ABSTRACT

PRODUCTION OF NANOCRYSTALLINE RDX BY RESS: PROCESS DEVELOPMENT AND MATERIAL CHARACTERIZATION

by
Victor Stepanov

The aim of the present work was to address the hazardous vulnerability of energetic materials to accidental initiation. An improved form of the explosive RDX with a significantly reduced sensitivity to stimuli including shock and impact was sought. The direction of this research was to investigate the effect of RDX crystal size reduction down to nano-scale dimensions on the sensitivity characteristics. Although size reduction of energetic crystals has been demonstrated often to result in a sensitivity reduction, the effect at the nano-scale particle size has not been investigated.

To generate nanocrystalline RDX a recrystallization process was developed based on rapid expansion of supercritical solutions (RESS). Compressed carbon dioxide was utilized as the solvent for RDX. Effect of key process parameters including the pre-expansion temperature and pressure, post-expansion pressure, and nozzle dimensions was investigated experimentally and *via* mathematical modeling.

The RESS process yielded pure RDX with a mean crystal size ranging from around 100 to 1000 nm with a relatively narrow size distribution and near spherical particle shape. Continuous processing with efficient particle collection and solvent recycling was accomplished enabling bulk production.

The sensitivity of RDX recrystallized by RESS was tested to stimuli including electrostatic discharge, impact, and shock was tested. Both pure samples as well as wax-

based formulations were tested. Two types of recrystallized RDX were tested, Type A and Type B, with a corresponding specific surface area of around 20 and 6 m^2/g. Both samples exhibited a significantly lower sensitivity to shock and impact compared to the reference 4.8 micron RDX. The coarser Type B nano RDX was found to be the least sensitive with all the tests. This indicates the existence of a minimum in sensitivity with crystal size.

PRODUCTION OF NANOCRYSTALLINE RDX BY RESS: PROCESS DEVELOPMENT AND MATERIAL CHARACTERIZATION

by
Victor Stepanov

A Dissertation
Submitted to the Faculty of
New Jersey Institute of Technology
in Partial Fulfillment of the Requirements for the Degree of
Doctor of Philosophy in Chemical Engineering

Otto H. York Department of Chemical Engineering

May 2008

APPROVAL PAGE

PRODUCTION OF NANOCRYSTALLINE RDX BY RESS: PROCESS DEVELOPMENT AND MATERIAL CHARACTERIZATION

Victor Stepanov

_____   04/08/08
Dr. Lev N. Krasnoperov, Dissertation Advisor   Date
Professor of Chemistry, NJIT

_____   4/8/08
Dr. Basil C. Baltzis, Committee Member   Date
Professor of Chemical Engineering, NJIT

_____   4/8/08
Dr. Rajesh N. Dave, Committee Member   Date
Distinguished Professor of Chemical Engineering, NJIT

_____   4/15/08
Dr. Dana E. Knox, Committee Member   Date
Professor of Chemical Engineering, NJIT

_____   4/8/2008
Dr. Frank J. Owens, Committee Member   Date
Senior Scientist, U.S. Army, ARDEC, Picatinny, NJ

BIOGRAPHICAL SKETCH

Author: Victor Stepanov

Degree: Doctor of Philosophy

Date: May 2008

Undergraduate and Graduate Education:

- Doctor of Philosophy in Chemical Engineering
  New Jersey Institute of Technology, Newark, NJ, 2008

- Master of Science in Chemical Engineering
  New Jersey Institute of Technology, Newark, NJ, 2003

- Bachelor of Science in Chemical Engineering
  New Jersey Institute of Technology, Newark, NJ, 2000

Major: Chemical Engineering

Publications:

V. Stepanov, I. B. Elkina, T. Matsunaga, A. V. Chernyshev, E. N. Chesnokov, X. Zhang, N. L. Lavrik, and L. N. Krasnoperov, "Production of Nanocrystalline RDX by Rapid Expansion of Supercritical Solutions," in *Advancement in Energetic Materials and Chemical Propulsion*, 74-86, Begell House, 2007.

V. Stepanov, L. N. Krasnoperov, I. B. Elkina, and X. Zhang, "Production of Nanocrystalline RDX by Rapid Expansion of Supercritical Solutions," *Propellants, Explosives, Pyrotechnics*, vol. 30, 178-183, 2005.

E. M. Glebov, L. G. Krishtopa, V. Stepanov, and L. N. Krasnoperov, "Kinetics of a Diels-Alder Reaction of Maleic Anhydride and Isoprene in Supercritical CO_2," *J. Phys. Chem. A*, vol. 105, 9427-9435, 2001.

L. N. Krasnoperov, and V. Stepanov, "Introduction of Laser Photolysis-Transient Spectroscopy in an Undergraduate Physical Chemistry Laboratory: Kinetics of Ozone Formation," *J. Chem. Ed.* vol. 76, 1182-1183, 1999.

V. Stepanov, V. Anglade, A. Bezmelnitsyn, and L. N. Krasnoperov, "Production and Characterization of Nanocrystalline Explosive RDX," *Proceedings of the AICHE Annual Meeting*, San Francisco, California, November 12-17, 2006.

V. Stepanov, P. Samuels, I. B. Elkina, X. Zhang, N.L. Lavrik, and L. N. Krasnoperov, "Recrystallization of RDX by Rapid Expansion of Supercritical Solutions (RESS),"*Proceedings of the 36th International ICT Conference*, Karlsruhe, Germany, 2005.

To my parents, Anatoli and Greta

and my sister, Renata

ACKNOWLEDGEMENT

TABLE OF CONTENTS

TABLE OF CONTENTS
(Continued)

TABLE OF CONTENTS
(Continued)

LIST OF TABLES

LIST OF FIGURES

LIST OF FIGURES
(Continued)

LIST OF FIGURES
(Continued)

CHAPTER 1

INTRODUCTION

Accidental detonation of munitions can result in loss of life as well as tremendous costs and compromised capabilities. It may occur on the battlefield as well as non-hostile environments. External stimuli that can lead to detonation include fires, lighting, stray bullets and fragments, and adjacent explosions. Moreover, the susceptibility of munitions to accidental detonation generally increases with power. It is therefore a tremendous challenge to enhance the performance parameters of an explosive without also sensitizing the explosive to inadvertent detonation.
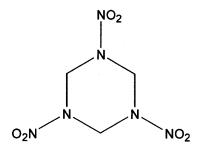
Today, an unprecedented amount of research is aimed at addressing the safety of munitions. Research tactics include modification of the chemical and physical structure of the explosive materials, improving the properties of the non-energetic ingredients of explosive formulations, and improving the design and composition of the shells and storage containers.

The focus of the present research is sensitivity reduction of the explosive RDX by crystal size reduction down to nano-scale dimensions. It is well known that the crystal size of an energetic material affects its sensitivity. In this work the sensitivity characteristics of RDX crystals with nano-scale dimension are investigated.

1.1 RDX

First synthesized by Henning in 1898, cyclo-1,3,5-trimethylene-2,4,6,-trinitramine (RDX) is among the most prevalent high brisance explosives used by the U.S. military. Industrial scale production of RDX started during the Second World War. RDX is typically used as a main ingredient in explosive formulations such as A5 and C4, but is also used in its pure form in applications such as output charges in detonators.

RDX belongs to the family of high energy density nitramine explosives which includes cyclotetramethylenetetranitramine (HMX) and hexanitro-hexaazaisowurtzitane (CL-20). The chemical structure of RDX is depicted in Figure 1.1.

Figure 1.1 Chemical structure of RDX.

RDX is the least powerful of the three nitramines described. However, due to its low cost and relatively low sensitivity, it is the most prevalent explosive in the U.S. Military. Processing of RDX is substantially less troublesome than HMX or CL-20. One reason is that only a single stable polymorph of RDX exists, while both HMX and CL-20 have four stable polymorphs of which only one is desired. Attaining the desired polymorph during crystallization is often challenging and limits processing options. For example the desired ε polymorph of CL-20 is generally only attainable during

crystallization from solution by seeding with ε CL-20. Consequently, a very limited choice of processing techniques is applicable, especially when it comes to size reduction, where seeding is not an option. Such limitations do not exist with RDX.

Several properties of RDX are listed in Table 1.1. RDX is soluble in solvents including acetone, cyclohexanone, acetonitrile, and DMF. It is nearly insoluble in water, alcohols, and hydrocarbons.

Table 1.1 Select Properties of RDX[1]

Molecular Weight	222.1 g/mol	Melting Point	204 $^{\circ}$C
Density	1.82 g/cm^3	Heat of Detonation	6322 kJ/kg
Dipole Moment	6.5 D[2]	Detonation Velocity	8750 m/s at 1.76 g/cc

Commercially available RDX ranges in crystal size from several to hundreds of microns. Larger grained RDX is typically produced by recrystallization from solvents such as cyclohexanone. Finer grained RDX is produced either by crash precipitation or milling.

In the quest for a less sensitive form of RDX, modification of the crystal size and quality are the main options. The processing flexibility of RDX may be a key factor in reaching the optimal form with the desired characteristics.

1.2 Objectives

The primary objective of the work presented in this dissertation was to produce a desensitized form of the explosive RDX while maintaining or enhancing the performance characteristics. It is known that crystal size reduction often leads to improved sensitivity characteristics. This work aimed to explore whether further decrease in sensitivity and improvement in performance can be achieved by reduction of the crystal size down to nano-scale dimensions.

Sensitivity testing requires bulk quantities of nanocrystalline RDX. Since RDX was not available with the desired small grain size, development of a process capable of producing nanocrystalline RDX was necessary. In an earlier work it was demonstrated that nanocrystals of RDX can be produced by rapid expansion of supercritical solutions (RESS)[3]. Based on the preliminary results it appeared that RESS is a viable process to meet the desired physical characteristics of RDX. A key task in this effort was to investigate the recrystallization of RDX by RESS and develop a process capable of bulk production.

Ultimately it was of interest to investigate the dependence of sensitivity to stimuli such as shock and impact on the crystal size at the nano-scale dimensions. Sensitivity testing of the pure samples as well as formulations containing the novel form of RDX was required to comprehensively assess the effects of size reduction.

CHAPTER 2
INITIATION OF SOLID EXPLOSIVES

A typical explosive charge consists of a high explosive material such as RDX or HMX which is commonly formulated with a polymeric binder system. Most of the explosive formulations have a solids loading in the range from 70-97 wt. %. Waxes and polymers are used as the main binder ingredient. Smaller quantities of additional ingredients such as surfactants and plasticizers are also commonly used in order to aid processing and achieve the desired material characteristics.

Both the chemical and physical properties of a high explosive affect its sensitivity towards incident energy stimuli from sources such as shock and impact. The performance of an explosive compound is dependent on the chemical structure of the explosive. In general, as the power increases so does the sensitivity toward incident energy stimuli. For example, among the well known high energy density nitramine explosives RDX, HMX, and CL-20, the power increases in the order listed with a corresponding increase in sensitivity to external stimuli.

The sensitivity of an explosive is not only a function of its chemical structure. The physical structure, which includes properties such as the crystal size, size distribution, shape, internal and surface quality, internal voids and inclusions, as well as the microstructure of the intercrystalline space have all been suggested to influence the response of an explosive to incident stimuli[4-7]. The physical microstructure governs the mechanical response of an explosive charge to incident stimuli and will affect the distribution of incident energy within the explosive charge. A heterogeneous microstructure is inherent in solid explosives (compared to the substantially more

5

homogeneous liquid explosives). The degree of heterogeneity may be an important characteristic and should be considered in the assessment of the mechanical response to incident energy.

The polymeric binder helps mitigate the risk of initiation of the explosive charge by unintended stimuli. Shearing and compressive forces resulting from incident stimuli can lead to ignition and consequently explosion of the affected charge. The binder reduces such vulnerability by eliminating direct contact between adjacent explosive crystals as well as filling the intercrystalline void space, resulting in a reduced sensitivity as well as improved performance.

In order to attain the desired performance and sensitivity characteristics the design of the explosive charge should involve the assessment of all the factors mentioned above including the chemical and physical structure as well as the formulation ingredients and processing.

2.1 Initiation of Heterogeneous Explosives

The physical structure of a solid explosive charge can influence the distribution of incident energy from a stimulus such as shock or impact. Due to the heterogeneous distribution of the incident energy in a polycrystalline explosive formulation, localized heating will occur[4, 8]. Heterogeneities within an explosive charge susceptible to energy localization can be crystal related such as dislocations, intra-crystalline voids and inclusions, and surface defects as well as formulation related including intercrystalline voids, voids within the binder, and voids at the binder-crystal interface. Localized heating

at such heterogeneities can result in the formation of "hot spots" which can subsequently lead to ignition and finally detonation of the explosive charge[4].

Common crystal heterogeneities such as cracks, inclusions, and surface defects in the explosive RDX are shown in Figures 2.1 and 2.2. In Figure 2.1 the inclusions and cracks are revealed by optical microscope analysis of sample crystals immersed in a matching refractive index fluid. Such macroscopic defects form during crystallization from a solvent and can be attributed to poor control of the crystal growth rate as well as impurities in the solutions[9]. Solvent inclusions can reach tens of microns in size.
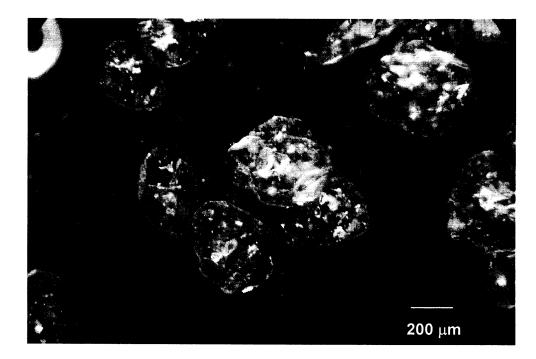
Figure 2.1 Optical microscope image of commercial grade RDX crystals.

Crystal defects such as dislocations are inherent in the crystal growth process. Defects alter the mechanical properties of the crystal and thus may influence the mechanical response to incident energy. Defects are believed to increase the sensitivity of an explosive.

In Figure 2.2 a topographical image generated by atomic force microscopy (AFM) of a commercial grade RDX crystal is shown. Micron scale surface defects can readily be seen. Such features may lead to poor surface wetting with the binder resulting in micron scale voids at the crystal-binder interface. Such voids may be susceptible to hot spot formation and thus may sensitize the explosive formulation.
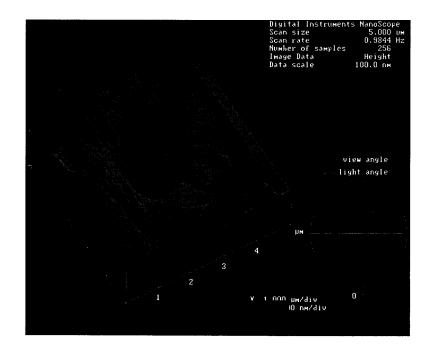
Figure 2.2 AFM generated surface image of a conventional RDX crystal.

2.2 Ignition of Explosives

Evidence of hot spot formation was demonstrated in the pioneering work by Bowden and Yoffe [4]. Investigation of liquid explosives, which are relatively homogeneous, revealed that the presence of small heterogeneities in the form of gas bubbles greatly sensitized the liquid explosive charge. It was concluded that compression of these bubbles by incident pressure waves lead to adiabatic heating of the trapped gas and consequently to the formation of hot spots which ignited the explosive.

Similarly, the incident energy from a shock wave or an impacting object is believed to localize within a solid, heterogeneous explosive and generate hot spots. Bowden and Yoffe estimated that critical hot spots with sufficient size (0.1 to 10 microns), temperature (>700 K), and duration (10^{-5} to 10^{-3} sec) are capable of igniting the surrounding explosive material which can lead to detonation[4]. On the other hand, hot spots which do not contain sufficient energy may be quenched by heat dissipation mechanisms including conduction, convection, radiation, and endothermic reactions[4, 10]. Both the activation energy of the initial endothermic reactions as well as the thermal conductivity of the explosive can thus influence the size and temperature of a hot spot necessary to reach the critical threshold. These properties depend on the chemical structure of the explosive. For example, the exceptionally low sensitivity of the powerful explosive TATB is ascribed to the high thermal conductivity of TATB as a result of hydrogen bonding[11]. Dissipation of hot spots is believed to be very effective in TATB resulting in a higher critical hot spot temperature necessary for ignition.

Calculations by Tarver et al. indicate that the critical hot spot temperature increases as the hot spot diameter is reduced from microns to 100 nm[11]. For the explosive HMX, the estimated critical temperature of a 1 micron diameter spherical hot spot was found to be around 1000 K, a reduction of the hot spot diameter down to 100 nm is expected to increase the critical temperature to around 1200 K. If this trend is extrapolated to a 10 nm hot spot, it can be shown that a critical temperature of around 1500 K will be expected. It was shown that the time to detonation decreases as the critical hot spot size is reduced. The calculations also indicate that the hot spot geometry does not greatly influence the critical temperature. Based on these calculations, it can be

concluded that a higher magnitude of incident energy will be required to initiate a heterogeneous explosive prone to smaller hot spot size. Such materials should exhibit a lower susceptibility to inadvertent initiation.

2.3 Mechanisms of Hot Spot Formation

2.3.1 Hot Spot Formation due to Adiabatic Compression

Hot spots may be generated by numerous mechanisms. One mechanism of hot spot formation involves the adiabatic compression of inter and intra-crystalline voids[4, 10, 12, 13]. The size and temperature of a hot spot formed in this manner will depend on the initial size of the void as well as the magnitude of the incident energy. For a given magnitude of incident energy, voids below a certain critical size may not heat to a temperature sufficient for ignition, rather, the energy can dissipate without an explosion.

The effect of the intercrystalline void size on the shock sensitivity of the explosive RDX is clearly seen in Figure 2.3[14]. The incident shock pressure required for a 50 % probability of initiation of the explosive as a function of packing density is shown. The material tested is unformulated RDX with a grain size above 100 microns. The sensitivity tests were performed with the small scale gap test. Details regarding this test method are described in Chapter 10. It can be seen in Figure 2.3 that as the density approaches the theoretical maximum density (1.82 g/cc for RDX), or as the void fraction of the packed explosives approaches zero, the sensitivity to shock greatly decreases.
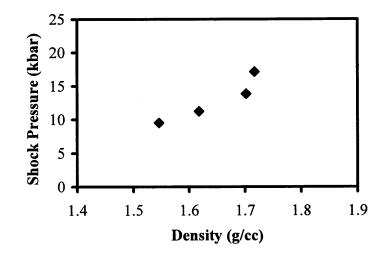
Figure 2.3 Effect of RDX powder density on the shock sensitivity[14].

This result reveals the effect of the intercrystalline void size on the hot spot formation. At lower packing densities a higher void fraction exists and thus the size distribution of the intercrystalline voids will likely tend to shift to larger sizes. Consequently, adiabatic compression of such voids due to shock loading leads to the formation of critical hot spots and detonation. The larger incident shock pressure required to initiate samples pressed to higher densities appears to be due to the smaller average void size.

A similar trend was observed by reducing the mean crystal size of the energetic material[5, 15]. The reduction of the particle size at a given packing density results in the reduction of the average intercrystalline void size, resulting in a reduced sensitivity to incident shock waves.

Due to the high sensitivity resulting from a large void content it is evident why explosives are seldom used in their pure form. Rather, formulations are prepared such that the large intercrystalline voids are filled with a polymeric binder. This mitigates the

formation of critical hot spots since pockets of gas, which are susceptible to adiabatic compression and heating, are eliminated. Although embedding the explosive crystals in a polymeric binder effectively eliminates large intergranular voids, small intergranular voids do remain. These can be found within the binder or at the binder/crystal interface due to poor coating as was discussed in Section 2.1. The content of voids can be minimized by proper formulation processing, including selection of binder ingredients which have strong affinity to the crystal surface, selection of explosive crystals with low surface defects, and coating or casting under vacuum to eliminate inclusions of trapped air[12].

The effect of voids in the binder phase on the sensitivity appears to be weak. Available experimental data indicate that their contribution to sensitivity is negligible even at a total void fraction of several %[16]. The formation of hot spots within the binder phase will likely not lead to ignition as the energy will be consumed by the endothermic decomposition of the binder or dissipated by conduction. Of more concern are the hot spots at the binder/crystal interface since direct heating of the explosive occurs.

The effect of the crystal surface quality on the sensitivity of plastic bonded explosives (PBX) was investigated[17]. Crystals with rough irregular surfaces were found to be more sensitive as compared to crystals with intentionally rounded and smoothed surfaces. The threshold shock pressure as well as the shock to detonation run-up distance were found to be higher for rounded crystals. It was suggested that voids at the crystal/binder interface which result from poor coating by the polymeric binder are responsible for the increased sensitivity.

Shock initiation tests on cast PBX formulations point mainly to the intracrystalline voids as the most consequential hot spot sites[13, 18]. The shock sensitivity correlates well with the void fraction in the explosive crystals. In a study with RDX and HMX it was demonstrated that both explosives were sensitized at higher void fraction[18]. In the same study the shock sensitivity poorly correlated with the void fraction within the binder ranging from 0 to 2.5 %.

Accurate assessment of the void fraction in crystals can be obtained with methods such as floatation density analysis[19]. However, the ability to assess the number of voids and the size distribution of voids is limited. Thus, it is unclear whether adiabatic compression heating, which is more effective with larger voids or perhaps other mechanisms relevant with smaller voids are dominant. The presence of voids may facilitate another mechanism of hot spot formation which results from shearing forces during plastic deformation of the explosive. Intracrystalline voids may compromise the mechanical integrity of the explosive crystals and facilitate mechanisms leading to plastic deformation and fracture. This topic will be covered in more detail in the following section.

2.3.2 Hot Spot Formation due to Plastic Deformation

Hot spot formation by localization of the incident energy is also believed to occur as a result of plastic deformation of explosive crystals. Several mechanisms are considered.

Localized stresses induced by incident energy was observed to lead to the formation of shear bands within the slip planes [20]. Evidence for shear band formation

has been observed in samples that underwent plastic deformation. Molten RDX appeared to extrude form within the shear bands.

Due to high shearing forces exerted on the explosive crystals by shock or impact substantial deformation of the crystal lattice and molecules occurs. This was observed experimentally by atomic force microscope analysis of crystals that were exposed to mechanical insults which did not lead to initiation. At incident energy levels near to but below levels required for initiation, plastic deformation of explosive crystals was seen in the form of distortion of the crystal lattice and the molecules[21, 22]. Individual molecules were observed to be shifted and rotated out of their equilibrium lattice positions. Displacement of molecules by as much as 20% was observed within the shear bands. Chemical reaction has also been observed to originate within these shear band regions[21]. In light of these observations, mechanochemical effects must be considered. The mechanical deformation of the crystal lattice may lead to a narrowing of the LUMO-HOMO energy gap thus reducing the activation energy required for chemical reaction[23]. Such shear strain in molecules has been known to induce chemical reactions athermally, or solely due to mechanical effects.

The presence of defects within crystals such as dislocations, cracks, and voids may facilitate plastic deformation. The lattice distortion described above was attributed to the presence of dislocations[21]. Meyer hardness analysis of conventional RDX revealed that substantial plastic deformation occurs prior to brittle fracture[24]. Such behavior is attributed to the presence of dislocations and has the implication that cracking occurs at lower stresses compared to cracking resulting from solely elastic deformation[25].

Explosives that were sufficiently confined to prevent or substantially limit plastic deformation exhibit higher initiation energy thresholds. Such confinement can be achieved in certain explosives by dead pressing or pressing at high pressures where the final bulk density is close the theoretical maximum density (TMD), which is the crystal density. Experiments with large single crystals have revealed a substantially higher initiation energy threshold. Single HMX crystal detonation experiments showed that with incident pressure equal to the equilibrium Chapman-Jouguet detonation pressure of HMX, the single crystals were found to be extremely insensitive and could not be initiated[26]. This was attributed to the lack of plastic flow following the incident shock. On the other hand, if pores and voids are abundant within an explosive charge, plastic deformation will be facilitated, lowering the initiation energy threshold. Large single crystals which were shocked the second time exhibited a substantially reduced initiation energy threshold.

Typical high explosives such as RDX are considered to be brittle [25] and thus crystal fracture is anticipated following a mechanical insult. Due to applied shear stress, a crystal can fracture along existing cracks or defects or due to dislocation motion induced by the applied stress.

Several models have been developed to describe the initiation behavior of heterogeneous explosives. Armstrong, et al. applied a dislocation pile-up model to the treatment of RDX initiation by the drop weight impact test[6]. The experimentally observed discontinuous deformation of RDX is believed to indicate that a dislocation pile-up collapse occurs. Dislocations within crystals are believed to accumulate under shear stress at grain boundaries which prevent their motion. When a sufficient

accumulation of dislocations occurs at a given boundary, the boundary can give way resulting in a breakthrough. Localized heating will occur at such site and may lead to the formation of critical hot spots. Such discontinuous flow behavior in metals is well known[27].

The required applied stress for a dislocation pile-up collapse can be related to the physical properties of the material as follows[25]:

$$\tau = \tau_0 + \left\lfloor c\sqrt{G\tau_c b}\right\rfloor l^{-1/2}$$

where τ_0 is the shear stress required for dislocation movement, G is the shear modulus, τ_c is the critical stress concentration which equals the product of the number of dislocations in the pile-up and the shear stress τ at which a collapse occurs, b is the Burgers vector, l is the slip length.

The inverse square root dependence of the shear stress on the slip length is based on the Hall-Petch effect which is known to predict the grain size dependence of plastic deformation of polycrystalline materials including metals. It was also found that such deformation behavior should result in a linear log-log relationship between the drop height necessary for initiation and $l^{-1/2}$. The slip length l can be assumed to be equal to the crystal size of the explosive. This relationship fits well to experimental impact test data of RDX with crystal size ranging from 22 to 1000 μm[6, 25]. The implication of such result is that as the crystal size is decreased the impact energy required for initiation should increase.
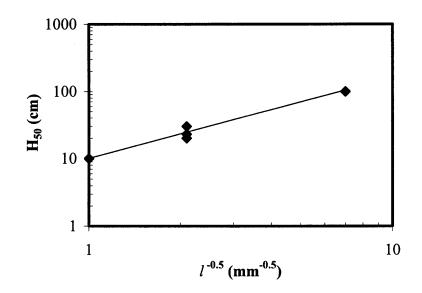
Figure 2.4 The dependence of impact sensitivity on the crystal size of RDX[6].

Coffey and Sharma considered initiation based on dislocation propagation due to tunneling in explosive crystals[21]. This model also predicted that as the crystal size of the explosive is reduced, a higher shear stress is necessary in order to achieve plastic flow. This is a consequence of the predicted increase in the lattice potential barrier with decreasing crystal size. In addition, the model indicates that explosives with a small crystal size should be more sensitive to short duration, high amplitude pressure pulses, while larger crystals should be more sensitive to long duration, low amplitude pulses. The calculations also revealed that the transition to detonation from the source of ignition of explosives with small crystal size is more rapid as compared to larger grained explosives. These predicted trends are in agreement with existing experimental data.

2.4 Effect of Crystal Size Reduction on Sensitivity

Based on the existing empirical as well as theoretical analyses of the effects of physical characteristics of a heterogeneous solid explosive on the sensitivity it appears that the reduction of the crystal size in an explosive charge should generally lead to a reduced vulnerability to unintended initiation.

A benefit of crystal size reduction appears to be the corresponding reduction in the size of the internal defects. Shock initiation of large grained explosives such as RDX shows a primary dependence on the defect density and a lesser dependence on particle size when sufficient binder is present to fill the interstitial voids. In a study by Caulder et al. the shock sensitivity of RDX with a low defect density, as determined by nuclear quadrupole resonance spectroscopy (NQR), was relatively constant with mean crystal size varying from 20 to 250 μm[7]. The shock sensitivity had a strong dependence on crystals size within the same size range for crystals with a higher defect density. The shock sensitivity increased with the crystal size. At the lowest size both types of RDX exhibited a similar sensitivity. This suggests that the size of defects influences the sensitivity.

Sensitivity data are available for crystals ranging in size from hundreds of microns down to around a micron. Based on the existing trends it appears that further reduction of the crystal size, specifically down to the submicron and nano-scale regimes, where the crystal dimensions are in the range 250-1000 nm and below 250 nm respectively, may lead to further desensitization. In addition, there is evidence that such drastic size reduction may also lead to an enhancement in the performance parameters of the explosive charges.

The mechanical response of a heterogeneous explosive to incident energy clearly plays a key role in the ignition and consequently detonation. Modification of the solid explosive by reducing the crystals size down to the nano-scale will have an impact on the mechanical response. Several key factors can be attributed to the anticipated change in the solid response due to reduction of the crystal size down to nano-scale dimensions. One factor is the elimination of large heterogeneities such as voids, cracks, and dislocations. The dimensions of hot spots are believed to be proportional to the size of such heterogeneities. As the crystal size is reduced, the size of defects as well as of intercrystalline voids will also be reduced resulting in a larger number of smaller defects and voids. The void fraction in principle may remain the same. Due to the larger number of smaller voids a more homogeneous distribution of incident energy can be anticipated. The energy distribution mechanisms which lead to localized energy at the heterogeneities may lead to the formation of hot spots of smaller dimensions as well as lower temperatures and thus will require larger incident energy to reach the critical initiation threshold.

Another consequence of crystal size reduction is increased mechanical strength of the explosive powder. In the preceding section it was shown that mechanical properties of nanocrystalline materials are expected to be altered. Enhancement of the mechanical properties including increased yield strength with reduced crystal size, which follows the well known Hall-Petch effect as well as enhanced hardness are anticipated.

The overall effect of size reduction down to the submicron and nano-scale dimensions is a more homogeneous distribution of the incident energy from stimuli such

as shock or impact as well as enhanced mechanical resistance to plastic deformation, which plays an important role in the formation of hot spots.
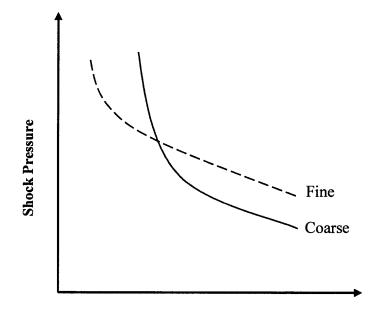
2.5 Effect of Crystal Size Reduction on Detonation Characteristics

Reduction of the crystal size is also expected to alter the performance characteristics of a solid explosive. Affected performance parameters may include the critical diameter, critical thickness, shock to detonation transition length, deflagration to detonation transition length, response to short duration high amplitude incident shocks, and shock spreading.

Fine grained explosives should exhibit a higher energy threshold necessary for initiation, however, once ignited the spread of reaction leading to detonation is expected to occur on a shorter time and length scales[11]. This was suggested to result from the higher hot spot temperature which leads to a faster rate of chemical decomposition[11]. Faster transition to fully developed detonation may also result from a higher number density of hot spots and the larger surface area of a fine grained explosive[28].

Based on shock initiation tests of cast plastic bonded explosive formulations, Moulard observed that as the crystal size of RDX is reduced from a mean size of around 400 μm to 6 μm, the pressure threshold required for initiation of the charge increased[28]. In addition, it was also observed that the run-up to detonation distance, which is the transition length from the location of incident shock to self sustained detonation, was altered. The trends observed by Moulard are illustrated in Figure 2.5. It was suggested that at lower incident pressures the transition to detonation is controlled by the formation of critical hot spots which leads to ignition. At higher shock pressures the

transition to detonation is governed by the rate of growth of explosion by coalescence of reacting fronts emanating from the hot spots to form a fully developed detonation front.

The crossover pressure seen in Figure 2.5 signifies the transition from ignition to growth dominated regimes. It can be seen that at lower incident shock pressures ignition is more effective with the coarsest crystals, which exhibit the lowest ignition threshold resulting in a shorter run-up to detonation distance. Above the crossover pressure the run-up to detonation distance becomes shorter for the finer grained samples due to faster growth to detonation rate resulting from a larger number density of hot spots as well as higher surface area of explosive.

Run-up to detonation distance

Figure 2.5 Qualitative representation of shock to detonation transition length for an explosive with fine and coarse grain size[28].

A similar trend was observed by Honodel et al. who demonstrated that the high surface area form of the explosive TATB was the most reactive to high amplitude short

duration incident shocks, however, it exhibited a reduced sensitivity at lower amplitude incident pressures[29]. Gifford et al. also observed that submicron samples of PETN exhibited a reduced sensitivity to long duration, low amplitude shocks[15].

The effect of the surface area of an explosive on the transition to detonation length at high amplitude short duration incident pressures is also evident with the explosive hexanitrostilbene (HNS)[5]. The high surface area form, HNS-IV, with a surface area ranging from 5-25 m^2/g, has been demonstrated to have a very short transition length to detonation. Due to its high surface area HNS-IV is uniquely capable of being detonated as the output charge in exploding foil initiators (EFI), where the output charge is detonated with a characteristically short duration, high amplitude shock.

These findings have important implications in that finer materials should be less vulnerable to unintended initiation by shock stimuli from sources such as adjacent detonations. Such sources typically generate shocks with low amplitude and long duration. On the other hand finer grained explosive should be initiated more effectively with controlled high amplitude shock sources such as detonators. A shorter run-up to detonation will also lead to improved performance since a larger fraction of the explosive will detonate. Another important consequence is that smaller size charges may be detonable with finer grained explosive.

Reduction of the crystal size has also been demonstrated to improve the detonation spreading performance or the corner turning ability of the detonation shock front in a given explosive. Lee et al. demonstrated using the Floret test that with fine grained explosive TATB improved detonation spreading was achieved[30]. The

detonation spreading ability is dependent on the critical diameter which is the minimum diameter of an explosive charge capable of sustaining detonation.

Gifford et al. investigated the initiation characteristics of submicron PETN and RDX[15]. It was demonstrated that samples of submicron PETN pressed into cylindrical 25 by 5 mm bores in PMMA confinement cylinders were readily initiated by short duration high amplitude shocks generated by laser driven flyer plates. Conventional PETN samples were not initiated in this test. This result appears to indicate that the critical diameter of conventional PETN is above 5 mm, therefore detonation cannot be established. Reduction of the crystal size to submicron scale apparently leads to a reduction in the critical diameter.

The reactivity and burn rate of nanocrystalline RDX is anticipated to improve due to a higher ratio of surface to bulk molecules. Quantum chemical calculations indicate that the dissociation of the $N-NO_2$ bond of the surface molecules requires significantly lower energy than that of the bulk RDX molecules [31].

2.6 Conclusions

The experimentally observed and mathematically predicted trends of the dependence of sensitivity and performance of solid heterogeneous explosives on the crystal characteristics were outlined. These trends indicate that further improvement in the properties of energetic materials may be achieved by reduction of the explosive crystal size down to the nano-scale. Both the sensitivity and the performance characteristics may be enhanced.

It would thus be of interest to investigate the crystal size dependence of sensitivity and performance parameters at the nano-scale. For such purpose it would be desirable to prepare samples of a novel high explosive with grain sizes ranging from 100 to 1000 nm, with relatively uniform size distribution. Furthermore, the novel material should consist of crystals of high purity, low defect density, and high surface quality. The new high explosive material should be incorporated into formulations prepared in such a manner that all the crystals are well wetted by the binder and the interstitial space between the crystals is entirely filled resulting in a fully dense composite.

CHAPTER 3

RECRYSTALLIZATION WITH SUPERCRITICAL FLUIDS

A large number of methods have been developed for the purpose of production of very fine organic particles. These may be classified as top-down and bottom-up processes. Top down methods achieve crystal size reduction by mechanically breaking down the larger precursor material. These include techniques such as grinding, milling, and crushing. The bottom-up methods involve processes where a material is grown to its final size. These include crystallization processes from solutions.

For particle size reduction of energetic materials, which are sensitive to intense thermal and mechanical stimuli, process safety is as important as the capability of a given process to achieve the desired particle size. Supercritical fluid based technology offers the capability to achieve the desired particle size under mild processing conditions. A brief review of select techniques and properties of supercritical fluids follows.

3.1 Recrystallization Processes

A number of recrystallization technologies have been developed that utilize supercritical fluids (SCF) as processing media. SCF's have been employed both as solvents and anti-solvents. The most common methods include the gas anti-solvent recrystallization (GAS), precipitation with compressed anti-solvent (PCA), and rapid expansion of supercritical solutions (RESS). These have been widely explored in recrystallization of compounds such as active pharmaceutical ingredients and polymers in order to achieve the desired particle size and morphology as well as product purity without degradation of the

material. A number of reviews have been published to date[32-34]. A brief introduction to these recrystallization methods follows.

3.1.1 Gas Anti-Solvent Recrystallization

The Gas Anti-Solvent recrystallization (GAS) process utilizes a compressed gas such as carbon dioxide as the anti-solvent and a conventional liquid as solvent[35, 36]. The solubility of most solids in a dense gas is typically several orders of magnitude lower compared to the solubility in conventional liquid solvents. Precipitation of a dissolved solute is achieved by pressurization of the solution with the compressed gas anti-solvent. The anti-solvent is usually in the supercritical state, however, subcritical gases have also been shown to be useful. As the liquid phase solution is pressurized with the gas, the solution expands. The rate and degree of the expansion are governed by the miscibility of the solvent/antisolvent pair as well as the system temperature and pressure. As the solution expands the solubility drops and the solute precipitates. The crystals are collected following depressurization of the vessel.

Recrystallization of the explosive RDX using the GAS technique was studied by Gallagher et al[36]. Acetone and cyclohexanone were used as solvents. Carbon dioxide was the anti-solvent. It was demonstrated that high quality crystals of RDX with few inclusions and a narrow size distribution can be achieved. The particle size was tunable from around 5 microns to hundreds of microns by controlling the rate of pressurization.

Teipel et al. studied the recrystallization of the explosive HMX using the GAS process[37]. The smallest particle size was found to be 65 microns for the acetone /

carbon dioxide system. Larger crystal sizes were obtained when using γ-butyrolactone as the solvent.

The GAS process appears to be suitable if particle size in the micrometer range is required, but does not appear to be viable for production of nanoparticles.

3.1.2 Precipitation with a Compressed Anti-Solvent

Recrystallization by precipitation with a Compressed Anti-Solvent (PCA) is similar to the GAS process. In contrast with the GAS process, the liquid phase is injected into a pressurized vessel containing the compressed gas anti-solvent[32]. Typically, the solution is injected through a nozzle, resulting in micro-droplet formation. Selection of a solvent / anti-solvent pair follows similar requirements as for the GAS process. Miscibility, temperature, pressure, and solute concentration are process parameters that can be used to control the particle size and morphology.

The solution droplets rapidly expand due to miscibility with the dense gas and precipitation takes place. It is believed that the expansion is faster than the bulk liquid expansion in the GAS process due to the higher surface area of the liquid phase. Resulting particle size tends to be smaller in comparison to the GAS process. Submicron particle of organic compounds have been produced using this process.

3.1.3 Rapid Expansion of Supercritical Solutions

Rapid expansion of supercritical solutions (RESS) has been successfully utilized to recrystallize a wide range of organic and inorganic solids down to submicron and nano-scale dimensions[38]. In contrast to the GAS and PCA processes, RESS solely utilizes a supercritical fluid which is used as the solvent. Precipitation of a solid dissolved in a supercritical fluid is induced by rapid depressurization, taking advantage of the strong solubility dependence on pressure. Depressurization can be achieved on a very short time scale (<50 μs), which can lead to rapid precipitation and formation of fine, uniform, and pure particles.

Carbon dioxide is the most commonly employed solvent, however many other solvents have been investigated. Since no organic solvents are required, the powders produced by RESS are dry and pure. Uniform particle size is often obtained by RESS. The particle size uniformity is a consequence of the highly uniform conditions within the expanding solution[39]. High crystal quality may be obtained by RESS due to the mild processing environment without exposure to intense mechanical or thermal stresses.

The RESS process was chosen for the present work. It offers the highest potential to reach the desired particle size and morphology as well as product quality and purity. A detailed description of the RESS process follows in Chapter 4.

3.2 Properties of Supercritical Fluids

Owing to the unique properties of supercritical fluids as processing media, technological capabilities unattainable with conventional methods are possible. Initial experiments with supercritical fluids date as far back as early 19th century. In 1822, Baron Cagniard de la

Tour first observed the appearance of the supercritical phase. In 1879, Hannay and Hogarth were first to notice that gases in their supercritical regime are able to dissolve solid materials[38]. Today, numerous processes take advantage of this phenomenon including extraction, crystallization, synthesis, and chromatography. Supercritical fluids are a unique media for processing, with properties intermediate between gases and liquids. These include liquid-like density and solubility and gas-like diffusivity and viscosity.

A substance is considered to be in the supercritical state when its temperature and pressure are above the respective critical values. The phase diagram for carbon dioxide, the fluid of interest in this work, is shown in Figure 3.1. The critical temperature of carbon dioxide is 304.2 K and the critical pressure is 73.8 bar[40]. The critical point lies at the tip of the liquid / vapor phase boundary. As the critical point is approached, the vapor and liquid phases become less and less distinguishable. The two phases merge gradually as the liquid phase expands while the equilibrium vapor phase is compressed, becoming a single phase at the critical point.

Compounds above their critical temperature are in the gas phase, where condensation into a liquid phase under pressure is no longer possible. Solidification will occur as the pressure is increased.

The near critical region is of high interest since dramatic changes in the fluid properties occur. At the critical point a fluid is infinitely compressible. This results in drastic variation of physical properties such as the density, isochoric heat capacity, and sound velocity in the near critical fluid[41]. The solvent power in this near critical region also changes drastically.
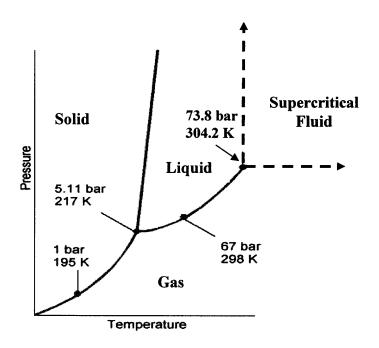
Figure 3.1 Phase diagram of carbon dioxide.

The primary parameters influencing the solubility in a supercritical solvent are the fluid temperature and pressure. As a result, the manipulation of solubility is possible by tuning both temperature and pressure. With conventional liquid solvents solubility can be manipulated only with the temperature.

Compounds that have mild critical parameters, (i.e. P_c < 100 bar, T_c < 100 °C) are most desired in supercritical fluid processing. Due to its mild critical properties, low cost, low toxicity, and chemical inertness, carbon dioxide has been by far the most widely investigated compound. A variety of other compounds have been investigated as supercritical processing media. Table 3.1 lists the critical properties of compounds which may have applicability in supercritical fluid processing.

The solvent strength is a major criterion in selecting the appropriate supercritical solvent. However, cost, safety, and environmental concerns also play a big role. For

example, nitrous oxide has been investigated due to its strong solvent power. It has an advantage over carbon dioxide due to its polarity and may be a better solvent for polar solids than the non-polar carbon dioxide. However, explosions of highly compressed nitrous oxide have been reported thus limiting its use. Halogenated compounds such as chloroform and fluoroform are also desirable fluids due to their mild critical parameters as well as polarity, however, high costs as well as environmental concerns may limit their use.

Table 3.1 Properties of Select Supercritical Solvents[40]

Compound	Mol Weight (g / mol)	Critical Temp (K)	Critical Pressure (bar)	Critical Density (g / cm^3)	Critical Compressibility	Accentric Factor
CO_2	44.01	304.19	73.82	0.468	0.274	0.228
N_2O	44.01	309.57	72.45	0.452	0.274	0.142
H_2O	18.02	647.13	220.55	0.322	0.229	0.345
SF_6	146.06	318.69	37.60	0.736	0.282	0.215
CHF_3	70.01	298.89	48.36	0.525	0.259	0.267
NH_3	17.03	405.65	112.78	0.235	0.242	0.252

3.3 Solubility of Solids in Supercritical Fluids

The solubility of many organic and inorganic compounds is known in supercritical solvents[42, 43]. Although appreciable solubility in a supercritical fluid can be achieved, the solubility levels are usually orders of magnitude lower than in conventional liquid solvents. Solubility becomes appreciable in the near critical region and increases above the critical point. At a given temperature a maximum in solubility exists beyond which

increasing the pressure will lead to a reduction in solubility. The dependence of RDX solubility on the temperature and pressure in carbon dioxide is illustrated in Figure 3.2.

At supercritical conditions the fluid properties become highly non-ideal. Interaction with the solute enables dissolution of solids to levels many orders of magnitude in excess of what would be expected with an ideal fluid, which would correspond to the solid's vapor pressure. Consequently substantial dissolution of solids with low volatility is possible.

The effect of density of a supercritical solvent on the solubility of solids is important. As can be seen in Figure 3.2, at pressures below *ca.* 150 bar a crossover of the solubility dependence on temperature exists. Isobaric heating of the supercritical solution at pressures below the crossover pressure results in a solubility decrease. This is often referred to as "retrograde" behavior. Such behavior is characteristic of supercritical solvents[44]. The crossover pressure signifies the dual effect of temperature and fluid density on the solvent strength. Below the crossover pressure the effect of the fluid density exceeds that of the temperature. Isobaric heating results in a density drop causing a reduction in the solvent strength. Interestingly, a single crossover pressure is often observed for a wide range of temperatures. A unique property of the upper crossover pressure is the temperature independence of solubility. The mathematical criterion for the crossover pressure in terms of the mole fraction of solute y_2 can be described as follows[44]:

$$\left(\frac{\partial \ln(y_2)}{\partial T} \right)_P = 0 \qquad (3.1)$$
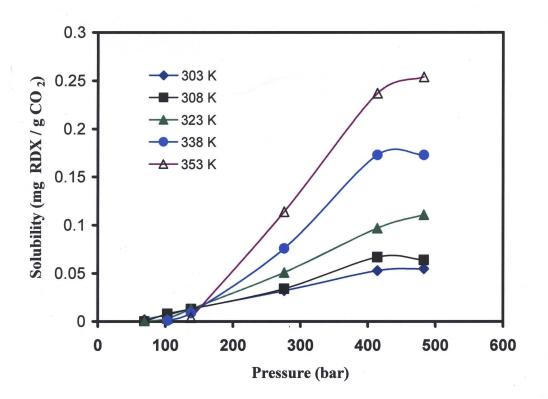
Figure 3.2 Pressure and temperature dependence of RDX solubility in supercritical carbon dioxide[2].

Near the critical point, the solvent molecules tend to cluster around the solute forming a fluid with localized high density regions[45, 46]. Clustering has been experimentally observed. Consequently, the partial molar volume of the solute in a dilute solution near the critical point can have a large negative value. For instance, at 35 $^{\circ}$C and 78 bar the partial molar volume of naphthalene in carbon dioxide is -10.8 L/mol. The partial molar volume of pure carbon dioxide is 0.0944 L/mol[47]. Such dramatic clustering near the critical point is likely related to the infinite isothermal compressibility of a fluid at its critical point. Interaction forces between the solvent and solute are sufficient for the solvent to aggregate into dense clusters surrounding the solute. Such

clustering is most pronounced near the critical point and diminishes at higher pressures and temperatures.

The critical parameters of supercritical solutions depend on the solute concentration. At low concentrations the influence of solute is likely negligible, at high solute concentrations there may be significant effects. This is especially important when the processing conditions are near the critical point of the solvent, such that small shifts in the critical parameters may lead to possibly detrimental solvent phase change.

3.3.1 Calculation of Solubility

Calculation of expected solubility of solutes in supercritical solvents may provide useful results without laborious experimental measurements. Modeling of the solubility of solids in compressed gases is most effective for low density solutions with non-polar solute species. For such cases fairly accurate solubility values may be predicted from the virial equation of state with the application of the second and third virial coefficient[47]. At higher densities, which are likely more suitable for numerous supercritical fluid processes, the applicability of the virial equation of state becomes less favorable as the fourth and higher virial coefficients become relevant. Estimation of these higher coefficients is increasingly complicated and often reasonable values are not attainable.

Empirical equations of state such as the cubic Peng-Robinson equation of state may be useful in correlating the solute's vapor phase fugacity coefficient to the solution parameters including the pressure and temperature.

The solubility tends to be higher for more volatile compounds. Knowledge of the solute's vapor pressure usually provides a good indication of the degree of achievable

solubility. Most conventional solubility models are formulated around the solute's vapor pressure[48, 49]. Temperature, accordingly, is a major factor affecting solubility since the vapor pressure of the solute increases exponentially with temperature. Similar compounds such as isomers may have orders of magnitude difference in solubility in a supercritical fluid. This difference was found to be closely related to the solutes vapor pressure.

The significant solubility of solids in dense gases can be interpreted to result from a large enhancement of the solute's vapor pressure due to interaction with the solvent. For an ideal gas solvent, the expected solubility of a solid would correspond to its vapor pressure as follows:

$$y_2 = \frac{p_2^{sat}}{p} \qquad (3.2)$$

where y_2 is the mole fraction of the solute in the vapor phase, p_2^{sat} is the equilibrium vapor pressure of the solid and p is the pressure of the system. Such approximation for supercritical solutions is highly inaccurate. In the ideal gas scenario, no solvation effect by the solvent gas is present, thus, the only amount of solute in the solution is that equivalent to its solid / vapor equilibrium at the given temperature and pressure. If this were the case, only negligible concentrations of solute could be achieved. However, the solvation effect of real, non-ideal dense gases can be tremendous. At high densities, solvent molecules interact with the solute. Such interaction results in significant solvation. This effect can be quantified by introducing the enhancement factor:

$$E = \frac{y_2}{p_2^{sat}/p} \qquad (3.3)$$

This expression represents the ratio of the actual concentration of solute in the gas phase versus the concentration in an ideal gas. The value of E for supercritical solvents is typically very high, reaching values as high as 10^{10}[50, 51]. The enhancement is typically correlated according to:

$$E = \frac{\varphi^{o,v}}{\varphi^v} exp\left[v^s \left(\frac{p - p^{sat}}{RT} \right) \right]$$

(3.4)

where $\varphi^{o,v}$ is the solute fugacity coefficient in the reference state, φ^v is the solute fugacity coefficient in the vapor phase, v^s is the molar volume of the solute, p^{sat} is the vapor pressure of solute, and p is the pressure of the system.

The exponential term is known as the Poynting correction factor. This term can be omitted for pressures below *ca.* 100 bar. The value of $\varphi^{o,v}$ is typically very close to 1, especially for solids. The fugacity coefficient of the solute in the gas phase is of most interest. Values below 10^{-6} are not uncommon. This is a clear indication of the high degree of non-ideality in a supercritical solution, which is responsible for the high attainable solubility.

The solubility of solutes in a supercritical solvent may be estimated using a cubic equation of state, such as the Peng-Robinson equation shown below with an appropriately determined mixture parameters a and b using mixing rules[52].

$$P = \frac{RT}{V-b} - \frac{a(T)}{V^2 + 2bV - b^2}$$

(3.5)

$$a(T) = 0.45724 \frac{(RT_c)^2}{P_c} \left(1 + k \left(1 - \left(\frac{T}{T_c} \right)^{1/2} \right) \right)^2$$

$$k = 0.37464 + 1.54226\omega - 0.26992\omega^2$$

$$\omega = \text{acentric factor}$$

$$b = 0.07780 \frac{RT_c}{P_c}$$

The values of the parameters a and b for a mixture are related to the pure component values *via* mixing rules. Commonly the van der Waals one-fluid mixing rules are used in conjunction with the Berthelot combining rule for a_{ij} as shown below for a two component system[52]:

$$a = y_1^2 a_1 + y_2^2 a_2 + y_1 y_2 a_{12} \tag{3.6}$$

$$a_{12} = (a_{11} a_{22})^{0.5} (1 - k_{12})$$

$$b = y_1 b_1 + y_2 b_2 \tag{3.7}$$

$$k_{12} - \text{mixing parameter}$$

The parameter k_{12} is often set to one, however if solubility is known, it may be determined by regression.

3.3.2 Modification of Supercritical Solvents

The solubility of polar compounds in supercritical solvents is typically lower than that of non-polar compounds, especially when a non-polar solvent such as carbon dioxide is used. A common technique for enhancing the solubility of polar materials in supercritical carbon dioxide is by modification of the supercritical fluid with a cosolvent. Commonly the cosolvents are organic solvents such as acetone, acetonitrile, and methanol, which

tend to be good solvents for the given solute. Modification with just a few mole % of a cosolvent can result in a solubility enhancement of over two orders of magnitude[53, 54].

A modified solution will have modified critical parameters, thus if working in the near critical region, the shift of the critical parameters should be known in order to avoid the often undesirable two phase regime [55]. The shift of the critical parameters due to cosolvent modification can usually be determined with sufficient accuracy from the arithmetic mean values of the given solvent and modifier:

$$T_c = y_s T_{c(s)} + y_m T_{c(m)}$$
$$P_c = y_s P_{c(s)} + y_m P_{c(m)}$$

(3.8)

More accurate results may be obtained from an equation of state such as the Peng Robinson equation. Table 3.2 lists the calculated shifts in critical parameters for systems of carbon dioxide with several commonly used cosolvents[56].

Table 3.2 Critical Parameters of Modified Carbon Dioxide[56]

Mole % Modifier	Acetone		Methanol		Ethanol		n-Propanol		i-Propanol	
	T_c (°C)	P_c (bar)	T_c (°C)	P_c (bar)	T_c (°C)	P_c (bar)	T_c (°C)	P_c (bar)	T_c (°C)	P_c (bar)
0	31.3	73.82	31.3	73.82	31.3	73.82	31.3	73.82	31.3	73.82
1	34.7	77.9	32.7	76.5	32.7	76.6	35.5	76.8	34.5	76.2
2	36.8	79.7	34.7	78.2	35.7	78.3	39.1	80.5	37.4	79.3
4	43.7	85.7	37.7	81.7	40.5	84.3	47.2	90	43.5	85.1

Cosolvents typically chosen exhibit a high solvent strength as liquids, however, non-solvent liquids are also occasionally chosen. Compounds that are non-solvents as liquids may be effective cosolvents in a supercritical solution. Solvent-solvent interaction in the liquid phase is much stronger than in the gas phase. Water, for instance, exhibits strong hydrogen bonding in the liquid phase, preventing it from dissolving numerous compounds, however, such strong bonding is absent in the gas phase. Non-solvent cosolvents are often desired[57]. Upon expansion of the solution both the solute and the cosolvent will typically condense. A cosolvent which is a non-solvent it its liquid phase may be desirable as it will not redisolve the product.

Understanding the miscibility of the cosolvent with the primary solvent is also of high importance since often excess cosolvent will result in the formation of a liquid phase[58]. For example, in the case of acetonitrile in carbon dioxide, the amount of acetonitrile should remain below 2 mole % at pressures below 170 bar. Further addition of acetonitrile results in phase splitting[59].

The solubility of nitramine energetics such as RDX, HMX, and CL-20 is low in supercritical carbon dioxide. This is expected due to the polar nature of these solutes as well as their low vapor pressures. It was experimentally determined that the solubility of RDX greatly increased in the presence of a solvent modifier[60]. The experiments compared the rate of RDX extraction with supercritical carbon dioxide, and supercritical carbon dioxide modified by DMSO and acetonitrile at 50 °C and 414 bar. The results showed that carbon dioxide modified with 6.1 mole % acetonitrile exhibited a 16 fold increase in solubility over neat carbon dioxide. Carbon dioxide modified with 5.6 mole % DMSO, exhibited over 120 times higher solubility than unmodified carbon dioxide.

3.4 Experimental Solubility Measurement

A variety of techniques have been described in the literature focusing on the solubility measurement of compounds in supercritical solvents. Most of these techniques fall into three categories: gravimetric analysis, spectroscopic analysis, and cloud point observation analysis. For sufficiently soluble compounds, gravimetric and cloud point techniques may be adequate. However, for poorly soluble compounds a more sensitive technique such as spectroscopy may be required.

3.4.1 Gravimetric Solubility Analysis

The simplest approach for measuring the solubility of compounds in supercritical fluids is by gravimetric methods[61]. With a gravimetric approach a saturated supercritical solution is prepared at a desired temperature and pressure. The solution is expanded into a controlled volume. The precipitate is collected and the amount is quantified. One way of analyzing the collected solute is by weighing. This is typically done with the continuous technique where significantly more precipitate is collected. In a batch arrangement, the precipitate may be collected by dissolving in a liquid solvent. The solution may be analyzed with a spectrophotometer for concentration of solute. From the quantity of the precipitate and the corresponding volume of expanded solution the solubility is determined.

3.4.2 Solubility Analysis by Cloud Point Observation

Cloud point observation is a convenient technique for the solubility determination[62]. This technique requires a high pressure, variable volume view cell. A window is built in

to allow visual observation of internal contents. A light source and a camera are mounted on the window and the cell contents are viewed on a monitor.

A known amount of solute is placed inside the view cell. An amount that is completely soluble in the given volume of solvent is necessary. Dissolution of the solute is visually confirmed by monitoring the solute disappearance inside the cell. Following complete dissolution, the cell is slowly expanded at constant temperature. Upon expansion, the pressure of the solution drops and the solvent strength decreases. Below the saturation pressure precipitation of the solute occurs resulting in a transition from an transparent to an opaque state of the fluid. This is termed "cloud formation". The solubility is determined based on the conditions at the onset of cloud formation. This process does not work for poorly soluble compounds since the cloud point below a certain solute concentration is not visually detectable.

3.4.3 Spectroscopic Solubility Analysis

Spectroscopic analysis enables more sensitive and accurate determination of solubility in supercritical solvents compared to the gravimetric and cloud point methods. This method is especially useful with poorly soluble substances. A variety of techniques incorporating spectroscopy exist including flow through[2, 63] and stagnant modes. Solute concentration is derived from the light absorption by the solute. Normally, the absorption in the ultraviolet (UV) spectrum is of interest.

Such analysis requires a high pressure view cell with two windows located opposite one another. Absorption is measured by comparing the intensity of the incident

light with that of the emerging light from the view cell. The absorbance, A, is determined according to the Beer-Lambert expression:

$$A = -\log \frac{I}{I_o} = \varepsilon [c] l \qquad (3.9)$$

The log of the ratio of the emerging light to the incident light is proportional to the concentration $[c]$ and the length of the optical path (distance between windows) l by the constant ε, which is the molar absorption coefficient[64].

Using a flow cell the relative solubility may be determined. In order to determine the absolute solubility a stagnant cell is required with a known quantity of the loaded solute.

3.5 SUMMARY

Supercritical fluid methods appear suitable for processing of energetic materials such as RDX. A number of solvents may be considered of which carbon dioxide appears to be the most desired. However, polar solvents or carbon dioxide modified with cosolvents may need to be considered if the solubility of the target material is inadequate.

Of the known supercritical fluid recrystallization methods the RESS process appears to be the most suitable to meet the required particles characteristics of the present study. RESS is the most appropriate due to the achievable low particle size, complete separation of solvent from the product, and safe processing conditions.

The ability of supercritical solvents to dissolve solids such as RDX is a consequence of the high fluid non-ideality. Both the solute's vapor pressure and the interaction strength with the solvent influence the solubility. Several generalizations can

be made regarding the phase behavior of supercritical solutions. The solubility of solids strongly correlates with the vapor pressure of the solid. In general it can be assumed that the solid with the higher vapor pressure is likely to exhibit a higher solubility in a given supercritical solvent. Due to the temperature dependence of the vapor pressure of a solid, isochoric temperature increase is expected to result in an increased solubility. At constant temperature the solubility tends to increase with solvent density.

CHAPTER 4

PARTICLE FORMATION BY RESS

4.1 Introduction

Very small particle size may be achieved by recrystallization of solids by rapid expansion of supercritical solutions (RESS). Recrystallization of a wide range of materials including organic and inorganic substances was investigated[32]. The reported mean particle size of solids recrystallized by RESS ranges from less than 100 nm to microns[38, 39, 65].

The small achievable particle size is attributed to the rapid change in the solvent strength resulting from expansion. Particle size uniformity is also expected due to the uniform conditions within the expanding fluid. In contrast to conventional liquid solvents, with temperature being the only relevant parameter, the solubility in supercritical fluids is dependent on both temperature and pressure. Precipitation can thus be induced by lowering of the pressure. Drastic solubility change can be achieved as a result of expansion, which may occur on the microsecond time-scale. Consequently, supersaturation levels above 10^6 are believed to be attainable[66, 67].

High supersaturation and rapid precipitation are essential for the formation nanoparticles by crystallization. At the supersaturation levels achievable during RESS, the critical nucleus size has been estimated to be as small as a single molecule[68, 69]. At such supersaturation levels a very high nucleation rate is also expected. Consequently, precipitation during RESS is believed to occur via homogeneous nucleation and condensation, which results in a large number of small particles. Following precipitation, particle growth may continue by coagulation. The final particle size is expected to depend

on the extent of coagulation. An outline of key principles of particle formation by RESS is shown in Figure 4.1.
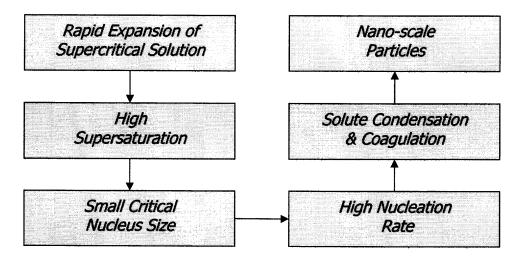
Figure 4.1 Principles of particle formation by RESS.

Complete separation of the solvent from the product is expected upon expansion resulting in a dry and pure material. In contrast, solvent inclusion and contamination is often a problem with crystallization from liquid solvents.

Carbon dioxide is the most commonly employed solvent due to its mild critical parameters, low cost, low toxicity, and chemical inertness. However, in principle a wide choice of compounds may be utilized as long as the critical state is reasonably accessible and no toxicity or reactivity prohibit their use. A number of potential solvents are listed in Table 3.1.

Rapid pressure drop is achieved by expansion of a supercritical solution across a flow restriction such as a nozzle. Nozzles range from short orifices to long capillaries. Typical nozzle diameters range from around 50 to several hundred μm with aspect ratios (L/D) ranging from around 1 to several thousand. The choice of a nozzle will determine

the expansion rate and thus can influence the final product characteristics. A much slower expansion is attributed to long capillary nozzles, as high as 0.1 s, compared to 10^{-5} s for short orifice nozzles[70]. The expansion rate will influence the degree of achievable supersaturation and thus may influence the particle size of the precipitate.

Rapid expansion of a supercritical solvent such as carbon dioxide leads to substantial cooling. The overall temperature change is the result of non-ideal gas behavior. Isenthalpic expansion of real gases is accompanied by a change in the temperature. This thermodynamic phenomenon is known as the Joule-Thomson cooling or heating. Whether cooling or heating results will depend on the sign of the Joule-Thomson coefficient, which is defined in Equation 4.1:

$$\mu \equiv \left(\frac{\partial T}{\partial P} \right)_H \qquad (4.1)$$

At the conditions relevant to the RESS process, most gases have a positive value of the Joule-Thomson coefficient. This means that isenthalpic expansion will lead to cooling.

Additional cooling occurs along the expanding fluid due to isentropic conversion of enthalpy into kinetic energy. Such cooling is relevant to the precipitation processes occurring within the high velocity jet. Temperature losses due to isentropic expansion are recovered downstream of the flow restriction as the velocity is reduced. Depending on the pre-expansion temperature and pressure as well as the downstream conditions, the net effect of cooling may lead to solvent condensation. Carbon dioxide may condense forming dry ice upon expansion to atmospheric pressure. The onset of condensation may occur inside the nozzle or downstream of the nozzle in the supersonic free jet where the

lowest temperatures are achieved. In some cases condensation may be prevented by sufficiently elevating the pre-expansion temperature.

A number of process parameters can influence precipitation and growth of particles during RESS and thus affect the final particle size. The pre-expansion temperature and pressure, solute concentration, nozzle size and geometry, and discharge temperature and pressure in the expansion chamber all are known to influence the particle size and morphology.

Depending on the process conditions, precipitation of the solute during RESS can start as early as at the nozzle inlet region or as late as the free jet downstream of the nozzle. The particle size and morphology has been demonstrated to be sensitive to such process parameters. Lele and Shine observed that expansion at conditions such that the onset of precipitation is favored to occur earlier in the expansion, the polymer precipitate exhibited a fiber-like morphology. At conditions where the onset was favored further downstream particle formation was observed[71].

The solute concentration also appears to be an important process parameter. Existing trends indicate that the particle size will generally increase with solute concentration. This trend is not always true, especially at very low concentration levels. If very small particle size is required, low solute concentration may be necessary.

Turk investigated the precipitation of naphthalene, cholesterol and benzoic acid by RESS with carbon dioxide as solvent[72]. The solubility of naphthalene is relatively high and can reach values on the order of 10^{-2} mole fraction, liley due to its high vapor pressure. The results showed that in general cholesterol, which has the lower solubility, around 10^{-4} mole fraction, precipitated with a particle size around an order of magnitude

smaller than naphthalene. It was also found that increasing the pre-expansion pressure, which resulted in a higher solvent density and higher solubility, led to an increase in the particle size. Results with benzoic acid, which is around one order of magnitude less soluble in CO_2 than naphthalene (10^{-3} mole fraction), showed in general a lower mean particle size compared to naphthalene. The observed trend was that the particle size tends to be lower for less soluble materials.

Experimental results also indicate that for poorly soluble compounds the particle size is not very sensitive to process conditions such as the pre-expansion pressure and temperature. Helfgen et al. investigated recrystallization of griseofulvin, which is poorly soluble in CO_2 (10^{-5} mole fraction)[68]. Particle size below 300 nm was achieved for the entire range of experimental conditions. It was observed that the pre-expansion conditions had little effect on the particle size. This observation is analogous with that observed with crystallization of the similarly poorly soluble cholesterol by Turk[72].

The post-expansion conditions can also affect the particle size. Experiments on recrystallization of naphthalene from supercritical carbon dioxide showed that reduction of the post-expansion temperature lead to a substantial increase in the crystal size[39]. A moderate decrease in the crystal size was observed as a result of increasing the post-expansion pressure.

The nozzle dimensions are also known to influence the particle size. The particle size tends to increase with nozzle size and aspect ratio[52, 73]. Dramatic particle size reduction has been observed with expansion across microporous channels. Huang and Moriyoshi demonstrated that an order of magnitude particle size reduction of loperamide HCL can be achieved by using a 5 μm clearance nozzle compared to conventional 100

µm internal diameter nozzle[74]. Domingo et al. also observed a size reduction of several solutes when using a microporous frit as the expansion device compared to a capillary nozzle[75]. Such low clearance nozzles may not be practical due to low flow rates and a much higher tendency to clog.

Changes in particle morphology as a result of changing the nozzle aspect ratio have also been observed in the experimental work of Lele and Shine[71]. It was found that the morphology of the precipitated polycaprolactone was drastically affected by reducing the nozzle aspect ratio. At the shorter aspect ratio long fibers were produced while at the longer aspect ratio particles were produced. It was suggested that solute precipitation occurring further upstream will occur at a slower rate[71].

The particle size may also be influenced by the condensation of the solvent. In a study by Matson et al., it was observed that at pre-expansion conditions which led to solvent condensation during expansion larger particles were formed compared to conditions such that no solvent condensation occurs. The role of solvent condensation was interpreted as dissolution of the solute in the solvent drops which subsequently precipitated as large particles upon evaporation[76].

An important drawback of RESS processing is the low solubility of most solutes of interest in supercritical fluids. Consequently large amounts of solvent must be processed leading to high processing costs. To address this limitation enhancement of solubility using cosolvents has been studied. Modification of a supercritical solvent such as carbon dioxide with a small amount of an organic solvent such as acetone or ethanol can lead to as much as several orders of magnitude enhancement in solubility. A difficulty arises with liquid cosolvents as they tend to condense upon expansion and

redisolve the product. Compounds that are highly soluble in supercritical fluids yet are solids at room temperature and pressure, such as menthol have recently been investigated as cosolvents[77]. Their utilization has shown a substantial improvement in the solvent power without the undesired dissolution of product downstream of the expansion. However, separation of a solid cosolvent by methods such as sublimation may be problematic.

4.2 Solute Precipitation during RESS

Depending on the expansion conditions and the nozzle dimensions the onset of precipitation may occur during subsonic expansion up-stream of the nozzle exit or within the supersonic jet downstream of the nozzle. The precipitation conditions can greatly differ affecting the final particle size and morphology.

A number of mechanisms are involved in particle formation during RESS. Initial precipitation occurs by homogeneous nucleation accompanied by solute condensation. The growth of particles does not end once all solute has been precipitated. Additional growth occurs *via* coagulation. Very large particle size is often attributed to coagulation which may continue far downstream of the nozzle.

Theoretical modeling of solute precipitation during RESS has evolved in complexity over the past two decades, however, predictions still cannot fully account for the experimentally observed particle size. Complete description of the RESS process requires the modeling of the fluid dynamics and thermodynamics of expansion as well as modeling of the solute precipitation. Numerous models have been developed which describe the fluid properties along the expansion path [52, 66-68, 71-73, 78-80].

Calculations considered both subsonic expansion which occurs prior to the nozzle exit and supersonic free jet expansion occurring downstream of the nozzle. Precipitation models have been coupled to the flow models in order to calculate the particle size evolution along the expansion path.

Fairly accurate description of the flow properties in the subsonic expansion regime up stream of the nozzle exit have been achieved by one-dimensional compressible flow calculations[71, 73, 81]. Free-jet expansion down-stream of the nozzle is far more complex and difficult to accurately describe mathematically. Multi-dimensional modeling is required in this flow region[79, 82]. The complexity arises from the drastic changes in the pressure and temperature of the fluid, condensation of the solvent, and complex events occurring within the transonic region where the jet velocity drops to subsonic values which is accompanied by shock formation. Shocks normal to the flow as well oblique shocks are present at the transonic stage. Here spikes in the fluid temperature and pressure occur.

Although condensation of solvent in the expanding jet is likely for a wide range of useful expansion conditions, it has not been adequately addressed in the literature. The majority of modeling efforts have considered simplified flow conditions where no condensation of the fluid occurs. Such conditions can be achieved experimentally, however, may not be practical. For example, free-jet calculation by Shaub et al., used a high pre-expansion temperature, 550 K, in order to preclude conditions that may lead to solvent condensation[78]. Helfgen et al. allowed for condensation of carbon dioxide in their fluid dynamics treatment of the expansion[81]. Homogeneous nucleation of carbon dioxide was presumed to lead to droplet condensation. As will be demonstrated in

Chapter 9, homogeneous nucleation may not accurately describe the condensation of the solvent.

Another difficulty arises in the accurate description of the solute precipitation mechanisms and kinetics along the expansion path. Precipitation inside the nozzle occurs under conditions where fluid phase non-ideality is significant and can affect events such as nucleation. In the free jet, extremely high supersaturation values can be achieved, with high estimates above 10^8. At such conditions it was shown that the classical nucleation theory may no longer be applicable[67, 69].

Values of important parameters needed for calculations such as the interfacial tension between the precipitate and the fluid are generally unknown, and estimates can lead to substantial error in calculations[73]. Another obstacle is the equation of state used in the calculations. Although cubic equations of state such as the Peng-Robinson or Redlich-Kwong are convenient for the description of solutions *via* mixing rules, their accuracy of predicting the thermodynamic properties especially in the vicinity of the critical point are poor. More accurate equations of state such as the extended generalized Bender equation of state accurately predict the thermodynamic properties of the pure solvent, however they are not suitable for calculation of multi-component systems. Consequently, the fluid properties are typically calculated with the more accurate empirical equations of state with the assumption of a pure fluid, while precipitation models use cubic equations of state to represent the solute-solvent systems.

Particle coagulation mechanisms have been introduced into the particle growth models in order to help bridge the discrepancy between experimental and theoretical results[72, 73, 80]. Coagulation of smaller particles becomes significant early in the

expansion process and may continue far downstream of the nozzle. A review of key precipitation and growth mechanisms follows.

4.2.1 Precipitation by Homogeneous Nucleation and Condensation

Initial precipitation from a supersaturated solution occurs by the formation of solute nuclei. Both homogeneous and heterogeneous nucleation mechanisms are possible routes of precipitation. In the case of heterogeneous nucleation, precipitation takes place on a surface of a solid such as the wall of a container or some dispersed particulate matter. Homogeneous nucleation involves the spontaneous formation of nuclei of the dissolved material.

Homogeneous nucleation requires activation energy. The activation energy is required to overcome the nucleation free energy barrier. The thermodynamic driving force for nucleus formation can be described in terms of the supersaturation. For a highly supersaturated solution a small perturbation is sufficient to bring about precipitation. On the surface of a solid, as is the case of heterogeneous nucleation, nucleation is facilitated by the presence of the stable solid phase, reducing the required activation energy and precipitation is facilitated. In the presence of a solid, nucleation takes place at relatively low supersaturation. Spontaneous nucleation is not significant at supersaturation values below *ca.* 4[9].

In the case of homogeneous nucleation, the metastable zone width is much wider prior to condensation. A substantially higher supersaturation level is required prior to a significant onset of precipitation. In this case the necessary free energy is derived from local density and composition fluctuations. Nucleation from a highly supersaturated

solution occurs at a much higher rate since the solute concentration is in large excess of the equilibrium concentration. Rapid nucleation results in a large number of fine nuclei.

Homogeneous nucleation is the predominant nucleation route in the RESS process. Only a small fraction of the fluid is in contact with the nozzle walls during expansion thus the contribution of heterogeneous nucleation is likely negligible. However, it does occur, and may help explain nozzle blockage by the solute.

The classical nucleation theory, which dates back to the 1920's, is still commonly used to describe nucleation processes at low supersaturation levels. The classical nucleation theory is based on several key assumptions. One assumption is that the concentration of nuclei is low and that most of the solute exists as single molecules. This leads to an assumption that the flux of solute to and from the surface of a nucleus occurs via single molecule addition and removal. Another key assumption is that the cluster population is at a steady state[83]. This requirement may be difficult to reach during RESS since the equilibration time required is much shorter than the expansion time[66] and may not be applicable in the fastest expansion stages such as the supersonic free jet. It is also assumed that the critical nucleus size is macroscopic. This assumption may also not be valid for RESS as the critical nucleus size can be as small as a single molecule.

The energetics of nucleus formation can be described by the following expression [84]:

$$\Delta G \cong n(\mu_\infty - \mu_1) + \gamma 4\pi r_i^2 \tag{4.2}$$

where G is the Gibbs free energy, n is the number of molecules in the cluster, μ_∞ is chemical potential of molecules in the condensed state, μ_1 is chemical potential of

molecules in the bulk state, γ is the surface free energy of the cluster, and r_i is radius of the cluster.

The second term on the right hand side of Equation 4.2 accounts for the free energy change during surface formation of the nucleus; this term is always positive. The first term describes the free energy of deposition of molecules on the surface of a cluster. For a supersaturated system this term is negative since the chemical potential of molecules in the bulk state is higher. For a system below the saturation level this term is positive, and the work required for the formation of nucleus is positive and increasing with the nucleus size. The net free energy change of nucleus formation is illustrated in Figure 4.2. ΔG^* corresponds to the free energy of a critical cluster formation with a radius r*. The positive change in the Gibbs free energy is the consequence of the interfacial energy required to form a surface, which is proportional to r^2. The magnitude of the energy required to form a surface will depend on the interfacial tension between the newly formed particle and the solvent. Any further addition of molecules to a cluster with a critical size or larger will happen spontaneously since the process becomes energetically favorable. Clusters below the critical size tend to spontaneously disintegrate. The activation free energy of nucleation is thus the energy required to form a cluster of critical size.
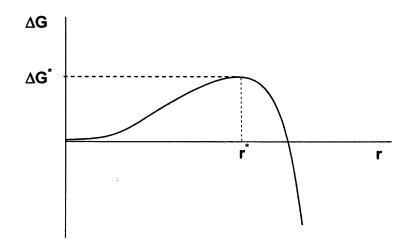
Figure 4.2 Qualitative illustration of the energetics of nucleus formation.

The classical nucleation theory is formulated around the growth kinetics and mechanism of nucleation. The growth process is a competition between the deposition of molecules on the surface of the embryo and the loss of molecules back into the solution. The rate of deposition of single molecules on the surface can be obtained from kinetic theory, however, the rate of loss of single molecules from the surface is not known. The growth rate is determined from the equilibrium size distribution of nuclei where the rate of molecule addition is equal to the rate of molecule loss. This is obtained from the energetics of nucleus formation.

The classical treatment of the nucleation process is based on two primary parameters: the nucleation rate J (nuclei / sec-m^3), and the critical nucleus size n^* (consisting of n^* monomers). The following expressions are used to describe the parameters according to the classical nucleation theory formalism[83]:

$$n^* = \frac{32\pi}{3}\left[\frac{(v')^{2/3}\sigma}{(-\Delta\mu)}\right]^3$$

(4.3)

$$J = 2\beta N_{tot} \sqrt{\frac{\sigma (v')^2}{kT}} \, exp\left[-\frac{16\pi}{3}\left(\frac{\sigma (v')^{\frac{3}{2}}}{kT} \right)^3 \left(\frac{1}{\ln S} \right)^2 \right] \qquad (4.4)$$

where v' is the molecular volume in the condensed phase, σ is the surface tension of the embryo, $\Delta\mu$ is the difference of the solute's chemical potential in the condensed phase and in the solution, β is the flux of molecules onto the surface of the nucleus, N_{tot} is the total number density of the metastable bulk phase. The degree of supersaturation is designated by S. The pre-exponential term describes the molecular collision frequency. The exponential term describes the energetics of nucleus formation.

Equation 4.3 indicates that the size of the critical nucleus has a very strong dependence on the degree of supersaturation, which is implicit in the value of $\Delta\mu$. As the supersaturation increases the critical nucleus size becomes smaller. Equation 4.4 indicates that the nucleation rate is driven by the degree of supersaturation. Higher supersaturation leads to a higher nucleation rate.

The applicability of the classical nucleation theory to the RESS process is most appropriate at the subsonic stages of expansion, where the supersaturation is relatively low ($<10^3$). Poor applicability can be expected in the free jet where the supersaturation can be in excess of 10^6. It was demonstrated by Chesnokov and Krasnoperov using a thermodynamically consistent kinetic model of nucleation that at very high supersaturation levels, due to high monomer depletion resulting from condensation on nuclei, a steady state was never reached[69]. A key requirement of the classical nucleation theory is that a steady state exists during nucleation.

At supercritical fluid conditions, especially in the vicinity of the critical point, fluid phase non-ideality can be very significant. Debenedetti accounted for the effect of

fluid non-ideality on the nucleation parameters[66]. A coefficient K was introduced as a measure of the non-ideality, which accounts for the influence of the fluid phase non-ideality on the energetics of embryo formation. A maximum for K lies near the critical point. It was demonstrated that due to the non-ideal fluid behavior, a supersaturation limit exists, beyond which the solution becomes unstable and may undergo spinodal decomposition. The supersaturation limit depends on K according to:

$$S_{max} = (Ky_1^e)^{-1} \tag{4.5}$$

where y_1^e is the equilibrium solute mole fraction. A correction to the nucleation expression was proposed to account for such non-ideality. The expression for the critical nucleus size as well as for the rate of nucleation were modified by correcting the ideal case nucleation driving force $\ln S$ by subtracting the term $Ky_1^e(S-1)$ resulting in the following expressions corresponding to Equations 4.3 and 4.4 respectively:

$$n^* = \frac{32\pi}{3}\left[\frac{(v')^{2/3}\sigma}{(kT)}\right]^3\left[\frac{1}{\ln S - Ky_1^e(S-1)}\right]^3 \tag{4.6}$$

$$J = 2\beta N_{tot}\sqrt{\frac{\sigma(v')^2}{kT}}\exp\left[-\frac{16\pi}{3}\left(\frac{\sigma(v')^{3/2}}{kT}\right)^3\left(\frac{1}{\ln S - Ky_1^e(S-1)}\right)^2\right] \tag{4.7}$$

At lower pressures where the fluid approaches ideal behavior, these corrections are not necessary and no thermodynamic limit on the extent of supersaturation exists.

Calculations by Turk show that the supersaturation in a free jet expansion of a supercritical solution can reach values as high as 10^8. The corresponding nucleation rate would be around 10^{26} $(cm^{-3}$ $s^{-1})$[67].

Nuclei larger than the critical size will grow by solute condensation. This process continues until all the solute in the bulk phase is exhausted. Beyond nucleation and condensation the growth of particles is expected to continue due to coagulation. This phenomenon is likely responsible for the very large particles often observed in experimental studies.

4.2.2 Particle Growth by Coagulation

Coagulation is a growth mechanism which occurs by fusion of smaller particles. The driving force for coagulation is the reduction in the specific surface energy which increases with decreasing particle size[85]. Coagulation is believed to be relevant during RESS and is likely responsible for particle growth to sizes beyond what is expected from nucleation and condensation alone.

The particle size of solids precipitated by RESS is usually significantly larger than the particle size expected due to homogeneous nucleation and condensation of the solute. Calculations based on the homogeneous nucleation and condensation indicate that the mean size of particles produced by RESS should be below 50 nm for most systems[69]. Weber et al. showed that for long capillary nozzles, up to 100 mm, the particle size due to precipitation inside the nozzle by homogeneous nucleation and condensation are not expected to exceed 100 nm in diameter[73].

The actual particle size of solids recrystallized by RESS is often in the range from around 100 nm to microns[39, 76]. Such large discrepancy indicates that a mechanism of particle formation involving only homogeneous nucleation and condensation does not adequately describe the entire crystal growth process. Coagulation is believe to be responsible for the large particle size obtained in experimental studies[68, 76, 80].

Mohammed et al. observed an effect of the post-expansion pressure and temperature on the particle size of naphthalene produced by RESS[39]. This observation has an implication that the final particle size may not result solely due to homogeneous nucleation and condensation, which should be nearly completed just outside of the nozzle, and that downstream of the nozzle additional mechanisms may play a very significant role. Matson et al. also observed that unexpectedly large particle were formed by RESS and suggested that coalescence of small nuclei in the expansion jet by coagulation may be responsible for the large particle size[76]. Supporting evidence for coalescence of nuclei was suggested based on the observation that increasing solute concentration resulted in an increase of the particle size and a wider particle size distribution. The higher concentration was suggested to lead to a higher number density of nuclei which would coalesce upon collision. This trend contradicts that predicted by the classical nucleation theory. According to the classical nucleation theory the final particle size should decrease as a result of increased solute concentration.

Helfgen et al. estimated that the number concentration of particles at the Mach disk(defined in Chapter 8) can exceed 10^{14} cm^{-3}. It was shown that at values above ca. 10^8 characteristic times for coagulation should be well within the residence times in a typical RESS jet[68].

The conditions downstream of the nozzle have a pronounced effect on the particle size[86]. Using an empirical expression for coagulation, Turk showed that coagulation may be relevant during particle formation inside the nozzle as well as in the free jet due to the estimated characteristic time for particle collision being substantially lower than the residence time[72]. Weber et al. suggested that a substantial amount of coagulation may occur within the transonic section in the vicinity of the Mach disk due to high shear forces associated with abrupt deceleration as well as pressure spike[73].

Several mechanisms have been considered in the literature to describe the coagulation of aerosol particles. These include coagulation due to particle-particle interaction resulting from Brownian motion, interaction resulting from shear forces due to laminar and turbulent flows, and interaction due to collisions resulting from the relative motion between the particles and the continuous phase[80].

Weber and Thies provide a thorough description of the various coagulation mechanism responsible for particle growth during RESS[80]. Collision of particles leading to coagulation may occur as a result of Brownian motion. This mechanism is relevant in both moving as well as stagnant solutions. The expression derived for coagulation via Brownian motion of particles is as follows:

$$D_p(t) = \left[\omega^{BM}\xi t + 1\right]^{1/3} D_{p,0} \qquad (4.8)$$

$$\omega^{BM} = \ln(2)\left[\frac{8k_B T}{\eta_{gas}}\right]\left[\frac{\varphi_p}{\pi/6(D_{p,0})^3}\right]$$

$D_p(t)$ is the particle diameter as a function of time, $D_{p,0}$ is the starting diameter of particles prior to coagulation, ω^{BM} is the particle collision frequency due to Brownian motion, φ_p is the fraction of precipitated material, k_B is the Boltzman contant, ξ is the collision efficiency leading to coagulation of two particles.

As the particle size increases, coagulation by shear stresses due to localized fluid velocity gradients may become significant. This can occur in both laminar as well as turbulent flows. The expression for coagulation due to shear stresses is:

$$D_p(t) = \exp[\omega^{SF} \xi\, t] D_{p,0} \tag{4.9}$$

$$\omega^{SF} = \frac{16}{\pi} \ln(2) k^{SF} \varphi_p$$

A third mechanism is proposed to account for the relative motion between the particles and the fluid. The expression describing such coagulation follows:

$$D_p(t) = [1 - \omega^{RM} \xi t + 1]^{-1} D_{p,0} \tag{4.10}$$

$$\omega^{RM} = A D_{p,0} F(g) \frac{\varphi_p}{\pi / 6}$$

Calculations based on coagulation due to Brownian motion indicate that the characteristic growth time are relatively slow and cannot explain the rapid growth of particles downstream of the nozzle. It was shown that the growth of particles by coagulation due to Brownian motion would require several seconds to achieve 1 micron particle size. This calculation was not sensitive to the initial nucleus size. Such long time-scale contradicts the experimental observations where micron size particles were collected in the near vicinity of the nozzle exit, which would indicate total growth time

scales of well below one second. Calculation of the growth time to reach 1 micron size by coagulation due to slip flow particle interaction yielded a time of 11 ms. This is at least an order of magnitude faster than coagulation due to Brownian motion and may be dominant during RESS.

Coagulation of newly formed solute particles during precipitation may influence the precipitation process[70]. Reduction of the particle surface area resulting from coagulation reduces the available surface for condensation of solute and thus may promote nucleation. This may lead to the formation of a larger number of nuclei and consequently the final particle size will depend less on growth by condensation and more on growth by coagulation.

Weber et al. showed that the contribution of coagulation to particle growth inside a short orifice nozzle can become very significant as the pre-expansion pressure increases[73]. Calculation of precipitation of phenanthrene during expansion across a nozzle with a 40 μm ID and 200 μm length showed that the contribution from coagulation inside the nozzle was less than 20 % for pre-expansion pressures below 230 bar, while for pressures above 260 bar as much as 85 % contribution was expected. It was also observed that the extent of solute precipitation inside the nozzle increases with pre-expansion pressure.

It is evident that reduction of the final particle size may be achieved by limiting the extent of coagulation. Several processing approaches may be considered to accomplish this. One such approach is based on the minimization of the residence time available for coagulation. This can be accomplished by reducing the volume of the expansion chamber[81].

Dilution of the expansion chamber by air addition was also demonstrated to limit coagulation. As the air flow rate into the expansion chamber increased, the mean particle size of benzoic acid precipitated from carbon dioxide was reduced[68]. It was suggested that dilution of the expanded gas lowers the probability of collision and thus limits coagulation.

Another approach demonstrated to mitigate the effects of coagulation was by co-precipitation of two solids. Turk demonstrated that precipitation of phytosterol from carbon dioxide in the presence of eudragit limited coagulation and resulted in a smaller particle size of the final product[87]. A similar approach was employed by Thakur and Gupta. Menthol was added to the system of carbon dioxide with the target solute. The presence of menthol not only dramatically increased the solubility of the target solutes 2-aminobenzoic acid[88] and griseofulvin[77]in supercritical carbon dioxide, but also led to a particle size reduction which was suggested was due to coagulation inhibition by menthol.

4.3 Summary

Due to the abrupt change in the solubility during the rapid expansion of supercritical solutions, precipitation of the solute occurs on a very short time scale leading to the formation of small particles. Particle formation and growth along the expansion axis during RESS occurs *via* several mechanisms which are dependent on the local conditions of the jet. The onset of precipitation, which depending on the process conditions may occur upstream, inside, or downstream of the nozzle, is expected to begin *via* homogeneous nucleation accompanied by solute condensation. Nucleation and

condensation account for particle growth to sizes substantially smaller than 100 nm for most cases. Another important growth mechanisms involved in the RESS process is coagulation. Coagulation is believed to be responsible for the large particles size, well above a micron, often observed in RESS experiments. Conditions that favor coagulation include a high number density of particles and highly turbulent flow. Limiting the coagulation of precipitated particles is essential if small crystal size is desired.

CHAPTER 5

SOLUBILITY ANALYSIS

Knowledge of solubility dependence on the temperature and pressure of the supercritical solvent is necessary for understanding and optimization of the RESS process. Two experimental techniques were investigated for the purpose of solubility measurement of RDX in supercritical carbon dioxide. These were solubility analysis by cloud point observation and by ultraviolet (UV) spectroscopy.

5.1 Solubility Analysis by Cloud Point Observation

Solubility determination of RDX in supercritical CO_2 was attempted using a Thar Technologies Phase Equilibrium Analyzer (PEA). This apparatus allows the determination of the saturation temperature and pressure by direct visual observation of the cloud point formation. The cloud point is defined as the point where the solution transitions from a transparent to an opaque state. Such transition occurs when a sufficient amount of precipitate is formed. From the cloud point pressure and temperature the solubility curves can be constructed.

5.1.1 Experimental Set-Up

The schematic of the phase analyzer is illustrated in Figure 5.1. The instrument consists of a variable volume view cell, with maximum volume of 25 cm^3. The cell volume is varied with a motor driven piston. The contents of the high pressure cell can be seen

through a 7/8 inch sapphire window located on the bottom lid. A camera is directed at the window feeds a live image to the monitor.

The contents of the cell are stirred with a mechanical stirrer which is located on the bottom of the piston. Heating of the cell is achieved by circulation of heating oil through the heating jacket. Temperature and pressure readings are directly fed to the PC. A software package provides the means to control the fluid parameters. A syringe pump with internal volume of 300 cm^3 is used to fill the view cell with liquid CO_2 at the desired density. The syringe pump is filled directly from a liquid CO_2 cylinder. This apparatus allows operation at pressures up to 6,000 psig and temperatures up to 130 °C.
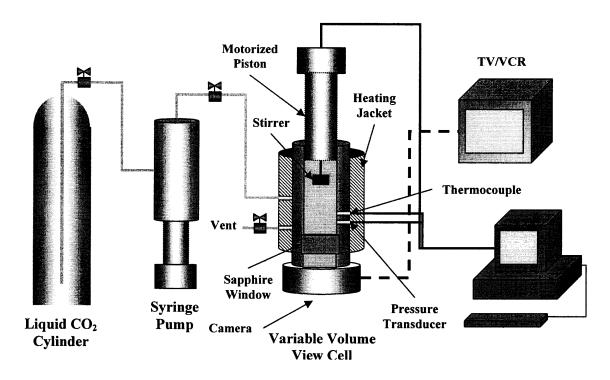
Figure 5.1 Schematic of high pressure phase equilibrium analyzer.

5.1.2 Procedure

The solute is weighed and placed inside the view cell. The piston is inserted and sealed. The air inside the cell is flushed by pressurization and discharging with carbon dioxide. Before the cell is filled with CO_2, the cell volume is reduced down to around 50 % of the maximum volume. This is necessary so that a sufficient range of expansion will be available during the depressurization step of the analysis. The syringe pump is filled with CO_2 from the liquid CO_2 cylinder. Filling with liquid phase is achieved by retracting the piston with the volume connected to the liquid CO_2 cylinder. Next the valve to the cylinder is closed and compression of the CO_2 with the syringe pump is initiated. Once the desired pressure is reached, pumping is stopped, and the valve to the view cell is closed. At this point heating and stirring is initiated. Once the set temperature is reached, manipulation of the view cell volume is possible to achieve the desired pressure. Experimental measurements are commonly performed isothermally.

Dissolution of the solid which is located on the sapphire window is observed on the monitor. Once the disappearance of the solid phase is visually observed, expansion of the view cell volume is started by retracting the piston. Expansion rate is controlled with the PC based control software. When the solvent density drops below the saturation point, cloud formation is observed on the monitor. In order to accurately determine the saturation point, the cell is pressurized again to a pressure a few bar above the initially observed cloud point pressure. Next the cell is again expanded but at a slower rate. This sequence may be repeated a number of times, each time decreasing the expansion rate, with a more accurate saturation conditions reading. Additional saturation points may be

determined without reloading the reactor. This can be done by changing the temperature and repeating the above procedure.

The view cell is typically situated in one of two positions. For solids dissolution analysis, normally the cell is fixed in a vertical position. In this case most of the loaded solid is dispersed directly on the window. Following dissolution, the visual observation of the solid disappearance is sufficient for confident confirmation that the solid is in solution. Another option is to perform the analysis with the cell in a horizontal position. With solids this is normally undesirable since a difficulty arises in observing the disappearance of the solid. However, when investigating the miscibility of liquid / gas systems, horizontal arrangement is preferred since the liquid / gas interface can be observed.

5.1.3 Results

Solubility of RDX in supercritical carbon dioxide was studied at pressures up to 350 bar and temperatures of up to 100 °C. The solubility was also analyzed in acetone-modified carbon dioxide. The acetone concentration was varied from 2 to 15 mole %. No observation of a cloud point was made for the entire range of conditions investigated. This suggests that the solubility of RDX was low, and the amount of precipitate was insufficient for visual observation. Based on the existing solubility data of RDX it appears the cloud point analysis is inappropriate with materials with solubility below *ca.* 100 ppm. A method with higher sensitivity is required for such poorly soluble substances.

5.2 Solubility Analysis by UV Spectroscopy

Solubility measurement of RDX in supercritical carbon dioxide was attempted using UV absorption spectroscopy. This is a significantly more sensitive method compared to cloud point observation.

5.2.1 Experimental Set-Up

The set-up consists of a 316 stainless steel high pressure cylindrical view cell. Two ½ inch thick quartz windows are located opposite to one another at the end caps of the cell. Quartz is transparent in the UV spectrum of interest. The optical path of the cell is 1.16 cm. The internal volume of the cell is 0.425 cm^3. The design of the window mounting and pressure sealing is illustrated in Figure 5.2.
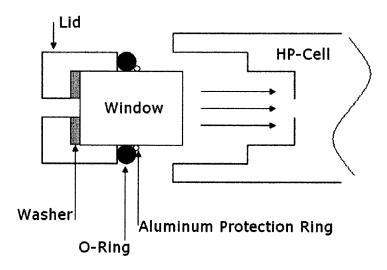
Figure 5.2 Schematic of high pressure view cell end-cap.

The quartz windows are supported by stainless steel window retainers with a PEEK washer in between. High pressure sealing is achieved using viton o-rings. Aluminum rings were installed on the high pressure side of the o-rings in order minimize the

dissolution of materials from the o-rings which were detectable and interfered with the measurement of the target solute. There are two 1/8 inch ports on the wall of the high pressure cell. A thermocouple probe was inserted into one of the ports and feed tubing into another.

The schematic of the experimental set-up is illustrated in Figure 5.3. A manually operated piston screw pump by HiP Inc. was used to pressurize the view cell volume. 1/16 inch high pressure stainless steel tubing was used as the feed line. The cell was wrapped with resistive heating tape. Cell temperature was controlled using a temperature controller with 0.1 °C accuracy. Pressure inside the cell was determined at the time of filling via a pressure gauge. A steel stirring bar was used to accelerate dissolution. The bar was actuated by an alternating magnetic field from an external source.
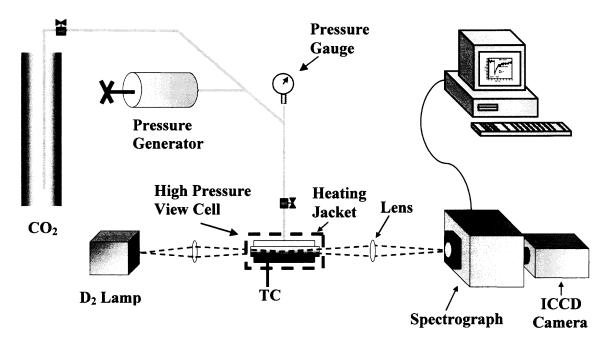
Figure 5.3 Schematic of high pressure spectroscopy set-up.

A deuterium lamp (Oriel) was used as the ultraviolet light source. A deuterium light source was chosen due to its emission stability. An optical lens was positioned between the lamp and the view cell such that the light would be focused at the center of the view cell. A second lens was installed to focus the emerging light from the view cell onto the entrance slit of the spectrograph. An Acton, SpectraPro 300i spectrograph with a grating blazed at 300 nm was used to direct the desired spectrum onto the Princeton Instruments ICCD-Max intensified charged coupled device (ICCD) camera. The ICCD camera enables the simultaneous acquisition of a full spectrum with tunable sensitivity. The spectra frames were transferred to a PC and processed using WinSpec (Princeton Instruments) software.

5.2.2 Procedure

The solute was loaded into the cell by injecting a measured volume of RDX/acetonitrile solution with a carefully prepared composition, typically 10^{-2} M. A Hamilton 25 µL syringe was used for injection. Acetonitrile was used due to its low absorption in the UV spectrum of interest. The solvent was allowed to evaporate prior to sealing the view cell. The assembled and sealed view cell was mounted and heated to the desired temperature.

Prior to pressurizing the view cell flushing was performed to eliminate air. The cell was flushed several times with carbon dioxide. This was done by filling and venting at low pressures (< 10 bar) in order to avoid flushing of the loaded RDX. Next the cell was pressurized. The system volume including the pressure intensifier was filled with carbon dioxide from a liquid cylinder. The cylinder outlet valve was closed and the pressure was elevated to the desired value by compression with the manual pressure

intensifier. Time was allowed for thermal stabilization of the carbon dioxide prior to sealing the cell by closing the inlet valve. Pressure reading was not possible after sealing.

Measurements were made in series of two runs to determine the absorbance of RDX. The first run was performed with pure carbon dioxide and the second with RDX. This was done in order to correct for the baseline shifts caused by supercritical CO_2 at high pressures.

UV spectra were taken intermittently after sealing of the view cell. The absorbance was monitored over time in order to determine whether complete dissolution had been achieved. Once a plateau in absorbance was established the measurement spectra were recorded.

Solubility at a given temperature and pressure was determined by a series of experiments with increasing RDX loading. Saturation of the supercritical solution was indicated by a plateau in the absorbance vs. loaded amount of RDX. The concentration of RDX at the onset of the plateau was taken as the solubility.

5.2.3 Results

The absorbance spectra of RDX in supercritical carbon dioxide were acquired at 80 °C and 275 bar as a function of RDX loading ranging from $1 \mu L$ to 80 μL of 10^{-2} M solution of RDX in acetonitrile. The dependence of absorbance on the loaded amount of RDX at 225, 246, and 260 nm is shown in Figure 5.4. Inspection of the absorbance curve reveals a non-linear response above RDX loading of around 10 μL of 10^{-2} M solution of RDX. This non-linearity is especially pronounced at the 225 nm wavelength, however not very

significant at the longest wavelength. The source of such wavelength specific effect is not known.
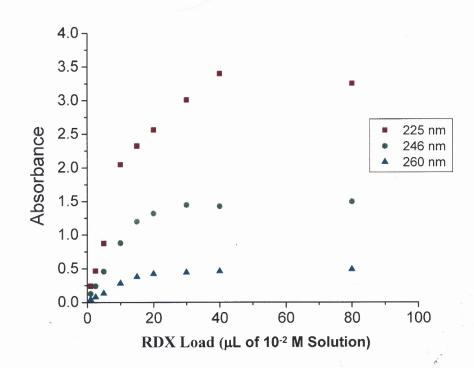
Figure 5.4 Absorbance at 225, 246, and 260 nm vs. RDX loading in supercritical carbon dioxide at 80 °C and 275 bar.

The solubility of RDX in carbon dioxide at 80 °C and 275 bar was determined based on the absorbance at 246 nm as shown in Figure 5.5. This was done by locating the loaded RDX quantity corresponding to the onset of saturation, which is evident in the plateau in Figure 5.5. The solubility was found to be 0.108 ± 0.006 mg of RDX / g of carbon dioxide. This result is in close agreement with the value obtained by Morris at the same conditions: 0.114 mg of RDX / g of CO_2[2]. The RDX solubility results based on the work of Morris are shown in Figure 3.2.
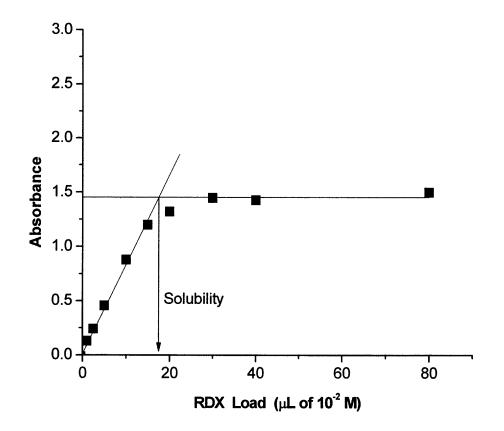
Figure 5.5 Determination of phase equilibrium of RDX in supercritical carbon dioxide at 80 °C and 275 bar from the absorbance plateau at 246 nm.

Morris utilized a flow cell arrangement for UV solubility measurements. A major drawback of the flow cell approach is the inability to determine the absolute concentration of the solute. Thus, the extinction coefficient cannot be measured. Morris relied on the absorbance of RDX in acetonitrile to calibrate the absorbance in carbon dioxide. The solubility calculations by Morris were made with the assumption that shifting of the spectrum to correct for the wavelength shift was sufficient to relate the absorbance in acetonitrile to the absorbance in supercritical carbon dioxide. Comparison of the absorption spectra of RDX in acetonitrile and RDX is shown in Figure 5.6.
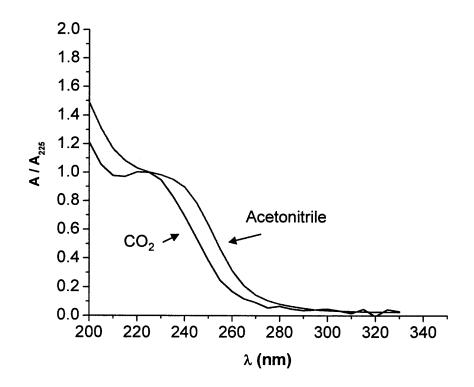
Figure 5.6 Absorption spectra of RDX in acetonitrile and carbon dioxide normalized to absorption in carbon dioxide at 225 nm.

In the closed view cell arrangement used in this work, the concentration of RDX is known, thus it is possible to directly measure the extinction coefficient of RDX in supercritical carbon dioxide. With known concentration of solute and measured absorbance the extinction coefficient may be determined using the well known Beer-Lambert law[64]:

$$A = \varepsilon\,[c]\,l \tag{5.1}$$

where A is the absorption, ε is the extinction coefficient, c is the concentration of the solute, l is the optical path length.

The extinction coefficient of RDX in supercritical carbon dioxide at 80 °C and 275 bar as a function of wavelength is shown in Figure 5.7. The extinction coefficient of RDX in supercritical carbon dioxide calculated from absorbance data at 225 nm is $\varepsilon_{225} = 0.95 \pm 0.09 \times 10^4$ L mol^{-1} cm^{-1}.
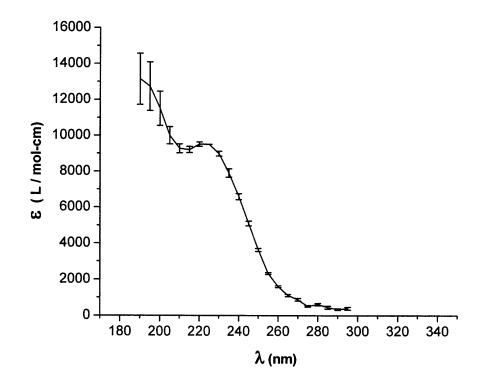
Figure 5.7 Extinction coefficient of RDX in supercritical carbon dioxide at 80 °C and 275 bar as a function of wavelength.

The similarity in the solubility determined in this work with the data of Morris validates the assumption made by Morris for the system of RDX / carbon dioxide.

5.3 Conclusions

The measurement of solubility by cloud point formation as well as by UV spectroscopy was investigated. Due to the low solubility of RDX in carbon dioxide, the cloud point approach was found not to be applicable because the precipitate was not visually detectable. The method based on UV spectroscopy was successfully utilized to determine the absolute solubility of RDX. Due to the closed cell arrangement, the concentration of RDX was known, enabling the accurate determination of the extinction coefficient of RDX in carbon dioxide. The results obtained here validate the published results for a wide range of pressures and temperatures which were obtained using an assumed extinction coefficient[2].

CHAPTER 6

RECRYSTALLIZATION OF RDX BY RESS

In this chapter the experimental high pressure setup assembled for recrystallization of RDX by rapid expansion of supercritical solutions is described. The solvent used in the study was carbon dioxide. The experimental results are examined. These include the effects of the pre-expansion temperature and pressure as well as the nozzle diameter on the particle size of RDX resulting from the rapid expansion to atmospheric pressure. The physical properties of the recrystallized RDX are characterized and compared to the properties of the precursor.

6.1 Materials

Production grade RDX containing around 10 % HMX was used as the precursor material. 99.5 % purity reagent grade acetone was obtained from Aldrich. 3 mm glass beads were obtained from Fisher Scientific. "Bone Dry" grade carbon dioxide from Praxair was used as the solvent. The solubility of RDX in carbon dioxide has been reported over a temperature range 303-353 K and pressure range 69-480 bar [12]. The data are shown in Figure 3.2. At pressures above 150 bar, the solubility of RDX increases with pressure and temperature with a maximum measured solubility of about 0.25 mg of RDX/g of CO_2 at 480 bar and 353 K. Below the critical point the solubility becomes negligible. The solubility appears to reach a plateau above 400 bar for the entire range of extraction temperatures studied.

6.2 Experimental Set-Up

An experimental set-up was assembled in order to investigate the recrystallization of RDX by RESS. A schematic of the experimental set-up is illustrated in Figure 6.1. The set-up consists of a Thar P-200 dual piston high pressure liquid pump with chilled piston heads for efficient pumping of carbon dioxide. The pump is rated for discharge pressures up to 400 bar and flow rates up to 200 g/min. The feed carbon dioxide is supplied from a liquid cylinder fitted with an eductor tube. The eductor tube is required in order to feed the liquid phase carbon dioxide from the bottom of the cylinder as the carbon dioxide at the top of the cylinder is in the vapor phase. The feed was chilled to around 5 $^{\circ}$C in order to minimize flashing during the filling of the pump pistons. Without chilling the pumping efficiency drastically decreases due to vapor formation inside the pistons. The pistons are also externally chilled in order to limit evaporation of carbon dioxide inside the pistons since the pistons are heated during compression. A rupture disk with a pressure rating of around 5000 psi is located at the pump outlet and is designed to protect the pump from overpressure in case of flow blockage downstream of the pump.

The compressed carbon dioxide was pre-heated to the desired extraction temperature in an electrical heater prior to entering the extraction vessel. The extraction of RDX occurred inside a 1 liter high pressure stainless steel vessel. The vessel was heated with an electrical heating jacket. RDX was loaded into the extraction vessel by depositing the RDX onto glass beads and filling the vessel with the coated glass beads. The beads were coated with RDX by spraying a saturated acetone solution onto heated glass beads. As the solvent evaporated a deposit of RDX was formed on the surface of the beads. 3 mm spherical glass beads were used in the experiments.
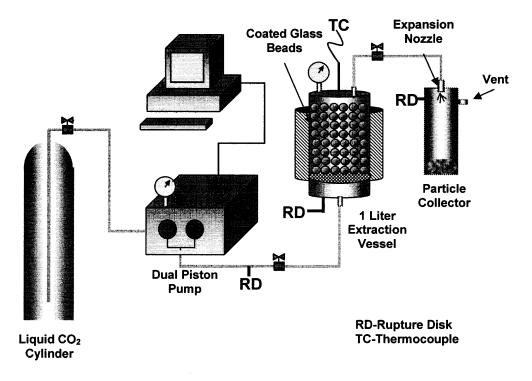
Figure 6.1 Experimental set-up.

Glass beads were used to enhance the dissolution of RDX. The supercritical fluid was fed to the vessel via 1/8 inch stainless steel tubing to a feed port on the bottom of the vessel. The vessel was fitted with a rupture disk rated at 5000 psig in case of accidental overpressure. The extraction temperature was measured with a thermocouple inserted into the extraction vessel through a port. The tip of the thermocouple was located near the exit port of the vessel.

The saturated RDX/CO_2 solution was transferred through a 1/16 inch high pressure stainless steel tubing to the temperature controlled nozzle assembly. The transfer tubing was wrapped with heating tape and heated slightly above the extraction temperature in order to prevent cooling of the solution which may result in premature precipitation of the solute. The nozzles used for expansion were laser drilled short

sapphire orifices with a 100 and 150 µm internal diameter and a 250 µm length. The orifices had a tapered inlet followed by a constant diameter duct. The orifices were fitted inside of the heated stainless steel housing containing heating cartridge and thermocouple ports.

The process parameters were controlled with PC based software by Thar Technologies. All the heating zones as well as the pump were controlled via the PC interface. The pumping rate was controlled to maintain a set pressure. Pressure limits were set using the control software. In case of overpressure the pumping was automatically shut down.

6.3 Collection of Recrystallized RDX

The collection of the aerosol RDX particles from the expanded gas was initially attempted by a cyclone collector supplied by Thar Technologies. It was discovered however that collection of fine crystals from a dilute gas suspension was not at all efficient by centrifugal action of the cyclone. Due to the small particle size, the precipitated crystals tend to follow the streamlines of the flowing gas, thus most of the product was vented out with the carbon dioxide. Small quantities were collected on the vessel walls.

In order to improve the collection efficiency a particle collection by sedimentation was investigated. The nozzle assembly was coupled to the top of a tubular collection vessel which was made from a clear plastic. The vessel was mounted vertically as shown in Figure 6.2. The vessel was vented to atmospheric pressure via an exit port open to

atmosphere. A relief valve set to around 30 psig was installed on the vessel in case of overpressure due to flow blockage.

As the carbon dioxide / RDX solution expands across the nozzle to atmospheric pressure both the solute and carbon dioxide precipitate. The solute is believed to precipitate before carbon dioxide. As will be demonstrated in Chapter 8, this is expected due to earlier supersaturation of the solute. It appears that the condensation of carbon dioxide is assisted by the presence of RDX precipitate which serves as seeds for the heterogeneous condensation of carbon dioxide. Due to the low post-expansion pressure, below its triple point pressure, solid phase carbon dioxide was precipitated.

The extent of carbon dioxide condensation is determined by the pre-expansion pressure and temperature of the supercritical solution as well as the pressure and temperature downstream of the nozzle. At atmospheric discharge pressure the downstream temperature plays a key role. At typical pre-expansion conditions in this study, the expansion into a chamber with ambient temperature and pressure resulted in minimal visible condensation of carbon dioxide. As a result nearly all of the precipitated RDX was lost with the vented gas. It was observed that when a larger fraction of carbon dioxide condensed large, visible agglomerates of dry ice formed and precipitated to the bottom of the collection vessel. The precipitated dry ice contained essentially all of the RDX precipitated. The quantity of recovered RDX matched the expected amount based on the solubility of RDX at the process conditions. This is an indication that condensation of carbon dioxide occurred heterogeneously on the surface of the precipitated RDX. The RDX nanoparticles were recovered by sublimation of the dry ice.

In order to condense an adequate fraction of carbon dioxide that can lead to large enough agglomerate size for gravitational sedimentation, the temperature in the collection vessel must be sufficiently low. At the onset of expansion the temperature in the vessel is steadily cooled by the cold expanding carbon dioxide. As the vessel cools, the conditions for carbon dioxide condensation become more favorable. Consequently, the vessel temperature reached a steady value with sufficient condensation of carbon dioxide for the formation adequately large agglomerates for gravitational sedimentation.

Such effect of the expansion vessel temperature on the condensation of carbon dioxide is expected. The expanding jet entrains gas from the surroundings. If the temperature of the surrounding gas is warm, the entrained gas will cause a rise in the jet temperature which will limit condensation of the carbon dioxide. However, as the temperature of the entrained gas decreases a larger fraction of carbon dioxide can condense.

During long duration runs, the precipitated dry ice accumulated inside the collection vessel. Applying heating to the bottom of the vessel helped limit this accumulation by aiding in the sublimation of the collected dry ice and thus enabling longer duration processing. The process was typically run continuously for several hours at a time generating sample quantities on the order of several grams.

6.4 Procedure

Glass beads were coated with RDX and loaded into the extraction vessel. The vessel was sealed. The system air was flushed by filling with carbon dioxide to *ca.* 10 bar from the carbon dioxide cylinder and discharging. The chiller was turned on and allowed to reach

the set point which was 0 °C. Next, the cylinder was fully opened and pumping of carbon dioxide was initiated at a slow pumping rate. Heating of the extraction vessel and in the pre-heater was also started. The extraction vessel was pressurized keeping the vessel outlet valve closed. Once the set point pressure was achieved the extractor outlet valve to the nozzle was opened and expansion began. The temperature of the nozzle housing was set to the desired value. The pumping rate automatically adjusted in order to maintain the pressure.

At the start of expansion the collection vessel was at room temperature. During the first 5-10 minutes of expansion no collection of product occurred as the condensation of carbon dioxide was insignificant. As the collection vessel was cooled by the expanding gas, condensation of carbon dioxide intensified. Collection of product began as the carbon dioxide condensate reached a sufficient size to settle to the bottom of the expansion vessel. A steady expansion temperature was achieved and was typically maintained for the duration of the run. At the end of the process pumping was stopped and the vessel outlet valve was closed. All heaters were shut off. The collected dry ice was transferred into a storage container and was allowed to stand until sublimation of carbon dioxide was completed. The recrystallized RDX remained in the container.

6.5 Product Characterization

Particle size and shape analysis was performed by microscopy with a LEO 1530 VP Field Emission Scanning Electron Microscope. Typically, the variable pressure mode, In-Lens detector, low voltages, fast scan rate and small aperture were employed for all samples. Before analyzing, the samples were coated with carbon using a BAL-TEC MED 020 HR

Sputtering Coater. Image-Pro Plus software by Media Cybernetics was used for image analysis, particle size measurements and size distribution calculations.

Thermal properties were analyzed with a Perkin Elmer Diamond DT/TGA. Powder X-ray diffraction analysis was performed with a Scintag 2000 diffractometer. Chemical composition was analyzed by Waters 2695 HPLC.

6.6 Effect of Process Conditions on the Particle Size

The effect of the pre-expansion conditions including temperature and pressure on the RDX particle size was investigated. The post-expansion pressure was atmospheric. The particles were collected by sedimentation with dry ice encapsulation.

Experiments were performed by varying the pre-expansion pressure in the range from 100 to 350 bar at the isotherms of 50, 70, and 90 °C. A 100 μm ID nozzle was used in this set of experiments. The effect of the pre-expansion temperature and pressure on the particle size is shown in Figure 6.2. As can be seen in the figure, at the lower temperature isotherms of 50 and 70 °C, the particle size tends to decrease with increasing pressure. However, at the 90 °C isotherm a moderate increase in the particle size with pressure was observed.
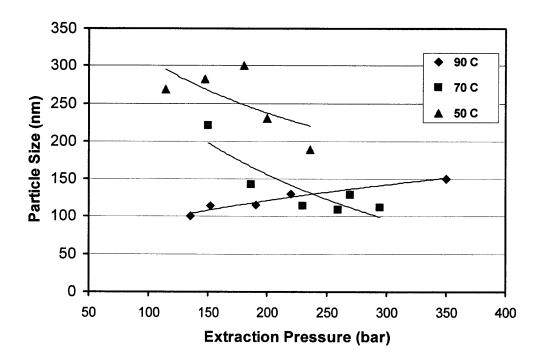
Figure 6.2 Effect of the extraction pressure on the RDX particle size at 50, 70, and 90 °C extraction temperatures.

For the 70 °C isotherm, the effect of the pre-expansion pressure on the particle size and size distribution is illustrated in Figure 6.3. The size distributions were obtained by fitting data obtained from SEM image analysis. The particle size distribution is best fitted with a lognormal distribution function. It can be seen that increasing pressure leads to a decrease in the particle size at 70 °C in the pressure range from 150 to 295 bar. However, at the higher pressure range (230-295 bar) this dependence becomes weaker. The particle size distribution narrows as the pre-expansion pressure increases.
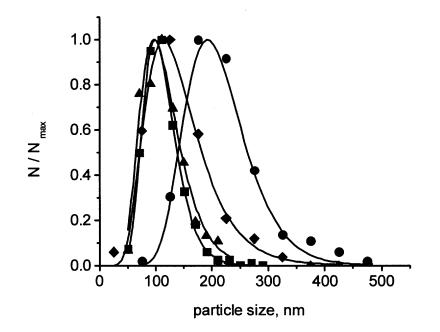
Figure 6.3 Size distribution functions (solid lines) fitted to experimental data (symbols) for RDX produced by expansion from 70 °C and 150 (●), 186 (◆), 230 (▲) and 295 bar (■). N is the number of particles in a bin, N_{max} is the number in the maximum bin.

Sample SEM images of particles produced at different pre-expansion conditions are shown in Figures 6.4 through 6.8. In Figure 6.4, an SEM image is shown of RDX recrystallized with pre-expansion pressure set to 180 bar and temperature set to 50 °C. The supercritical solution was expanded to atmospheric pressure across a 100 μm nozzle.

Figure 6.4 SEM image of RDX recrystallized by expansion from 180 bar and 50 °C to atmospheric pressure.

SEM images of recrystallized RDX particles produced with pre-expansion temperature set to 70°C and pre-expansion pressures set to 295 and 150 bar are shown in Figures 6.5 and 6.6 respectively. SEM images of RDX recrystallized with 90 °C pre-expansion temperature and 135 and 350 bar pre-expansion pressures are shown in Figures 6.7 ad 6.8 respectively.
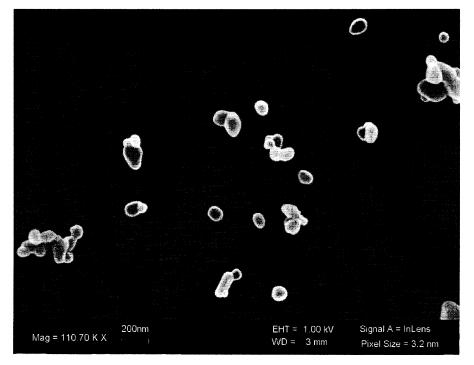
Figure 6.5 SEM image of RDX recrystallized by expansion from 295 bar and 70 °C to atmospheric pressure.
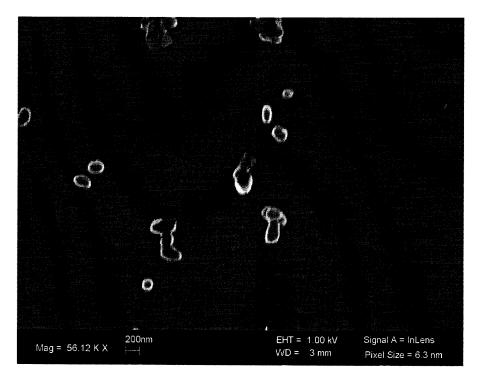
Figure 6.6 SEM image of RDX recrystallized by expansion from 150 bar and 70 °C to atmospheric pressure.
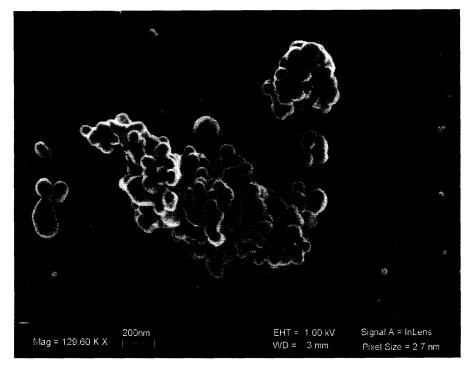
Figure 6.7 SEM image of RDX recrystallized by expansion from 135 bar and 90 °C to atmospheric pressure.
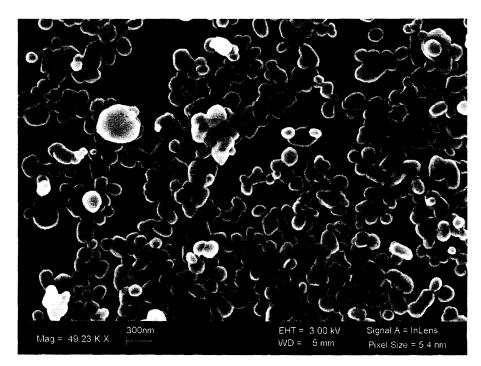
Figure 6.8 SEM image of RDX recrystallized by expansion from 350 bar and 90 °C to atmospheric pressure.

In general the recrystallized RDX crystals appear to have a spherical or oval shape with no apparent crystal facets. Such crystal shape is expected due to the very short time scale of crystal formation. As was discussed in Chapter 4, it is expected that coagulation plays an important role in the final stages of crystal growth in the expanding gas and thus influences the final particle size and shape. The near spherical crystal morphology is consistent with the particle morphology expected from coagulation.

At the 50 and 70 $^{\circ}$C isotherms shown in Figure 6.2, the observed size reduction with pre-expansion pressure appears to be qualitatively in agreement with the classical nucleation theory. The solubility of RDX in CO_2 increases with pressure. Higher solute concentration should lead to a higher supersaturation upon expansion. As the supersaturation increases, the critical nucleus size decreases and the nucleation rate increases. This leads to a higher concentration of critical nuclei and consequently to a smaller particle size. However, at 90 $^{\circ}$C the particle size increased with pre-expansion pressure. This may be an indication that the role of coagulation becomes dominant at elevated extraction temperatures, above *ca.* 70 $^{\circ}$C, due to the higher solubility. While at the lower temperatures, with lower solute concentration, the roles of nucleation and condensation may be dominant. It may be concluded that the classical nucleation theory is not generally applicable to describing particle formation by RESS.

Condensation of carbon dioxide occurs shortly after the onset of precipitation of RDX. Due to the heterogeneous nature of carbon dioxide condensation on the surface of newly formed RDX nanoparticles, influence on the final particle size of RDX may be anticipated. Detailed analysis of the possible effects of solvent condensation is provided in Chapter 9.

6.7 Effect of Nozzle Diameter

Experiments were performed to determine the effect of the nozzle internal diameter (ID) on the particle size. Two nozzles with 100 and 150 µm ID and 250 µm length were investigated. The pre-expansion conditions were set to 90 °C and 155 bar. The post-expansion pressure was atmospheric. Particles were collected by sedimentation with dry ice encapsulation and recovered by sublimation of the dry ice. Sample SEM images of particles produced with the 100 and 150 µm ID nozzles are shown in Figures 6.9 and 6.11 respectively. The corresponding particle size distributions measured by SEM image analysis are shown in Figures 6.10 and 6.12
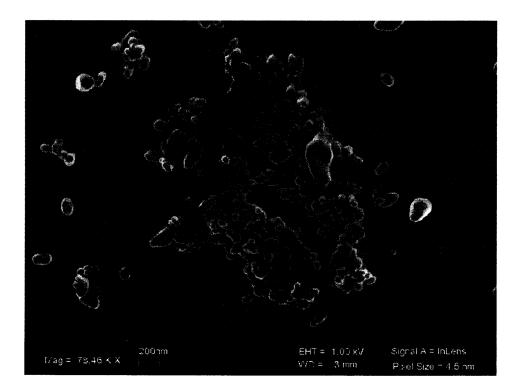
Figure 6.9 SEM image of RDX recrystallized by expansion from 155 bar and 90 °C to atmospheric pressure across a 100 µm ID orifice. Mean particle size is 115 ± 35 nm.
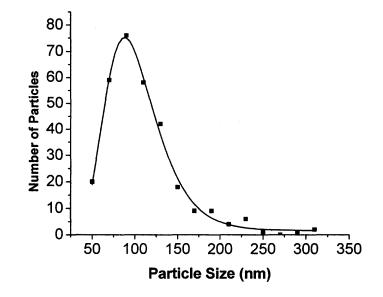
Figure 6.10 Particle size distribution of sample shown in Figure 6.9.
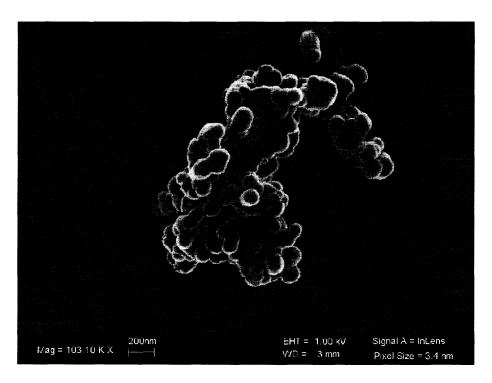
Figure 6.11 SEM image of RDX recrystallized by expansion from 155 bar and 90 °C to atmospheric pressure across a 150 μm ID orifice. Mean particle size is 140 ± 30 nm.
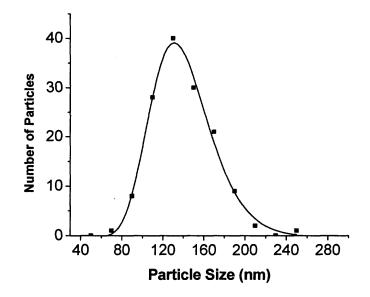
Figure 6.12 Particle size distribution of sample shown in Figure 6.11.

As can be seen in the preceding figures, increasing the nozzle internal diameter resulted in a larger particle size for the same set of expansion conditions. Increasing the nozzle ID for a constant nozzle length alters the expansion dynamics due to a change in the nozzle aspect ratio (L/D). As the nozzle ID increases the aspect ratio decreases. Consequently, a decrease in the pressure drop up to the nozzle exit and a higher fluid expansion rate are expected. In addition, a larger fraction of the overall pressure drop is expected to occur upstream of the nozzle entrance. This has the implication that the onset of precipitation will occur further upstream. An additional consequence of increasing the nozzle diameter is the lengthening of the supersonic free jet length downstream of the nozzle. A detailed analysis of fluid expansion across the nozzle is provided in Chapter 8. Such changes in the expansion dynamics may be responsible for the observed changes in the particle size. The significance of such effects is especially important with short nozzles as the pressure drop upstream of the nozzle is significant.

6.8 Physical Properties of Recrystallized RDX

A bulk sample of nanocrystalline RDX was prepared by continuous expansion across a 100 μm nozzle with extraction temperature set to 75 °C and pressure set to 280 bar. The solubility of RDX at these conditions is around 0.11 mg of RDX per gram of CO_2[2]. Several grams were generated for analysis. An SEM image and the particle size distribution of a sample taken from the final product are respectively illustrated in Figures 6.13 and 6.14.
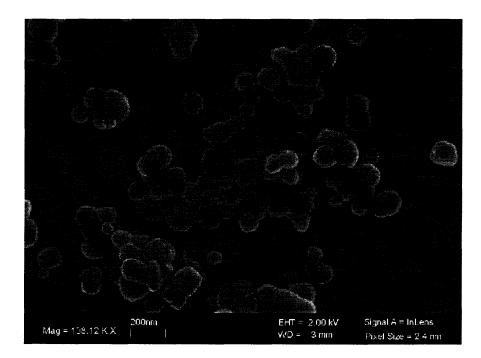
Figure 6.13 SEM image of RDX recrystallized by expansion from 280 bar and 75 °C to atmospheric pressure across a 100 μm ID orifice. Particle size is 130 ± 40 nm.
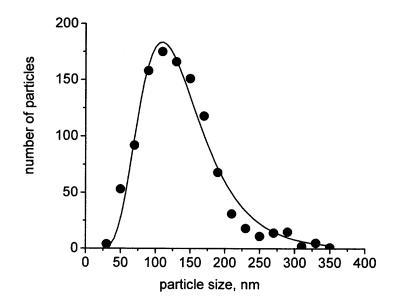
Figure 6.14 Particle size distribution of sample shown in Figure 6.13.

6.8.1 Thermal Analysis

Thermal analysis of the recrystallized RDX and conventional RDX samples was performed with a Perkin Elmer Sapphire differential scanning calorimeter (DSC). The samples were heated at a rate of 5 °C per minute over a temperature range from 140 to 280 °C. From this analysis the melting endotherm and the decomposition exotherm can be located. The thermal effects on the nanocrystalline and conventional size RDX as a result of heating are shown in Figures 6.15 and 6.16 respectively. The initial peak represents the endotherm corresponding to melting of the RDX sample. The second peak represents the decomposition exotherm of RDX. Characteristically of RDX the decomposition occurs shortly after melting and is the case in both samples.
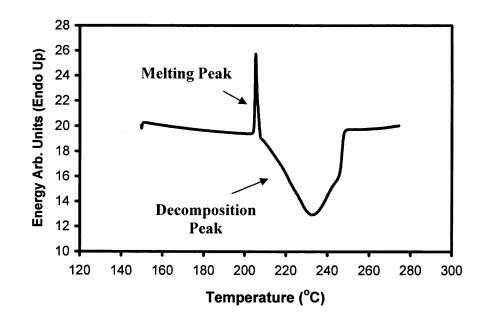
Figure 6.15 Thermal behavior of nanocrystalline RDX determined by DSC analysis.
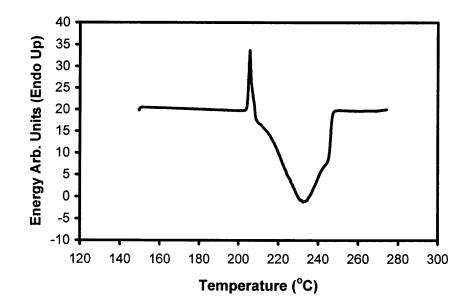
Figure 6.16 Thermal behavior of pure RDX with conventional grain size determined by DSC analysis.

The onset of melting in both conventional and nanocrystalline RDX samples was found to be nearly identical. The melting point of the conventional RDX was 204.3 °C. The melting point of the recrystallized RDX was 204.5 °C. These values are in agreement with the accepted melting point value of 204 °C[1]. It can be concluded that the RDX crystal size does not influence the melting point for sizes larger than around 100 nm.

6.8.2 Powder X-Ray Diffraction Analysis

Powder X-ray diffraction was used to determine whether the particles are crystalline or amorphous. The X-ray diffraction spectra for the recrystallized and the precursor RDX are shown in Figure 6.17. Peak intensity (arbitrary units) is plotted as a function of the diffraction angle (2θ). From the narrow peak width it can be concluded the nanoparticles of RDX have a crystalline structure. In the diffraction spectrum of the precursor RDX several peaks appear that do not appear in the spectrum of the recrystallized RDX. This is likely due to the presence of impurities in the precursor RDX which are insoluble or weakly soluble in supercritical carbon dioxide and thus were not extracted from precursor. The largest known impurity in commercial grade RDX is HMX. Around 10 % of HMX is expected to be present.
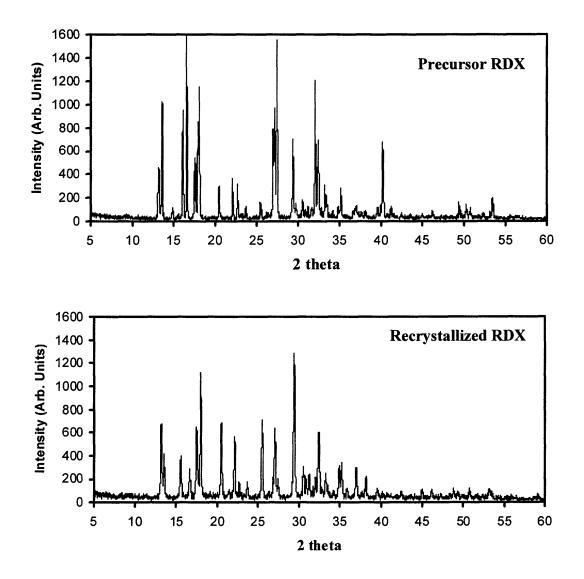
Figure 6.17 Powder X-ray diffraction spectra for precursor RDX (top) and recrystallized RDX (bottom).

6.8.3 HPLC Analysis

The purity of the precursor and the recrystallized RDX was determined by high performance liquid chromatography (HPLC) analysis. The precursor RDX was found to contain 12% HMX by weight. This is expected as HMX is a major byproduct in the Bachman process used in the synthesis of RDX used as precursor in this work[89]. The HMX content in the recrystallized RDX was found to be less than 1%. This result reveals that the solubility of RDX is significantly higher in supercritical CO_2 than HMX. This is in agreement with published supercritical carbon dioxide extraction data of RDX and HMX [90, 91].

6.8.4 Examination of Bulk Density

The tap density of bulk nanocrystalline RDX is substantially lower than that of class-5 RDX, a conventional form of RDX with a *ca.* 10-20 μm mean crystal size. The bulk size of 1 gram samples of nanocrystalline RDX and class-5 RDX are shown in Figure 6.18. A substantially lower bulk density of the nanocrystalline RDX is evident. The low bulk density is a result of the increased tendency of small particles, especially at the nano-scale, to agglomerate. Interaction between particles due to van der Waals forces is enhanced by the large surface area.
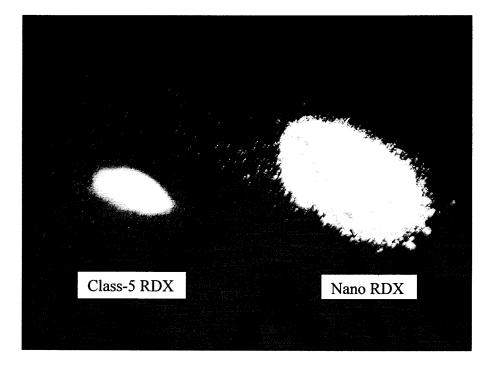
Figure 6.18 Photograph of 1 gram samples of class-5 and nanocrystalline RDX.

6.9 Summary

It was demonstrated that production of nanocrystalline RDX was feasible by rapid expansion of supercritical solutions with carbon dioxide as the solvent with expansion to atmospheric pressure. The effect of the pre-expansion temperature and pressure was investigated in the pressure range from 100 to 350 bar and at temperatures 70, 80, and 90°C. The particle size was found to depend on both the pre-expansion temperature and pressure and ranged from 100 to 300 nm. Near spherical particle morphology was observed in the experiments.

An efficient particle collection method by heterogeneous condensation of solid carbon dioxide followed by sedimentation was demonstrated. RDX recovery was achieved by sublimation of carbon dioxide at atmospheric pressure. The collection efficiency was estimated to approach 100 %.

The physical properties of the recrystallized RDX were assessed. Crystallinity of the RDX nanoparticles was confirmed by powder X-ray diffraction. The melting point of the recrystallized material matched the melting point of conventional size RDX.

The RESS process was demonstrated to be an effective way of producing nanocrystalline RDX with high purity, near spherical particle morphology, and physical properties matching those of conventional RDX.

CHAPTER 7

SCALE-UP OF THE RESS PROCESS

Due to the high demand of carbon dioxide during the recrystallization of RDX by the RESS process, around 5 kg CO_2 per 1 g of RDX, bulk production of nanocrystalline RDX will require the recycling of carbon dioxide. Recycling entails liquefaction of the expanded gas in order to be fed back to the pump in the liquid state. The liquid feed to the pump should be at a temperature below the saturation temperature in order to minimize vaporization during piston filling which can result in a drastic drop in pumping efficiency. For piston pumps the desired temperature is around 15-20 °C below the saturation temperature.

Liquefaction may be accomplished in two ways, cooling the expanded gas until liquid is formed or by compression of the gas followed by cooling. As can be seen in the phase diagram of carbon dioxide (Figure 2.1), at pressures below 5.2 bar or the triple point pressure, a liquid phase does not exist. In such case in order to liquefy the gas phase carbon dioxide compression to a pressure at least above the triple point pressure is necessary. Above the triple point pressure carbon dioxide can be liquefied solely by cooling, however, at low pressures very cold temperatures are required for liquefaction. For example, liquefaction of carbon dioxide gas at 10 bar will require cooling the gas to around -50 °C. Such low temperatures are difficult to achieve due to the requirement of specialized equipment and components including chillers, heat exchangers as well as seals. Temperatures in the range from 0-10 °C are fairly easily attainable with standard equipment and should not compromise the integrity of polymeric seals and other standard

104

components. At 0 $^{\circ}$C pump feed temperature the required pressure is around 50 bar. Thus it is evident that compression may be necessary at expansion pressures below 50 bar. It can also be appreciated how expansion to pressures above 50 bar could simplify the processing requirements by eliminated the need for compression.

7.1 Experimental Set-Up

An experimental set-up, illustrated in Figure 7.1, was built with the capability to recycle carbon dioxide by both cooling and compression. The set-up is similar to the one described in Chapter 6, with an added capability of carbon dioxide recycling. It consists of a dual piston liquid pump rated for up to 350 bar discharge pressure and around 2 l/min flow rate. The pressurized carbon dioxide is pre-heated to desired extraction temperature upstream of the extraction vessel. The saturated solution is expanded across a nozzle into the expansion vessel. One liter stainless steel expansion vessels were used with a pressure rating of around 1000 psi. The expansion vessels were heated with heating tape. Depending on the expansion pressure downstream of the nozzle, the carbon dioxide is recycled either by cooling alone or by compression followed by cooling in a heat exchanger. A two stage diaphragm compressor by PPI Inc. was used for carbon dioxide compression. Two expansion chambers allowed processing at two sets of expansion conditions allowing for direct comparison of process parameters including the post-expansion pressure and temperature as well as the nozzle diameter.
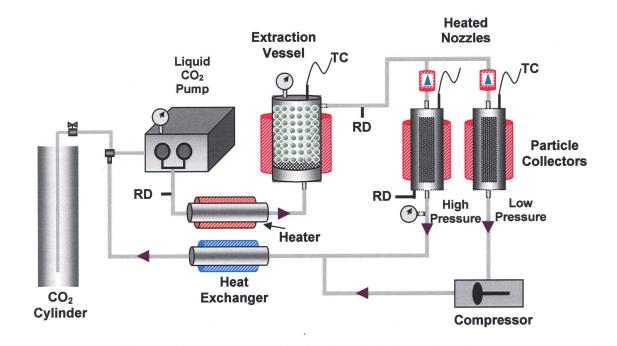
Figure 7.1 Schematic of experimental RESS set-up with carbon dioxide recycling.

Cooling was achieved with a tube in tube heat exchanger where the high pressure tubing containing the carbon dioxide was cooled by an external flow of an ethylene glycol/water coolant mixture. The coolant was chilled with an FTS Systems Maxi Cool chiller/circulator. The coolant and carbon dioxide flows were set-up in a counter current flow arrangement for efficient cooling.

When operating the RESS process with near atmospheric post-expansion pressure the gas was compressed with the two stage diaphragm compressor. Typically the carbon dioxide was compressed to the cylinder pressure, around 55-65 bar, depending on the room temperature. This was necessary as the cylinder volume was connected throughout the operation in order to maintain a stable pressure in the low pressure zones. In addition, this ensured that no overpressure would occur in the low pressure collection vessels and tubing. Substantial heating of the carbon dioxide occurs during compression. The compressed carbon dioxide was cooled to around 0 - 5 °C and fed back to the pump.

The set-up was also operated by setting the post-expansion pressure in the range from 55 – 65 bar. In this case no compression was required and the expanded gas bypassed the compressor and was fed directly to the chiller before entering the pump. Only cooling was necessary to liquefy the carbon dioxide. Without compression the process complexity and energy requirements are greatly reduced. However, the effect of increasing the post-expansion pressure on the product particle size must had to be investigated. An important consequence of operating at elevated post-expansion pressures is that condensation of carbon dioxide during expansion will not result in the formation of dry ice, but rather will condense as liquid. Consequently, the particle collection approach outlined in Section 6.3, useful with expansion to near atmospheric pressures, will not be applicable. Instead, filtration must was employed.

Operation at both low and high post-expansion pressures the collection vessels are heated in order to avoid the build-up of solid carbon dioxide during low expansion pressure operation, or liquid carbon dioxide build-up during operation at elevated post-expansion pressures.

7.2 Effect of Post-Expansion Pressure

The effect of elevating the post-expansion pressure on the particle size and morphology was investigated for discharge pressures ranging from around 1 to 65 bar. The dependence of the mean particle size on the discharge pressure for a set of pre-expansion conditions: 85 °C and 280 bar and 85 °C and 350 bar is shown in Figure 7.2. A 100 μm ID nozzle was used in these experiments.
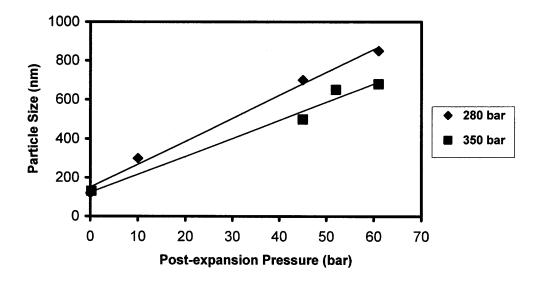
Figure 7.2 Effect of post-expansion pressure on the mean particle size at 280 and 350 bar pre-expansion pressures.

As can be seen in Figure 7.2, the particle size increases with post-expansion pressure. However, for the pressure range investigated, at a given post expansion pressure the particle size can be reduced by increasing the pre-expansion pressure.

An SEM image of RDX recrystallized by expansion from pre-expansion conditions at 280 bar and 85 °C to 44 bar discharge pressure is shown in Figure 7.3. Particle size ranged from around 300 nm to several microns. Large irregular particles can be seen. For comparison an SEM image of RDX produced by expansion from pre-expansion conditions at 350 bar and 85 °C to 44 bar discharge pressure is shown in Figure 7.4. In this case smaller particles were formed with sizes ranging from around 200 nm to a 1 micron. It can be seen that increasing the discharge pressure results in a larger particle size. Substantially larger particles were formed at the lower pre-expansion pressure. Irregular particle shape can also be seen especially with the larger particles.
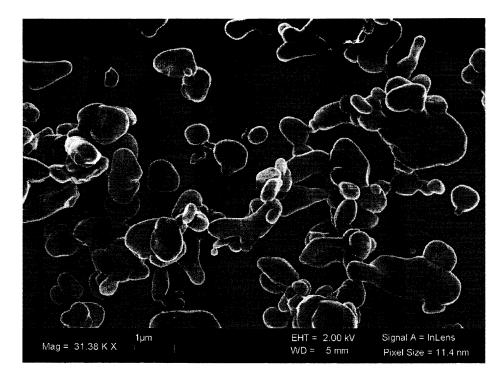
Figure 7.3 SEM image of RDX recrystallized by expansion from 280 to 44 bar.
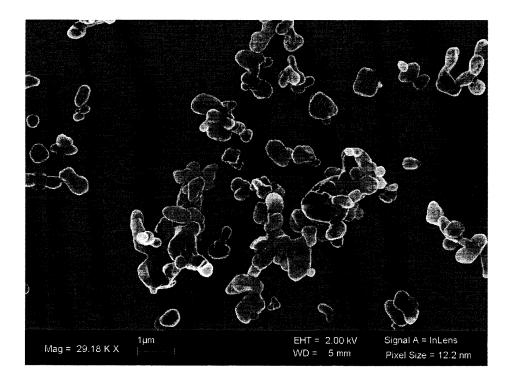
Figure 7.4 SEM image of RDX recrystallized by expansion from 350 to 44 bar.

The larger particle size is an indication that the growth mechanisms downstream of the nozzle are different compared with expansion to near atmospheric pressures. As will be shown in Chapter 8, due to the chocked flow regime, the flow properties as well as the particle size distribution at the nozzle exit are expected to be identical. The differences observed in the product generated by expansion to elevated pressures compared to product generated by expansion to near atmospheric pressures is solely due to the growth occurring downstream of the nozzle. An important difference is the heterogeneous condensation of liquid carbon dioxide rather than solid. The effect of such condensation on the particle size and morphology are considered in detail in Chapter 9.

7.3 Powder Characterization by BET Surface Area Analysis

BET specific surface area analysis is a convenient tool for bulk powder characterization. The analysis measures the specific surface area of a bulk powder with a several mg sample size. An effective mean particle diameter, assuming uniform spherical particles, can be calculated from the specific surface area (SSA) by the following derived expression:

$$D = \frac{6}{SSA \cdot \rho} \tag{7.1}$$

Here D is the mean particle diameter and ρ is the density of the solid. BET surface area analysis alone provides no information regarding the particle shape and particle size distribution and microscopy is needed to better characterize the sample material. However, when the particle morphology is known for select process conditions, surface area analysis is a convenient way to quantitatively compare different samples with a

sample size much more representative of the bulk than the sample size in SEM image analysis.

Surface area analysis was performed on powder samples generated by RESS. The analysis was performed on a Beckman Coulter SA 3100 surface area analyzer with nitrogen as adsorbent. Samples were prepared for analysis by vacuum outgasing at 60°C for 3 hours. Typical sample size was on the order of 10 mg.

The measured SSA for several samples of recrystallized RDX is plotted vs. the mean particle diameter as determined from SEM image analysis in Figure 7.5. The dashed line represents the dependence of the SSA on the particle size based on Equation 7.1. A reasonable agreement between the fitted and calculated curves can be seen at low SSA values. At higher SSA values a larger discrepancy exists. Such discrepancy is not surprising for several reasons. The calculated values were obtained with the assumption of spherical particle shape as well as a uniform particle size. Particle size estimation based on SEM image analysis is limited to two dimensions, thus the size distribution is based on the two dimensional analysis. Another source of error which may explain the apparent discrepancy is the number average based mean particle size used in the comparison. Due to the non-uniform particle size, the use of a weight or volume averaged mean particle size would be more appropriate for comparison with the specific surface area. The mean particle size based on the number average value is likely lower than that based on the weight or volume average value. A closer correlation would thus be expected between a volume or weight averaged particle size and the specific surface area.

Overall the specific surface area may be a better quantitative metric than the mean particle size determined from SEM image analysis. BET surface area analysis is a

valuable tool in comparing samples produced at different conditions or to monitor the product uniformity of a production process. In can be concluded that in order to obtain a comprehensive and representative characterization of a powder sample both SEM and surface area analysis should be used in conjunction.
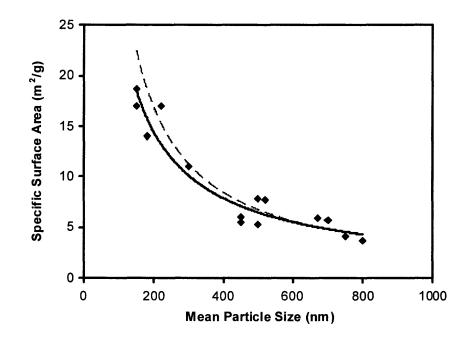
Figure 7.5 Correlation of measured specific surface area with the mean particle size determined from SEM analysis. Dashed line represents the calculated values based on Equation 7.1.

7.4 Effect of Pre-Expansion Pressure on the Particle Size

The effect of the pre-expansion pressure on the particle size was investigated. Data shown in Figure 7.6 represent the specific surface area of RDX samples recrystallized by expansion across a 150 μm nozzle with 85 °C extraction temperature. Two sets of data are presented. Expansion to downstream pressures set at 2 bar and 50 bar with the pre-expansion pressures ranging from 300 to 350 bar.
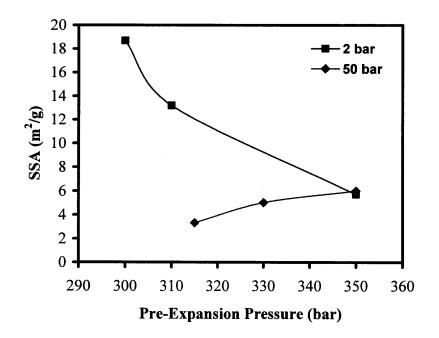
Figure 7.6 Effect of the pre-expansion pressure on the specific surface area of RDX produced by expansion to 2 and 50 bar discharge pressures.

It can be seen in Figure 7.6 that the RDX specific surface area decreases as the pre-expansion pressure increases in the range from 300 to 350 bar with expansion to 2 bar. The opposite trend is true for expansion to 50 bar. In this case the specific surface area of RDX decreases as the pre-expansion pressure increases from 315 to 350 bar.

An interesting result is revealed at the 350 bar pre-expansion pressure. There is essentially no effect of the discharge pressure on the specific surface area. SEM images of the two samples produced by expansion from 85 °C and 350 bar to 2 and 50 bar discharge pressures are shown in Figures 7.7 and 7.8 respectively. The images are scaled to equal magnification. Examination of the SEM images reveals that crystals of RDX produced at the higher discharge pressure have a wider size distribution with size ranging

from around 300 nm to around 5 μm. The larger particles appear to have a very irregular surface morphology.
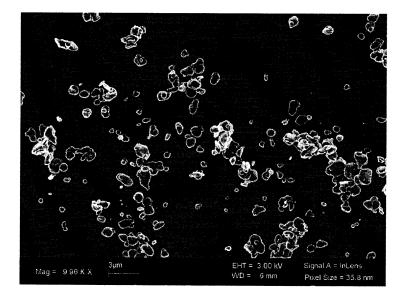
Figure 7.7 SEM image of RDX recrystallized by expansion from 350 to 2 bar.
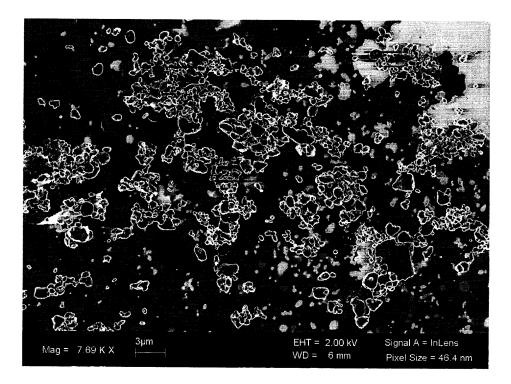

Figure 7.8 SEM image of RDX recrystallized by expansion from 350 to 50 bar.

At the lower discharge pressure RDX crystals appear to be nearly spherical and the crystal size ranges from around 300 nm to around 1 μm. The difference in the size distribution and the surface morphology are likely due to the drastically different expansion environments at the two discharge pressures. The condensation of liquid phase carbon dioxide at the higher discharge pressure coupled with a greatly reduced length of the free jet downstream of the nozzle are likely responsible for the difference in the particle size. The variation in the particle size and morphology is likely due to coagulation mechanisms downstream of the nozzle exit. The particle size distribution at the nozzle exit is expected to be identical. The possible effects of the discharge pressure on the particle size and morphology are discussed in detail in Chapters 8 and 9.

7.5 Processing with Alternative Solvents

Due to the low solubility of RDX in the non-polar carbon dioxide, substitution of carbon dioxide by polar solvents including CHF_3 and carbon dioxide modified with acetone was investigated to determine whether higher throughput of RDX is feasible.

7.5.1 Recrystallization with CHF_3

An experiment was performed to see the effect of substituting carbon dioxide with a polar supercritical solvent on the throughput and morphology of recrystallized RDX. CHF_3 was chosen due to its mild critical conditions[40]. The critical temperature is 298.89 K and the critical pressure is 48.36 bar. CHF_3 is polar with a dipole moment of 1.649 Debye. 99.0 % purity CHF_3 (Halocarbon 23) was obtained from Praxair.

The extractor temperature and pressure were set to 85 °C and 280 bar respectively. The supercritical solution was expanded to nearly atmospheric pressure across a 100 μm ID orifice. An SEM image of the recrystallized RDX is shown in Figure 7.9.
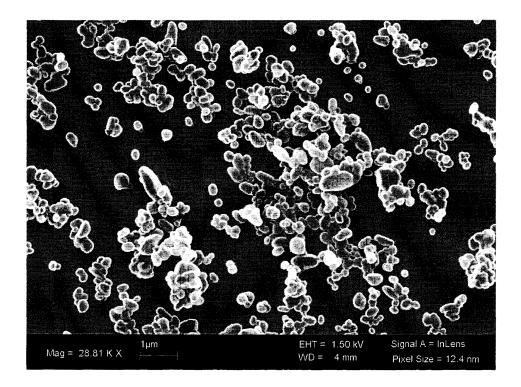
Figure 7.9 SEM image of RDX recrystallized by RESS from CHF_3.

Analysis of Figure 7.9 revealed that the average particle size was around 180 nm. The specific surface area of this sample was 13.9 m^2/g. The crystals appear to be nearly spherical with a relatively narrow size distribution. The particle size and morphology of RDX recrystallized with CHF_3 is similar to RDX recrystallized from carbon dioxide at the same processing conditions. The throughput of RDX with CHF_3 was also similar to the throughput with carbon dioxide indicating a similar solubility. It can be concluded

that CHF$_3$ offers no advantage over carbon dioxide in the processing of RDX. Its use is less desirable due to the high cost and environmental concerns.

7.5.2 Recrystallization with Acetone-Modified CO$_2$

Recrystallization of RDX was investigated with acetone-modified carbon dioxide as solvent. The acetone concentration was varied from 0.2 to 1 mole %. A 150 μm ID nozzle was used in the experiments. The pre-expansion conditions were set to 90 °C and 350 bar. In order avoid the condensation of acetone in the expansion chamber the pressure of the expansion chamber was set to 50 bar and the discharge temperature was set to 50 °C. Condensation of acetone would lead to re-dissolution of the product and consequently alteration of the particle size and morphology.

An SEM image of RDX recrystallized from carbon dioxide modified with 1 mole % acetone is shown in Figure 7.10. A wide size distribution is evident, with crystal size ranging from around 500 nm to 3 μm. The bulk of RDX was recrystallized in the form of large rectangular shaped crystals. The crystal morphology and size distribution are notably different from RDX produced at similar conditions with pure carbon dioxide shown in Figure 7.8. A lower specific surface area was measured for the sample recrystallized with acetone, 3.9 m^2/g, compared to 6 m^2/g for the sample recrystallized from pure carbon dioxide.

A *ca.*30 % increase in throughput was observed with 1 mole % acetone-modified carbon dioxide, indicating a higher solubility. Such moderate enhancement in solubility is consistent with the findings of Niehaus et al[56].
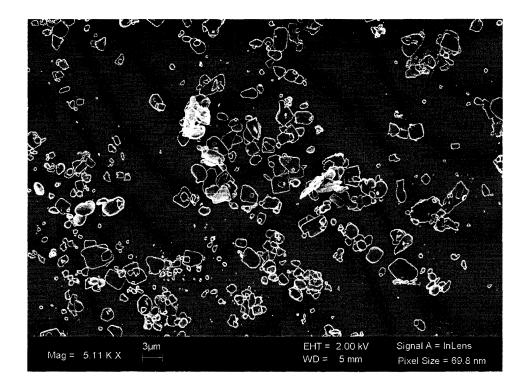
Figure 7.10 SEM image of RDX recrystallized by RESS from carbon dioxide modified with 1 mole % acetone.

Based on the rationale outlined in Chapter 9 condensation of the co-solvent along the expanding jet is expected to occur earlier than the condensation of liquid carbon dioxide. Consequently, partial or complete dissolution of RDX in the acetone condensate is likely. In the warmer expansion chamber, evaporation of the acetone droplets likely leads to precipitation of RDX with an altered particle size and morphology.

Increasing the concentration of acetone resulted in a decrease of the specific surface area of RDX as is shown in Figure 7.11.
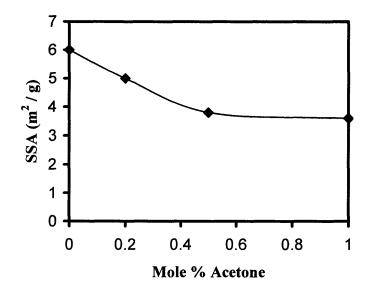
Figure 7.11 Effect of acetone mole % on the surface area of RDX.

The throughput of RDX with acetone-modified carbon dioxide at the highest acetone concentration, 1 mole %, was modestly higher, however, due to the negative effect on the RDX particle size and morphology as well as the requirement of higher expansion vessel temperature it can be concluded that carbon dioxide modification by acetone is not desirable.

7.6 Effect of the Nozzle Diameter

Higher production rates with the RESS process can be achieved by either increasing the number of nozzles or by using nozzles with a larger internal diameter. The latter would be preferred since a lesser quantity of nozzles will require fewer connections, collection vessels, and other components. The influence of the nozzle ID on the particle size and morphology was examined.

In this study short orifice nozzles with internal diameter values ranging from 100 to 250 micron were investigated. Table 7.1 lists the specific surface area of recrystallized RDX in four sets of experiments each with identical process conditions but differing nozzle internal diameter.

Table 7.1 Effect of Nozzle Internal Diameter on the Specific Surface Area of Recrystallized RDX

	Extraction Pressure (bar)	Extraction Temperature (K)	Post-Expansion Pressure (bar)	Nozzle Diameter (μm)	Specific Surface Area (m^2/g)
Set 1	350	360	1	100	17.2
	350	360	1	150	10.4
Set 2	310	360	2	150	13.2
	310	360	2	200	6.8
Set 3	350	358	60	150	5.5
	350	358	60	200	4.8
Set 4	320	358	60	150	5.9
	320	358	60	250	4.6

For all four sets of experimental conditions, the specific surface area of the recrystallized RDX samples increased with decreasing nozzle internal diameter. The effect appears to be more pronounced with expansion to low pressures.

7.7 Solvent Saturation during Extraction

Bulk production of nanocrystalline RDX was typically performed by processing at throughput rates as high as 6 grams RDX per hour. This corresponds to a maximum carbon dioxide flow rate around 30 kg/hour. Such high flow rates were achieved by using

two nozzles simultaneously. Although a single nozzle with a larger internal diameter could in principle have been used, heating of the 1 liter expansion vessels became inadequate. Larger vessels with a higher surface area would be required with higher ID nozzles.

At the higher flow rates ensuring that the supercritical solution is adequately saturated prior to expansion is necessary as the particle size may depend on the solute concentration. Also, processing at undersaturated conditions will lead to reduction in the throughput. Experiments at all flow rates were performed using the 1 liter extraction vessel. At high flow rates the glass beads were removed. Instead an impeller coupled through the top lid of the vessel was used. The precursor RDX powder was loaded directly into the vessel.

In order to validate that sufficient saturation was achieved at all flow rates the throughput of RDX is plotted versus the flow rate of supercritical carbon dioxide in Figure 7.12. The data represent experiments with extraction at 350 bar and 85 $^{\circ}$C. A linear correlation of the RDX throughput on the mass flow rate of carbon dioxide can be seen over the entire range of flow rates investigated. The linear dependence indicates that similar saturation levels were achieved for the entire range of flow rates.

At the highest flow rate the fluid residence time inside the extraction vessel is around 1.5 minutes. Near complete saturation of the fluid at such residence time is not surprising due to the characteristically high diffusivity of the solute in supercritical carbon dioxide, which can be several orders of magnitude higher than the diffusivity in conventional liquid solvents.
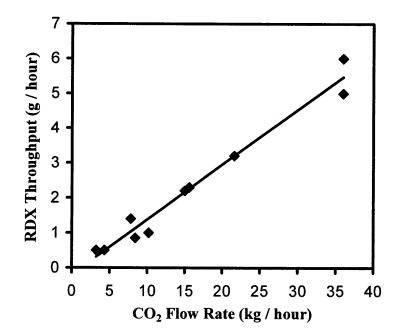
Figure 7.12 Dependence of RDX throughput on the flow rate of carbon dioxide for extraction at 350 bar and 85 °C.

7.8 Conclusions

Transitioning the RESS process from lab scale to bulk production requires engineering analysis which takes into account both the desired product characteristics as well as processing complexity. Selection of nozzle size, process conditions including the pre-expansion pressure and temperature as well as post-expansion pressure all affect the product characteristics.

Economical processing by RESS will require recycling of the solvent. The method of recycling depends on the discharge pressure. At low discharge pressures compression followed by cooling is required to liquefy the solvent. At high discharge pressure compression can be eliminated and liquefaction can be achieved solely by cooling. Although expansion to higher pressure may result in substantially lower processing costs and complexity, the effect on the particle size and morphology due to

expansion to a higher discharge pressure must be taken into account. The smallest particle size was achieved by expansion to near atmospheric pressure. In addition the particle morphology and size distribution appear to be improved at the low discharge pressure.

Pure carbon dioxide appears to be the most suitable solvent for recrystallization of RDX. Replacement of carbon dioxide by CHF_3 resulted in a similar particle size and morphology but no significant enhancement of throughput was observed. Modification of carbon dioxide with up to 1 mole % acetone had a moderate enhancement of the throughput of RDX (ca. 30 %) but also resulted in an undesired particle size increase.

It was observed that increasing the nozzle diameter generally resulted in an increased particle size. It can be concluded the use of multiple smaller ID nozzles may be preferred to a single larger nozzle if minimum particle size is required.

CHAPTER 8

DYNAMICS AND THERMODYNAMICS OF

SUPERCRITICAL CO_2 EXPANSION

8.1 Introduction

Expansion of compressed gases across a flow restriction is a practical way of achieving a large reduction in pressure on a very short time scale. Typical flow restrictors include nozzles which range from short orifices to long capillaries. The nozzle dimensions, aspect ratio (L/D), and nozzle geometry can influence the expansion rate. The inlet to a nozzle is usually tapered since substantially higher flow rates can be achieved as the entrance losses are minimized.

The flow efficiency of a nozzle is often described in terms of the flow coefficient, C. The coefficient value ranges from 0 to 1 with 1 being the ideal case with no losses. Due to flow disturbances at the nozzle inlet and outlet as well as internal friction a value of the flow coefficient below 1 is always expected. High quality nozzles have a flow coefficient value above 0.9. For nozzles with untapered, flat inlets the coefficient may be as low as 0.6. For a given type of restriction, the flow rate and thus the expansion rate can be precisely controlled by varying the channel length of the restriction.

Short nozzles with a low aspect ratio (length/diameter) are preferred to higher aspect ratio nozzles such as capillaries for high throughput processing by rapid expansion of supercritical solutions (RESS). Long capillary type nozzles although commonly used for experimental investigations may not be suitable for continuous RESS operation due to

slow expansion rates which can affect the particle size as well as being more susceptible to clogging. Short nozzles on the other hand are less likely to clog and provide higher expansion rates. With short nozzles the expansion is nearly adiabatic due to low fluid residence time within the nozzle. For long nozzles heat exchange with the surroundings becomes significant due to the longer residence time and must be accounted for and controlled to achieve the desired expansion conditions.

Choked flow is typically achieved at the process conditions where the pre-expansion to downstream pressure ratio exceeds 2. When this is the case the flow is critical, meaning that the velocity at the nozzle outlet is sonic or the Mach number is equal to 1. In a chocked flow regime decreasing the downstream pressure will not affect the mass flow rate. Only increasing the pre-expansion pressure can be used to increase the mass flow rate.

Expansion of a compressible fluid across a nozzle begins up-stream of the nozzle entrance and continues well downstream until the pressure is in equilibrium with that of the surroundings. As will be shown in the subsequent sections, a substantial pressure reduction is attained upstream from the nozzle due to the converging flow. Further pressure drop occurs within the nozzle. The fastest pressure drop occurs during supersonic free jet expansion downstream of the nozzle. At the nozzle inlet as well as inside the nozzle the flow is subsonic, immediately downstream of the nozzle exit the unconfined expansion occurs at supersonic velocities.

In order to optimize the design of the RESS process a key requirement is the thorough understanding of the flow properties. Using one-dimensional flow modeling approach for compressible fluids, the temperature and pressure profiles in the subsonic

expansion stages have been calculated. Such one-dimensional models have been reported to reasonably predict the fluid properties along the subsonic expansion path[52, 70, 71]. The impact of the temperature and pressure profiles on the solute precipitation is examined.

8.2 Nozzle Flow Calibration

The mass flow rate of supercritical carbon dioxide through a nozzle was measured as a function of the pre-expansion pressure at 354 K pre-expansion temperature and atmospheric pressure downstream of the nozzle. Measurements were performed at several pre-expansion pressures ranging from 100 to 350 bar. The nozzle used in the experiments was a laser drilled sapphire nozzle with a 150 μm internal diameter a 250 μm duct length. The inlet to the nozzle is tapered, while the outlet is flat. A flow calibration curve is shown in Figure 8.1. A linear dependence of the flow rate on the pre-expansion pressure was observed over the pressure range investigated. The experimental data was fitted with a linear function shown the figure.
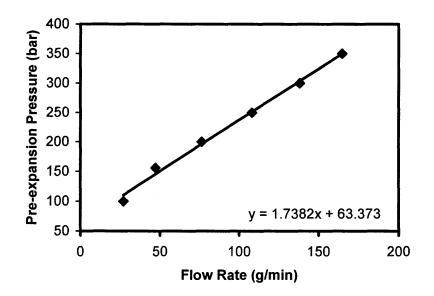
Figure 8.1 Mass flow rate of carbon dioxide through a sapphire nozzle with 150 micron internal diameter and 250 micron length as a function of pre-expansion pressure.

8.3 Flow Calculations

A steady state one-dimensional compressible flow model was used to calculate the dynamic and thermodynamic properties of expanding carbon dioxide. The temperature, pressure, and velocity along the expansion path were calculated for the expansion of carbon dioxide across a short nozzle described in Section 8.2. Several assumptions have been made in the calculations. The velocity profile of the expanding jet was assumed to be flat implying that the velocity only varies along the expansion axis. The fluid was assumed to be pure carbon dioxide. This is a reasonable assumption as the concentration of the solute RDX is less than 100 ppm and thus should not have much effect on the fluid properties. A short orifice nozzle with a low aspect ratio was considered in this model. Such short nozzles may be treated as adiabatic due to the short residence time. Flow properties were calculated at the subsonic expansion stages at the nozzle inlet and inside

the nozzle. A diagram of the nozzle and the key expansion stages of a compressible fluid are illustrated in Figure 8.2.
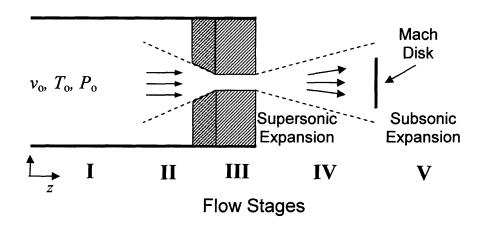
Figure 8.2 Compressible fluid expansion across a nozzle.

In Figure 8.2, stage I is the pre-expansion stage where the velocity, pressure, and temperature may be considered constant along the length of the duct. The velocity along this stage is on the order of 1 m/s. Stage II represents the nozzle inlet region where acceleration occurs due to converging flow. The flow in this stage is considered to be inviscid and adiabatic, and therefore the expansion is isentropic. Stage III represents the flow inside the cylindrical nozzle with a constant cross section. At this stage wall friction is responsible for the fluid expansion. This stage cannot be considered isentropic due to conversion of fluid momentum into heat resulting from viscous dissipation. Since the nozzles being considered has a low aspect ratio, 1.67, the heat flux across the nozzle surface is considered to be negligible.

At stage IV, unconfined free-jet expansion of the fluid occurs. Here the unconfined jet expands at supersonic velocities with Mach number exceeding 1. The flow in the supersonic free-jet may be considered adiabatic and isentropic. At the end of the

free jet the transition from supersonic to subsonic velocities results in the formation of shock waves. The peak pressure at the shocks is expected to be several bar above the downstream pressure. The shock wave normal to the flow is called the Mach disk. Its position is stationary during steady flow. Around 25% of the fluid is estimated to flow through the Mach disk, while the remaining fluid decelerates to subsonic velocity by barrel shock transition[70]. A spike in the temperature and pressure occurs at the shock waves. Downstream of the Mach disk the subsonic jet decelerates by entrainment of gas from the surroundings.

Calculation of the flow properties in the supersonic jet would require sophisticated multi-dimensional modeling and was not undertaken in this work. However, estimates of the fluid properties in the jet based on modeling calculations available in the literature are adopted in order to complete the description of the expansion process.

8.3.1 Governing Equations

The one-dimensional compressible flow model consists of the governing differential Equations (8.1)[92]. The expressions of continuity (a), conservation of momentum (b) and conservation energy (c) make up the system of equations required to calculate the flow properties:

$$\frac{d\rho}{\rho} + \frac{dv}{v} + \frac{dA}{A} = 0 \qquad (8.1\text{-a})$$

$$\frac{dP}{\rho} + vdv + gdh = dW - dE_v \qquad (8.1\text{-b})$$

$$dH + vdv = dQ \qquad (8.1\text{-c})$$

where ρ is fluid density, v is the velocity along the expansion axis, A is the cross sectional area normal to the flow, P is the pressure, g is the gravitational acceleration, h is the height, W is the shaft work, E_v is the viscous loss of mechanical energy and Q is the heat flux.

The viscous dissipation term, E_v, accounts for the mechanical energy losses due to friction inside the nozzle. This term accounts for the increase of the fluid entropy. Viscous dissipation can be described in terms of the Fanning friction factor f [92]:

$$E_v = \frac{2 f \rho v^2}{D} \tag{8.2}$$

For the case of adiabatic expansion, which is relevant for stages II and III of the expansion across a nozzle, Equations 8.1 can be transformed into differential equations of the variation of density, velocity, and temperature along the expansion axis z, resulting in [70]:

$$\frac{d\rho}{dz} = -\frac{\rho}{D(z)(M^{-2} - 1)} \left[\left(1 + \frac{1}{C_{v,m} \rho_m} \left(\frac{\partial P}{\partial T} \right)_\rho \right) 2f - 2 \frac{dA}{dz} \right] \tag{8.3}$$

$$\frac{dv}{dz} = v \left(-\frac{1}{\rho} \left(\frac{\partial \rho}{\partial z} \right) - \frac{2}{D(z)} \frac{dA}{dz} \right) \tag{8.4}$$

$$\frac{dT}{dz} = \rho \, C_v \left(\frac{2\rho v^2 f}{D(z)} + T \left(\frac{\partial P}{\partial T} \right)_\rho \frac{1}{\rho} \left(\frac{\partial \rho}{\partial z} \right) \right) \tag{8.5}$$

where C_v is the constant volume heat capacity, $D(z)$ is the position dependent diameter of the flow cross section, T is the temperature and M is the Mach number. The Mach number is a dimensionless ratio of the fluid velocity to the local speed of sound, c.

$$M = \frac{v}{c} \tag{8.6}$$

The speed of sound is defined as:

$$c^2 \equiv \left(\frac{\partial P}{\partial \rho}\right)_S = \gamma \left(\frac{\partial P}{\partial \rho}\right)_T \tag{8.7}$$

where S is the entropy, γ is the ratio of the constant pressure heat capacity to the constant volume heat capacity: C_p / C_v.

Expression 8.3 is Mach number explicit. A singularity occurs at the sonic velocity where the Mach number equals to unity. This has an important implication that fluid acceleration beyond sonic velocity is impossible in a converging flow.

A suitable equation of state is necessary to solve Equations 8.3-8.5. A commonly employed equation of state for compressed carbon dioxide property calculations is the Peng-Robinson cubic equation of state[47]:

$$P = \frac{RT}{V-b} - \frac{a(T)}{V^2 + 2bV - b^2} \tag{8.8}$$

$$a(T) = 0.45724 \frac{(RT_c)^2}{P_c}\left(1 + k\left(1 - \left(\frac{T}{T_c}\right)^{1/2}\right)\right)^2$$

$$k = 0.37464 + 1.54226\omega - 0.26992\omega^2$$

$$\omega = \text{acentric factor}$$

$$b = 0.07780 \frac{RT_c}{P_c}$$

The inaccuracy of the Peng-Robinson equation of state is significant at the expansion conditions relevant to this work. In order to improve the accuracy of the

calculations, a 27-parameter empirical equation of state for carbon dioxide shown below was used in the calculations[93].

$$\frac{P}{\rho \, R \, T} = 1 + b_2\rho' + b_3\rho'^2 + b_4\rho'^3 + b_5\rho'^4 + b_6\rho'^5 + b_7\rho'^2 \exp(-c_{21}\rho'^2) + b_8\rho'^4 \exp(-c_{21}\rho'^2)$$

$$+ c_{22}\rho' \exp(-c_{27}(\Delta T)^2) + c_{23}\frac{\Delta\rho}{\rho'} \exp(-c_{25}(\Delta\rho)^2 - c_{27}(\Delta T)^2) \tag{8.9}$$

$$+ c_{24}\frac{\Delta\rho}{\rho'} \exp(-c_{26}(\Delta\rho)^2 - c_{27}(\Delta T)^2)$$

where T is the temperature in K, ρ is the density in kg/m^3, $T'=T/T_c$, $\rho'=\rho/\rho_c$, where the subscript c indicates that the property value is at the critical point, $\Delta T=1-T'$, $\Delta\rho=1-\rho'$, and R is the universal gas constant. The values for carbon dioxide are listed in Appendix A.

To compare the accuracy of the Peng-Robinson cubic equation of state with the empirical 27-parameter expression, the error in pressure calculation of supercritical carbon dioxide using the two expressions at isochors of 0.5 and 0.6 g/cc as a function of temperature in the range 305-350 K is illustrated in Figure 8.3. It can be seen that the calculation with the Peng-Robinson equation of state led to a substantial error in pressure evaluation. The 27-parameter empirical equation of state shows little deviation from empirical results[94].
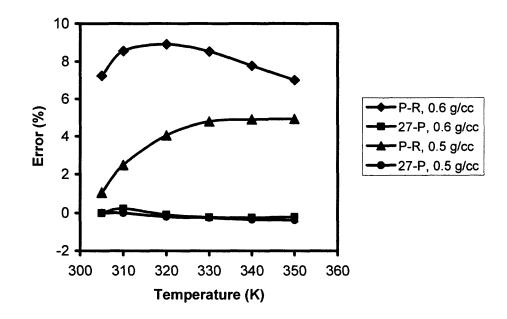
Figure 8.3 Error in the pressure calculation of supercritical carbon dioxide using the Peng-Robinson equation of state and the 27-parameter empirical equation of state at the 0.5 and 0.6 g/cc isochors for temperatures ranging from 305 to 350 K.

8.3.2 Nozzle Inlet Flow Calculations

Calculation of the carbon dioxide properties were performed by simultaneous numerical solution of Equations 8.3 to 8.5 in conjunction with the 27-parameter equation of state. Maple version 9 software package was used in the computation.

The flow within the nozzle inlet region, stage II, may be considered as gradually converging from the cross sectional area of the feed duct down to the cross sectional area at the nozzle entrance. In this region heat transfer and frictional effects were neglected as the flow was assumed to be adiabatic and inviscid. Calculation of the fluid properties along this region was performed by solving Equations 8.3 to 8.5 setting f to zero.

The calculations were performed as follows. For a desired pre-expansion temperature and pressure the experimentally measured mass flow rate was used to

calculate the axial velocity of the fluid at an arbitrarily chosen flow cross section area in pre-expansion stage. The initial values were calculated assuming a flow cross section with a 2 mm diameter. The calculated velocity together with the pre-expansion temperature and density were used as the initial values in the numeric solution of the system of differential Equations 8.3-8.5. The flow properties were calculated along the converging flow from the initial cross section area with a 2 mm diameter to the cross section area at the nozzle entrance. The converging flow cone angle was also chosen arbitrarily as the rate of change of the cross sectional area has no influence on the results in such one-dimensional calculation.

The values of C_v and C_p are required in these calculations as a function of both temperature and pressure along the expansion axis. Such data may be calculated from the equation of state. However, due to the burdensome nature of such calculations, especially with the 27-parameter equation, the values were obtained by iteratively fitting the values along the expansion path of the fluid using empirical data[94]. The initial calculation was typically performed by using estimated mean values of C_v and C_p. This was followed by several iterations of fitting empirical C_p and C_v values to the calculated temperature and pressure profiles along the expansion axis. Typically two iterations were sufficient for adequate convergence, stability of values within 1%.

A representative set of carbon dioxide flow properties was calculated to model the flow in the inlet region of a laser drilled sapphire nozzle with a 150 μm inner diameter with a 250 μm channel length having a tapered inlet and a flat outlet. The calculations were based on 350 bar pre-expansion pressure and 354 K pre-expansion temperature. The mass flow rate, m, for this nozzle at the given pre-expansion conditions was determined

from the calibration, Figure 8.1. The initial velocity in the pre-expansion stage at the 2 mm diameter cross section was calculated from the empirical mass flow rate according to:

$$v = \frac{m}{\rho A}$$ (8.10)

The calculated flow properties at the starting and the end points of the nozzle inlet stage are listed in Table 8.1. The fluid properties are given at two axial positions in this stage, z_{II}. The location at the beginning of stage II, where the acceleration due to convergence starts is marked as z_{II} = 0 cm. Here the flow cross section diameter (D) was assumed to be 2 mm. Position z_{II} = 0.411 cm is the end point of stage II where the flow cross section diameter is equal to the value at the nozzle entrance, 0.15 mm. The fluid properties included at the corresponding locations are the linear velocity, Mach number, temperature, pressure, and density.

Table 8.1 Calculated Properties at the Start and End Points of the Nozzle Inlet Stage

z_{II} (cm)	D (mm)	v (m/s)	M	T (K)	P (bar)	ρ (g/cc)
0	2	1.08	0.002	354.0	350.0	0.785
0.411	0.15	211.9	0.547	331.3	182.5	0.707

The calculated pressure, temperature, velocity, and Mach number profiles along the expansion path of the nozzle inlet stage are presented in Figure 8.4.
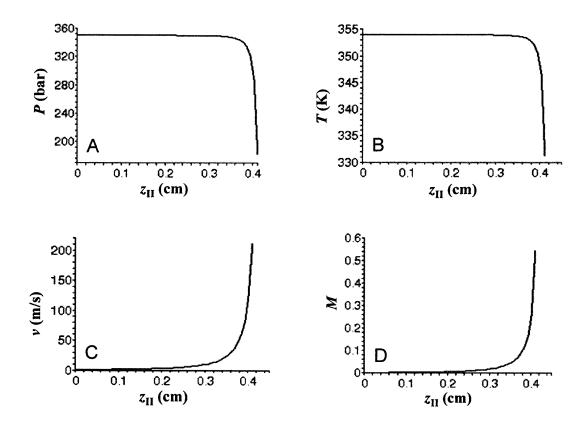
Figure 8.4 Calculated properties of expanding carbon dioxide along the nozzle inlet stage: temperature (A), pressure (B), velocity (C), and the Mach number (D).

The calculations reveal a substantial pressure and temperature drop across the nozzle inlet stage as a result of the flow convergence. It can be seen in Figure 8.4 that most of the changes occur within 0.05 cm of the nozzle entrance. The expanding fluid reaches a high velocity at the nozzle entrance with a corresponding Mach number of around 0.55. A large pressure drop occurs at the inlet stage, nearly 168 bar. Carbon dioxide remains in the supercritical state during expansion across the inlet stage.

The calculated value of the pressure at the end of the nozzle inlet stage represents the maximum possible value since inviscid flow at the nozzle inlet stage was assumed. The contribution of the nozzle inlet region to the overall changes in the fluid properties

will increase as the nozzle length is shortened. For example, in the case of an infinitesimally short nozzle, in order to meet the requirement of sonic flow at the nozzle exit the entire pressure drop will occur in the nozzle inlet region. The opposite is true for much longer nozzles, where the contribution of the inlet region may be negligible. These results also indicate that little pressure or temperature drop should be expected along the length of the feed tubing upstream of the nozzle.

8.3.3 Nozzle Flow Calculations

The flow of supercritical carbon dioxide inside the nozzle (stage III) differs from that in the inlet region in that the cross sectional area is constant along the expansion path. Here the pressure drop is assumed to result solely from wall friction. At this stage the flow is assumed to be adiabatic as heat transfer through the nozzle wall is minimal due to the low residence time. Due to the presence of viscous dissipation as a result of wall friction and high turbulence the flow is non-isentropic. Such adiabatic compressible flow with wall friction is often referred to as Fanno flow[95].

The flow calculations along this stage were performed similarly to those along the inlet stage. However, the differential of the cross sectional area with respect to axial position z was set to zero and the friction term f was included. The conditions at the end of stage II were used as initial conditions for the flow calculations inside the nozzle. The calculations were performed iteratively by adjusting the value of the friction factor f in order to meet the required Mach 1 velocity at the nozzle exit, a required condition due to chocked flow. The heat capacity profiles were determined in the same manner as was done for the nozzle inlet region. A sample Maple input code is shown in Appendix B.

The residence time of the fluid inside the nozzle τ was calculated based on the average velocity which was determined by integration of the velocity profile using the mean value theorem:

$$\tau = \frac{\bar{v}}{\Delta z} \qquad (8.11)$$

where,

$$\bar{v} = \frac{\int_{z=0}^{z} v(z)\, dz}{\Delta z} \qquad (8.12)$$

The calculated properties of carbon dioxide at the nozzle entrance and exit are given in Table 8.2. The entrance position is indicated as $z_{III} = 0$ cm; the nozzle exit is indicated as position $z_{III} = 0.025$ cm.

Table 8.2 Calculated Flow Properties at the Nozzle Entrance and Exit

z_{III} (cm)	D (mm)	v (m/s)	M	T (K)	P (bar)	ρ (g/cc)	τ (μs)
0	0.15	211.9	0.55	331.3	182.5	0.707	0
0.025	0.15	243.1	1	309.9	89.7	0.616	1.12

The calculated pressure, temperature, velocity, and Mach number profiles along the expansion path inside the nozzle are presented in Figure 8.5.
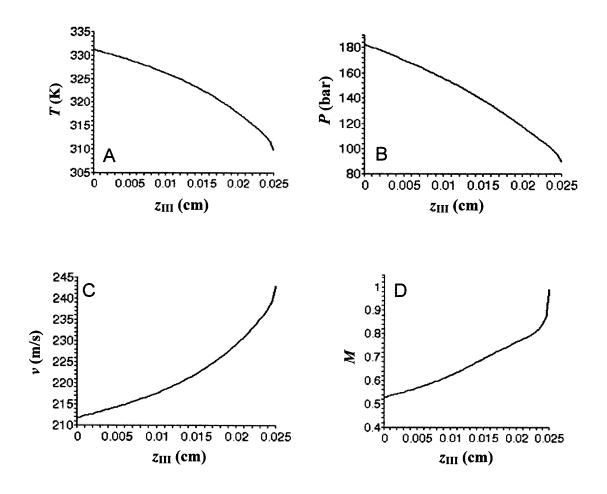
Figure 8.5 Calculated properties of expanding carbon dioxide along the nozzle: temperature (A), pressure (B), velocity (C), and the Mach number (D).

The calculated residence time of the fluid inside the nozzle is 1.12 μs. On such short time scale a pressure drop of around 93 bar is achieved with a corresponding temperature drop of around 21 K. The values of the temperature and pressure at the nozzle outlet indicate that the carbon dioxide remains in the supercritical state at the nozzle exit.

The friction factor *f* was found to be 0.027 in this calculation. This value exceeds the expected value which can be estimated using the Blasius empirical expression for flows with Reynolds number (Re) above 2×10^4 for smooth pipes[96]:

$$f = \frac{0.184}{\text{Re}^{1/5}} \qquad (8.13)$$

The calculated friction factor at the average Re inside the nozzle, around 4.5 x 10^5, is 0.014. The discrepancy in the value of the friction factor can be accounted for as follows. In the calculations described above all viscous losses which are represented by the value of f are assumed to occur inside the nozzle, while at the nozzle inlet the flow was considered to be inviscid. Due to the low aspect ratio of the nozzle considered in the calculations, it is likely that there are losses at the nozzle inlet as well[81, 92]. As a rough approximation, assuming that the friction factor value based on Equation 8.13 is accurate, the discrepancy in the value may be assumed to represent the losses at the inlet stage. Helfgen et al. demonstrated for a nozzle with aspect ratio equal to unity, calculations of the inlet flow allowing for around 1 % entropy increase were in better agreement with experimental data than the assumption of isentropic flow[81]. For longer nozzles such entrance losses should become less significant in comparison to internal wall friction losses. Based on calculations the overall entropy increase during subsonic expansion up to the nozzle exit is around 0.25%.

Although such considerations raise questions as to the accuracy of the profiles of flow properties along the subsonic expansion path, they should not impact the calculated values at the nozzle exit.

8.4 RDX Supersaturation during Expansion

Expansion of the supercritical carbon dioxide/RDX solution up to the nozzle exit at the pre-expansion conditions considered in the above calculations shows that the carbon dioxide remains in the supercritical state. Consequently, no condensation of carbon dioxide can occur. However, due to the substantial drop in the pressure and temperature, the dissolved RDX may begin to precipitate before the nozzle exit.

Supersaturation is defined as $S = C/C_E$, where C is the actual concentration of the dissolved solute and C_E is the equilibrium concentration of the solute. Based on the solubility of RDX in carbon dioxide the supersaturation profiles were calculated along the subsonic expansion path up to the nozzle exit. The supersaturation profiles along the nozzle inlet, stage II, and along the nozzle, stage III, are shown in Figures 8.6 and 8.7 respectively. The values represent supersaturation for 350 bar extraction pressure and 338, 348, and 354 K extraction temperatures. For all cases the solution is assumed to be at 354 K and 350 bar prior to expansion. This implies that following extraction at 338 and 348 K, the solution was further heated at constant pressure in order to achieve an undersaturated state prior to expansion. The comparison is presented to determine whether moderate overheating may delay precipitation until the free-jet downstream of the nozzle. This may be desirable as all precipitation will take place under uniform conditions and at supersaturation levels orders of magnitude higher due to the rapid pressure and temperature drop in the free-jet.
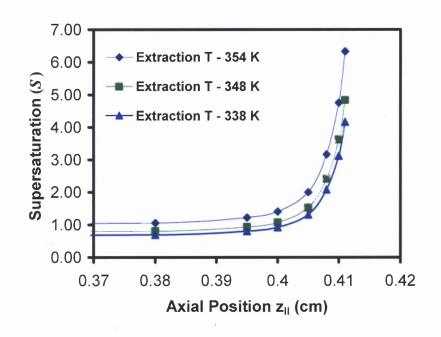
Figure 8.6 RDX supersaturation profiles along the nozzle inlet stage.
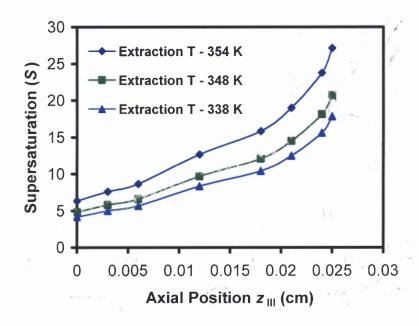
Figure 8.7 RDX supersaturation profiles along the nozzle stage.

As a rule of thumb, the onset of homogeneous nucleation becomes significant when the supersaturation value reaches *ca.* 4[80]. Thus it can be concluded from the above calculations that significant precipitation of RDX will begin as early as the nozzle inlet for all three scenarios considered. It can be seen that moderate overheating is not sufficient to delay precipitation until the free jet.

The supersaturation values shown in Figures 8.6 and 8.7 are the potential values assuming no precipitation takes place. Any precipitation of the supersaturated solute, which is likely to occur, would lower the value of the actual supersaturation. Implementation of a nucleation and precipitation model in conjunction with the solubility along the calculated expansion path was not attempted in this work, however, would be required in order to calculate the supersaturation profile accounting for the precipitated mass fraction of solute.

8.5 Effect of Pre-Expansion Pressure

Calculations were also performed to determine the dynamic and thermodynamic properties of carbon dioxide with pre-expansion pressures set at 280 and 310 bar at 354K. The calculations were performed analogously to the calculations with 350 bar pre-expansion pressure described earlier. The input mass flow rates were based on the flow calibration described in Section 8.2. The calculated flow properties for pre-expansion pressure set to 280, 310, and 350 bar pre-expansion pressure are summarized in Table 8.3. The pressures, temperatures, densities, and fluid velocities are shown at the end points of the nozzle inlet and the nozzle stages. The average friction factor values inside the nozzle as well as the input mass flow rates are included.

Table 8.3 Calculated Properties at the End Points of the Nozzle Inlet and Nozzle Stages

P_I (bar)	P_{II} (bar)	P_{III} (bar)	T_{II} (K)	T_{III} (K)	ρ_{II} (g/cc)	ρ_{III} (g/cc)	v_{II} (m/s)	v_{III} (m/s)	f	m (g/s)
350	182.5	89.7	331.3	309.9	0.71	0.62	211.9	243.1	0.027	2.66
310	170.7	90.7	332.3	311.3	0.67	0.58	196.6	227.0	0.030	2.35
280	169.8	88.7	334.8	311.2	0.65	0.55	179.2	212.2	0.039	2.08

The effect of decreasing the pre-expansion pressure at a constant temperature can be seen. In all cases the fluid remains in the supercritical state at the nozzle exit, thus, no condensation of CO_2 is expected. It can be seen that the mass flow rate increases with the pre-expansion pressure. The fluid density at the nozzle exit increases with the pre-expansion pressure. The calculated average friction factor inside the nozzle decreases with increasing pre-expansion pressure. This trend is consistent with that expected using Equation 8.13. At 280, 310, and 350 bar pre-expansion pressures and 354 K pre-expansion temperature the calculated fluid residence times inside the nozzle are 1.12, 1.21 and 1.32 μs respectively.

8.6 Free-Jet Expansion

Calculations of the carbon dioxide jet properties downstream of the nozzle were not attempted in this work, however, published results on supersonic jet expansion are reviewed.

Downstream of the nozzle the unconfined fluid expands supersonically in a free-jet. The transition to subsonic velocity is accompanied by shock wave formation where

recompression and a temperature spike occur. The residence time within the supersonic jet has been estimated to be less than 1 μs. The pressure within the supersonic jet can drop to a fraction of the downstream pressure with an accompanying severe drop in the temperature[70, 97]. Beyond the Mach disk the flow decelerates and reaches the ambient pressure and temperature due to entrainment of surrounding gas. The free-jet expansion up to the Mach disk is typically treated as isentropic and adiabatic.

Supersonic free-jet expansion of ideal gases is well described by existing empirical expressions. The diameter of the Mach disk, D_M, and the length of the supersonic jet, L_M, downstream of the nozzle can be estimated with the following expressions[70]:

$$L_M = 0.67 D_N \left(\frac{P_0}{P_a} \right)^{0.5} \qquad (8.14)$$

$$D_M = 0.5625 L_M \qquad (8.15)$$

where P_0 is the pre-expansion pressure, P_a is the ambient pressure downstream of the nozzle, D_N is the nozzle internal diameter at the outlet. The equations indicate that the location and size of the Mach disk are dependent on both the nozzle diameter as well as the pressure drop across the nozzle.

An estimate of these parameters for the expansion conditions considered in the calculations earlier, with expansion from 350 bar to atmospheric pressure across a 150 μm ID nozzle can be made using these expressions. For this set of expansion conditions the length from the nozzle exit to the Mach disk is around 1880 μm. The corresponding diameter of the Mach disk is around 1060 μm.

Calculations have shown that for expansions with a high pressure drop the fraction of fluid that goes through the Mach disk may be less than 25 %, while the rest of the fluid bypasses the Mach disk and transitions to subsonic flow via oblique shocks[70, 82]. This indicates that the flow field of the expanding fluid is not uniform and may have implications on particle formation within the expanding fluid. The calculations were performed without accounting for condensation. Condensation is expected to change the fluid properties along the jet.

Condensation of carbon dioxide within the free jet is expected to occur at expansion regimes relevant to the RESS process. Depending on the downstream pressure, which influences the velocity and temperature within the supersonic free jet, the condensation may lead to the formation of liquid carbon dioxide or at lower downstream pressures, dry ice. Due to the exothermic nature of condensation, the jet temperature is expected to rise, consequently limiting the extent of condensation.

Khalil modeled the free jet expansion of carbon dioxide from supercritical pre-expansion conditions[82]. A two-dimensional axi-symmetric numerical approach was used using the Redlich-Kwong equation of state. The following trends were revealed in the calculations. The effect of increasing the pre-expansion pressure from 80 to 200 bar at 70 °C led to a lengthening of the free jet with the pre-expansion pressure. The calculations also showed that the minimum temperature achieved in the free-jet, immediately before the Mach disk increased with pressure. Substantially slower cooling was also observed at the highest pressure, while at the lower pressures the bulk of cooling was achieved early in the free-jet. A higher pressure was also observed along the free-jet

with higher pre-expansion pressure. This trend indicates that the onset of carbon dioxide condensation would occur further down stream with increasing pre-expansion pressure.

8.7 Conclusions

The dynamic and thermodynamic flow properties of carbon dioxide were calculated along the subsonic expansion in the nozzle inlet and nozzle stages using a one dimensional compressible flow model. The nozzle inlet flow was considered to be adiabatic and inviscid. Expansion inside the nozzle was assumed to occur under adiabatic conditions, with losses due to wall friction. The calculation of flow properties for a set of expansion conditions relevant to this study revealed that a substantial expansion occurred at the inlet and nozzle stages. At all the conditions considered including expansion from 280, 310, and 350 bar and 354 K, the fluid remained in the supercritical state at the nozzle exit, which implies that no condensation of carbon dioxide is expected until the free jet downstream of the nozzle.

The expected supersaturation of the solute RDX was calculated along the subsonic expansion stages based on the calculated temperature and pressure profiles. It was demonstrated that the onset of RDX precipitation is expected to occur at the nozzle inlet stage. Moderate overheating of the saturated solution prior to expansion did not appear to significantly alter the location of the onset of RDX precipitation.

CHAPTER 9

EFFECT OF SOLVENT PRECIPITATION

9.1 Introduction

As was discussed in Chapter 4, a number of process parameters influence the size and morphology of particles produced by rapid expansion of supercritical solutions. These include process temperatures and pressures, solute concentration, as well as the nozzle dimensions. In this chapter the effects of carbon dioxide condensation on the particle size and morphology are examined. The experimental data gathered in this study as well as the results derived from the flow calculations are used in conjunction with the information available in the literature to present a qualitative description of the key trends of particle size dependence on the process conditions, specifically focusing on the role of solvent condensation.

For the range of conditions investigated in this study, a phase transition of carbon dioxide is expected. Depending on the expansion conditions solid or liquid phase condensate may form. Particle formation experiments by RESS performed in this study may be classified into two categories. Experiments with post-expansion pressures ranging from around 1 to 5 bar, at which freezing of the expanding carbon dioxide takes place, and experiments with elevated post-expansion pressures, ranging from around 5 to 65 bar, at which condensation of liquid carbon dioxide occurs. The pressure-enthalpy diagram for carbon dioxide, shown in Figure 9.1 is useful for determining the conditions at which the condensation of carbon dioxide occurs. The figure was constructed qualitatively based on the reference[98]. For a given set of pre-expansion temperature

and pressure, the conditions at the onset of condensation during isentropic expansion may be determined by following the expansion path along the isentropes which are shown in the diagram.
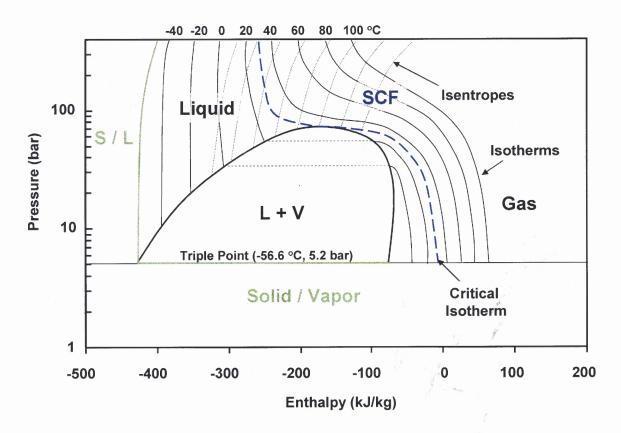
Figure 9.1 Pressure-enthalpy diagram of carbon dioxide.

Depending on the pre-expansion conditions, the onset of phase transition may occur during subsonic expansion upstream of the nozzle exit, or during supersonic free-jet expansion downstream of the nozzle.

For all conditions studied, chocked flow occurred, thus the flow properties are identical up to the nozzle exit for a given set of pre-expansion conditions, regardless of downstream conditions. Due to the chocked flow regime the extent of solute precipitation

and the particle size distribution will be identical regardless of the downstream conditions. Within the free-jet, the fluid conditions are strongly dependent on the downstream pressure. Therefore the final particle size and morphology can be influenced by the downstream conditions.

The flow calculations described in Chapter 8 revealed several important expansion process features during RESS. As is evident in the supersaturation profiles of the expanding solution for the set of conditions considered, precipitation of RDX can be anticipated to begin upstream of the nozzle entrance. The significance of such early onset of precipitation is that it occurs at supersaturation levels well below the values which are associated with precipitation within the supersonic free jet, where values in excess of 10^6 are achievable. At lower supersaturation levels larger critical nucleus size and slower nucleation rate are expected which may lead to a larger particle size compared to that expected from particle formation limited to the supersonic free-jet. The residence time of subsonic expansion is significantly longer compared to the supersonic free-jet expansion, which is less than *ca.* 1 μs.

The achievable supersaturation within the free-jet depends on the extent of solute precipitation prior to the nozzle exit. According to most accounts in the literature, it would be preferable to restrict all precipitation to the free-jet; however, as was shown in Chapter 8, the required conditions would often not be practical. It was demonstrated that overheating of the supercritical solution prior to the nozzle by as much as 16 °C had a very modest lowering of the supersaturation along the subsonic expansion path. Another approach by dilution of the supercritical solution prior to expansion is also not practical due to the increased demand of energy and reduced throughput.

Depending on the pre-expansion conditions the extent of precipitation during subsonic expansion will vary. Complete treatment of this problem requires the implementation of an applicable nucleation and growth model, which was not attempted in this work, but has been addressed in the literature[67, 73]. Mathematical description of the precipitation and growth processes downstream of the nozzle is much more challenging. Attempts have been made; however, existing models have not been successful at predicting the actual particle size. Difficulty in accurately describing the precipitation mechanisms arises from the complex flow properties especially in the free jet and at the transonic shocks.

The one-dimensional flow calculations described in Chapter 8 provide useful values of the fluid properties such as the temperature, pressure, and velocity up to the nozzle exit. For the pre-expansion conditions used in the calculations, it was determined that the fluid remained in the supercritical state up to the nozzle exit. This implies that condensation of carbon dioxide, which appears to influence the particle formation mechanism as will be subsequently addressed, may be delayed until the free-jet. It is also evident in Figure 9.1 that condensation inside the nozzle may occur if, for example, the pre-expansion temperature is moderately lowered.

For the expansion conditions considered in Chapter 8 the onset of RDX precipitation begins at the nozzle inlet and intensifies inside of the nozzle. Even though precipitation is ongoing, the supersaturation will likely increase due to the continuing expansion of the fluid with a corresponding reduction in the solubility. The residence time at these stages has important implications and can affect the extent of precipitation. The residence time within the nozzle inlet is on the order of 100 μs while the residence

time in the 250 μm long nozzle is around 1 μs. Much longer capillary nozzles will have longer residence times and thus larger extent of precipitation should be anticipated. The nozzle diameter and aspect ratio are thus important parameters for design considerations.

An abrupt change occurs as the fluid exits the nozzle. In the region from the nozzle exit up to the Mach disk the expansion is supersonic and isentropic. In this region the density of the fluid approaches that of the downstream values on the time scale of around a microsecond. Due to the abrupt density change in the free jet with an accompanying drop in the fluid temperature, a drastic rise in the supersaturation of the solution takes place which has been estimated to exceed 10^6[66, 67]. At such large value of supersaturation calculations indicate that the critical nucleus size will be that of a single molecule[69]. This has the implication that at such conditions all molecules can be considered as precipitate and the resulting particle growth to be purely a consequence of coagulation rather than nucleation and condensation[68]. The extent of precipitation prior to the free-jet will determine the amount of consumed solute and thus will limit the achievable supersaturation in the free-jet. If a substantial fraction of solute remains dissolved, a burst of precipitation will occur in the free-jet, leading to a high population of small nuclei. Particle growth solely by coagulation will follow, where all clusters as well as single molecules of the solute are considered to be precipitate since they meet or exceed the critical nucleus size.

Coagulation mechanisms have been described in the literature and have been reviewed in Chapter 4. The mechanisms described in the literature only consider aerosol coagulation of particles suspended in the gas stream. The calculated rates of coagulation under-predict the particle growth rate as compared to experimental results. However, at

experimental conditions of interest in this work, it is evident that such scenario is not fully representative of the actual expansion conditions. For the entire range of conditions investigated in this work, with the pre-expansion pressures ranging from 100 to 350 bar, pre-expansion temperatures ranging from 50 to 90 $^{\circ}$C, and post-expansion pressures ranging from atmospheric to 65 bar, condensation of the solvent carbon dioxide was expected. The effect of carbon dioxide condensation on the particle formation is likely very significant and may be responsible for the limited accuracy of the mechanisms considered in literature.

9.2 Solvent Condensation during RESS

As was shown in Chapter 8, the precipitation of RDX occurs substantially earlier than condensation of carbon dioxide. It has been suggested in the literature that nearly all of solute can be assumed to have been precipitated prior to the onset of the solvent condensation[73].

Since at the onset of carbon dioxide condensation precipitation of RDX has likely completed, the presence of RDX nanoparticles may influence the condensation of carbon dioxide. The RDX aerosol nanoparticles are likely seeds for condensation of carbon dioxide. Such heterogeneous condensation will occur at lower supersaturation of carbon dioxide as compared to homogeneous precipitation, and thus will occur earlier in the expansion. Depending on post-expansion pressure, solid or liquid condensate can form on the surface of RDX nanoparticles.

The notion of RDX particles serving as seeds for heterogeneous condensation of carbon dioxide was introduced in Section 6.3. The efficient collection of RDX

nanoparticles by encapsulation in dry ice and sedimentation necessarily requires heterogeneous condensation of carbon dioxide on the surface of RDX.

Additional evidence of the effect of RDX aerosol on the condensation of carbon dioxide in the expanding jet was experimentally observed in a study by Matsunaga[99, 100]. Using *in situ* imaging based on ultraviolet light scattering, the particle size evolution within the expanding jet was investigated downstream of the nozzle. Experimental details are provided in the references. The effect of RDX on the condensation of carbon dioxide expanding from 90 bar and 80 °C to atmospheric pressure can be seen in Figure 9.2. Shown are frames taken at several distances from the nozzle exit. The cloudy appearance of the solution containing RDX can be attributed to the high population of RDX nanoparticles which serve as seeds and result in the formation of a large number of small particles of carbon dioxide. In contrast, carbon dioxide precipitated homogeneously exhibited a smaller number of larger particles.

Matsunaga also observed an effect of RDX on the carbon dioxide jet temperature along the expansion axis. A significantly higher temperature was measured when RDX was present. This further shows that RDX facilitates the condensation of carbon dioxide. The temperature rise can be attributed to a earlier onset and thus a higher extent of condensation, which is an exothermic process.
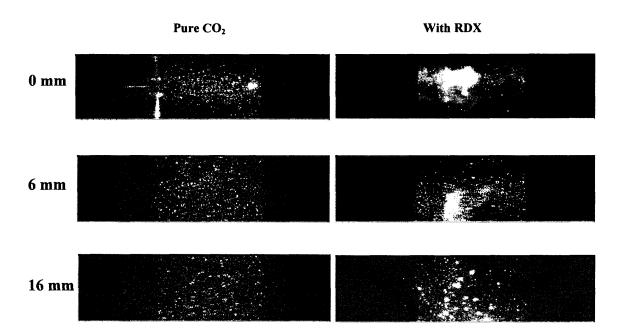
Figure 9.2 The effect of RDX on the condensation of carbon dioxide during expansion from 90 bar, 80 °C to atmospheric pressure.

For a set of pre-expansion conditions, such that the onset of carbon dioxide precipitation occurs downstream of the nozzle exit, the state of the precipitate will primarily depend on the downstream pressure. Expansion to downstream pressures below 5.2 bar, the triple point pressure of carbon dioxide, will necessarily lead to the formation of solid carbon dioxide. Expansion to pressures above 5.2 bar is expected to result in precipitation of liquid phase carbon dioxide.

As a result of heterogeneous condensation on a large number of RDX nanoparticles, a high population of condensate will appear. These RDX containing droplets (or solid particles) of carbon dioxide will likely undergo coagulation by the same mechanisms as was described in Section 4.2.2. In the case of liquid droplets a higher efficiency can be expected as the probability of rebounding of two liquid droplets is much lower than for solid particles. Due to the higher coagulation efficiency and no size

limitation for coagulation larger droplets are expected of liquid carbon dioxide than particles of solid carbon dioxide. An illustration of heterogeneous precipitation of carbon dioxide on RDX followed by coagulation is shown in Figure 9.3.

RDX Precipitation   Heterogeneous CO_2 Condensation CO_2 Coagulation
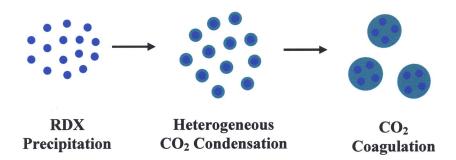
Figure 9.3 Heterogeneous condensation and coagulation of carbon dioxide in the presence of RDX precipitate.

It is reasonable to assume that at the onset of heterogeneous condensation of carbon dioxide on the surface of RDX nanoparticles the growth of RDX by coagulation will seize.

9.3 Precipitation and Growth of RDX during Subsonic Expansion

The subsonic flow calculations in this work and elsewhere[68, 71, 73]indicate that solute precipitation in the subsonic jet occurs at substantially lower supersaturation levels as compared to precipitation in the supersonic free-jet downstream of the nozzle. Therefore, different particle size may be expected for expansion conditions such that precipitation occurs solely within the subsonic jet. For the range of process conditions investigated in this work, it is anticipated that precipitation starts during the early stages of expansion at

the nozzle inlet and continues within the nozzle and perhaps to some degree within the free-jet.

At the conditions used in the calculation in Chapter 8, with pre-expansion pressures ranging from 280 to 350 bar at 354 K, it was shown that at the nozzle exit the carbon dioxide remained in the supercritical state. Consequently no condensation of carbon dioxide is expected inside the nozzle.

The density of carbon dioxide as well as the solute concentration increase with the pre-expansion pressure. Both of these factors contribute to a higher number density of RDX. Consequently, a higher supersaturation and precipitation rate are expected in the subsonic section of the expanding solution. Particle growth in the subsonic jet is aided by coagulation. The rate of coagulation is expected to increase with the number density of RDX nanoparticles within the jet.

It is expected that precipitation of RDX by expansion across a low aspect ratio nozzle from pre-expansion pressure 350 bar and temperature 354 K, should be nearly completed prior to the nozzle exit. These assertions are supported by calculations by Weber et al., who showed that the extent of precipitation increases with the pre-expansion pressure[73]. Their calculations revealed that for a short, low aspect ratio nozzle, similar to the nozzle considered in this study, the extent of precipitation is expected to approach unity at the nozzle exit at pre-expansion pressure above 320 bar. It was also shown that precipitation of solute will likely occur by formation of sub 5 nm particles whose size distribution will remain relatively constant with extent of precipitation and will begin to increase as coagulation takes over at conditions where nearly all solute has precipitated. The calculations indicate that growth of nanoparticles

by coagulation inside the nozzle becomes relevant as pre-expansion pressures exceed ca. 250 bar. The calculations were performed for a pre-expansion temperature of 383 K. This is substantially higher than the temperature considered in this study. The fluid density decreases with temperature, thus at the lower temperature considered here, 354 K, the extent of precipitation as well as the coagulation rate should be higher.

For the pre-expansion pressure of 350 bar and temperature 354 K it can be concluded that at the nozzle exit the precipitation has nearly reached completion or is fully completed and growth of particles occurs solely by coagulation. Since for this set of pre-expansion conditions condensation of carbon dioxide is not expected inside the nozzle, rather downstream in the free-jet, further coagulation is expected in the free-jet until the onset of carbon dioxide condensation where, as was assumed earlier, coagulation is expected to seize. The trends also indicate that reducing the pre-expansion pressure or increasing the pre-expansion temperature would lower the extent of precipitation and coagulation inside the nozzle.

9.4 Precipitation and Growth of RDX within the Supersonic Jet

The conditions in the free-jet are strongly dependent on the downstream pressure. However, as was mentioned earlier, due to the chocked flow regime, the downstream pressure has no effect on the subsonic flow properties upstream of the nozzle exit and thus has no effect on precipitation and particle growth. The extent of precipitation and the particle size distribution at the nozzle exit will be identical for varying downstream pressures. Thus, the variation in particle size and morphology for a set of pre-expansion conditions will be mainly due to the growth within the free-jet and beyond.

9.4.1 Expansion to Near-Atmospheric Pressures

At expansion conditions that favor the formation of solid carbon dioxide, it is reasonable to assume that shortly after the onset of heterogeneous condensation the growth process of RDX by coagulation will halt. Precipitation of RDX at such conditions was described in Chapter 6 where condensation of solid carbon dioxide was exploited in the collection of RDX nanoparticles. The recovery of the trapped RDX particles from the solid carbon dioxide matrix was achieved by sublimation at ambient conditions. No coagulation of RDX is expected during sublimation as no forces are exerted on the RDX particles. Therefore, the particle size distribution of RDX at the onset of carbon dioxide condensation is expected to be preserved.

Crystals grown by aerosol coagulation mechanisms are expected to be nearly spherical due to the random addition of smaller particles[85]. Accordingly, the final shape of RDX particles is also expected to be nearly spherical. Crystals with well defined facets, on the other hand, are grown by near equilibrium precipitation, at low supersaturation levels where reversible monomer deposition leads to a facet based selectivity and thus non-uniform growth rate of different facets.

Examination of the particle morphology of RDX precipitated by expansion to near atmospheric pressures where condensation of solid carbon dioxide occurs, the particle morphology indeed appears to be isotropic, with approximately spherical shape. Representative SEM images of RDX crystals formed by expansion to near atmospheric pressures at several pre-expansion conditions are shown below. An SEM image of RDX particles precipitated by expansion of a supercritical solution at 350 bar and 85 °C to 1

bar across a 150 micron ID nozzle is shown in Figure 9.4. The mean particle size is around 150 nm. Majority of crystals appear to have a spherical morphology.
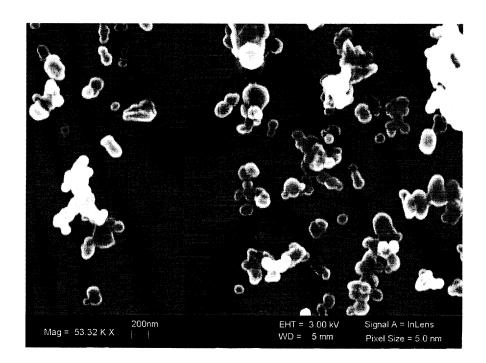
Figure 9.4 SEM image of RDX recrystallized by expansion across a 150 µm ID nozzle from 350 bar and 85 °C to 1 bar downstream pressure.

An SEM image of RDX crystals produced by expansion from 340 bar and 85 °C to 2 bar across a 200 micron ID nozzle, is shown in Figure 9.5. Although a significant change in the particle size can be seen, with a mean particle size around 700 nm, a similar spherical or near-spherical crystal morphology and a relatively narrow size distribution was observed, which is consistent with the particle morphology expected as a result of coagulation. The discrepancy in the particle size can be attributed to the large nozzle ID, which is expected as was described in Section 4.1. The effect of higher post-expansion pressure also needs to be considered. An increase from 1 to 2 bar, reduces the expansion

pressure ration by a factor of 2 and according to the Equation 8.14, leads to a shortening of the free-jet by a factor of $2^{1/2}$.
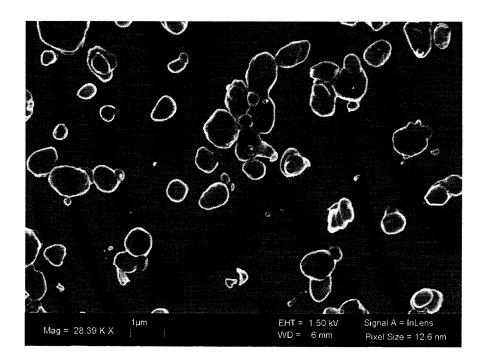
Figure 9.5 SEM image of RDX recrystallized by expansion across a 200 μm ID nozzle from 350 bar and 85 °C to 2 bar downstream pressure.

The effect of decreasing the pre-expansion pressure on the particle size is evident in Figure 9.6. Shown is an SEM image of RDX produced by expansion across a 200 micron ID nozzle by expansion from 310 bar and 85 °C to 2 bar downstream pressure. The mean particle size is around 350 nm. This sample also exhibits the similar spherical morphology, which again appears to result from coagulation by similar mechanisms as in the prior two examples.

Mag = 38.82 K X   300nm   EHT = 3.00 kV   Signal A = InLens
                            WD = 3 mm   Pixel Size = 6.8 nm
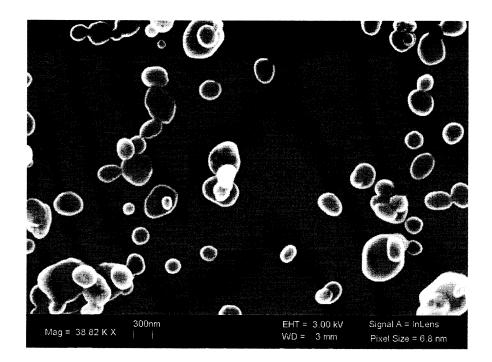
Figure 9.6 SEM image of RDX recrystallized by expansion across a 200 μm ID nozzle from 310 bar and 85 °C to 2 bar downstream pressure.

9.4.2 Expansion to Elevated Pressures

Increasing the post-expansion pressure has several effects on the expansion of the compressed carbon dioxide downstream of the nozzle exit. However, as was mentioned earlier, should have no effect on the subsonic expansion up to the nozzle exit. As was described in Section 8.6, the dimensions of the supersonic free-jet are a function of the overall pressure drop. As the post-expansion pressure is elevated, the length of the free-jet will shorten and the Mach disk will move closer to the nozzle exit. For example, using Equation 8.14, expansion to 60 bar from 350 bar across a 150 μm nozzle will lead to a free-jet length of around 250 μm, expansion to 1 bar results in a nearly 1900 μm free-jet. The diameter of the Mach disk will also be correspondingly smaller. The peak free-jet velocity will be lower for higher discharge pressures. The temperature and pressure drop

will decrease. Condensation of liquid carbon dioxide rather than solid can be anticipated, as can be seen in Figure 9.1.

A new particle growth mechanism appears to have a significant role with expansion to elevated pressures. Near-isentropic and adiabatic expansion from pre-expansion conditions of interest in this work to pressures ranging from around 5 to around 73 bar is expected to result in the condensation of carbon dioxide and formation liquid droplets by heterogeneous condensation on the surface of precipitated RDX nanoparticles as described earlier. Due to the presence of RDX seeds, condensation will likely initiate at relatively low supersaturation values of carbon dioxide. Condensation, as was mentioned earlier, is expected to halt further growth of RDX by coagulation. Unlike with expansion to near atmospheric pressures, freezing of carbon dioxide is not expected at these conditions. The condensed droplets are likely to grow by coagulation, forming larger droplets with several trapped RDX nanoparticles as was illustrated in Figure 9.3. The extent of carbon dioxide condensation will decrease with the post expansion pressure.

In the absence of freezing the separation of RDX from carbon dioxide will occur further downstream by evaporation of carbon dioxide droplets. This was accomplished experimentally by heating the expansion chamber as discussed in Chapter 7. Evaporation will begin at the Mach disk or the oblique shocks where a rapid temperature and pressure rise occurs[82]. Bonnamy et al. observed a decrease in the particle size of carbon dioxide immediately downstream of the Mach disk using in situ FTIR spectroscopy[101]. Droplets of carbon dioxide will continue to evaporate beyond the Mach disk, where the subsonic jet is heated due to entrainment of warmer gas from the surrounding.

It appears that a new coagulation mechanism of RDX may become relevant due to the evaporation of the carbon dioxide droplets. As the droplets containing RDX nanoparticles evaporate, the RDX nanoparticles within each droplet are brought together and compressed with substantial forces due to the surface tension forces of the carbon dioxide liquid droplets. Such compression may be the source of further coagulation of RDX nanoparticles. Growth by coagulation mechanisms described in Section 4.2.2 within the liquid phase carbon dioxide is unlikely due to the substantially lower relative particle velocities. Growth by Ostwald ripening is also not expected due to the short time scale prior to droplet evaporation.

The droplet size of carbon dioxide will depend on the RDX number density and the extent of precipitation of carbon dioxide which depends on the temperature and pressure. Droplets will grow by coagulation in the expanding fluid. Due to high shear forces generated at the Mach disk and the oblique shocks, droplet brakeage may occur. As only 25 % or so of the fluid is estimated to cross the Mach disk[70] while the rest is expected to undergo deceleration at the oblique shocks a non uniform expansion environment exists which may lead to a wider size distribution of droplets and consequently of the RDX crystals. The free-jet velocity may also impact the drop size. At higher velocities large velocity gradients may be present leading to shearing of large droplets.

The proposed coagulation mechanism appears to explain the unexpectedly large particle size obtained during RESS. With such mechanism the final particle size would depend on the carbon dioxide droplet size and the quantity of trapped RDX. Expansion

conditions which favor the coagulation of carbon dioxide droplets would also favor the formation of larger crystals of RDX.

The characteristics of RDX crystals produced by RESS with expansion to elevated pressures where liquid carbon dioxide formation is favored are examined. SEM images of RDX recrystallized by expansion from 320 bar and 85 °C to 60 bar post-expansion pressure across 150 and 250 micron ID nozzles are shown in Figures 9.7 and 9.8 respectively. Expansion across the smaller ID nozzle produces particles with size ranging from 250 to 1000 nm. The morphology of the smaller particles appears to be nearly spherical while the larger particles tend to have an irregular morphology. Increasing the nozzle ID leads to a dramatic increase in particle size, with sizes ranging from around 0.5 to over 3 microns. The particles appear to have a highly irregular morphology.

One effect of increasing the nozzle diameter appears to be an increase in the size of carbon dioxide droplets. This may be a consequence of the increased dimensions of the free jet, which appears to lead to a larger extent of carbon dioxide coagulation. The final particle size will depend on the drop size, which upon evaporation leads to the large irregular RDX particles.
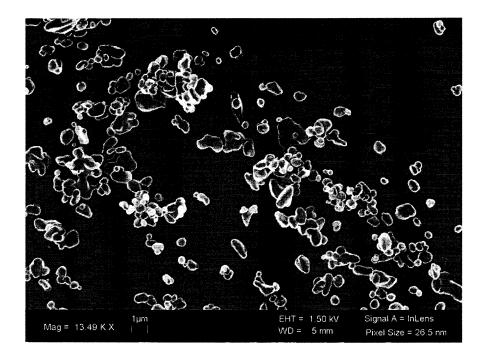
Figure 9.7 SEM image of RDX recrystallized by expansion across a 150 μm ID nozzle from 320 bar and 85 °C to 60 bar downstream pressure.
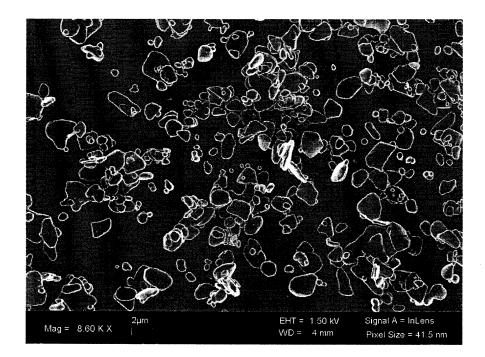
Figure 9.8 SEM image of RDX recrystallized by expansion across a 250 μm ID nozzle from 320 bar and 85 °C to 60 bar downstream pressure.

Representative SEM images of RDX produced by expansion across a 100 μm ID
nozzle, from 280 bar and 85 °C to post-expansion pressures set to 10 and 45 bar are
shown in Figures 9.9 and 9.10 respectively. Large irregular shaped particles can be
observed at the higher pressure, while with expansion to 10 bar a substantially smaller
particle size and near spherical morphology can be seen. This sample resembles the
crystals produced by expansion to near atmospheric pressures. Expansion to 10 bar may
result in freezing of carbon dioxide. The pressure in the late stages of the free-jet can
drop to a fraction of the downstream pressure prior to being recompressed by the shock
waves.
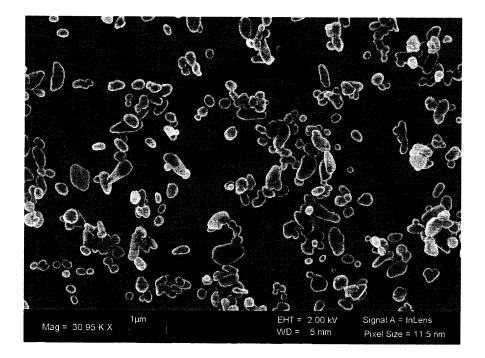
Figure 9.9 SEM image of RDX recrystallized by expansion across a 100 μm ID nozzle
from 280 bar and 85 °C to 10 bar downstream pressure.
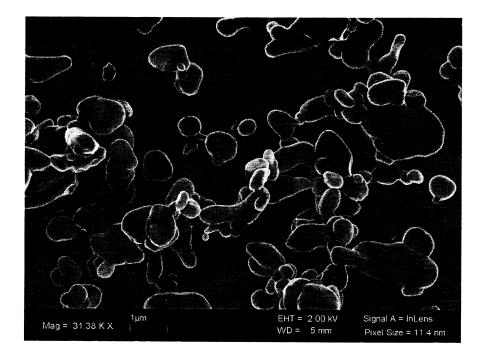
Figure 9.10 SEM image of RDX recrystallized by expansion across a 100 μm ID nozzle from 280 bar and 85 °C to 45 bar downstream pressure.

The largest crystals were produced by expansion from 350 bar and 85 °C to 60 bar across a 250 μm ID nozzle. An SEM image is shown in Figure 9.11. A magnification of the boxed section is shown in Figure 9.12. Particles with dimensions in excess of 3 μm were produced. The irregularity in the particle morphology is especially pronounced in this sample. A clear distinction in the morphology and size is evident in comparison to particles produced by expansion to near atmospheric pressures. This distinction is attributed mostly to the difference in the particle growth due to coagulation by liquid droplet evaporation. The irregular shape is evidently a result of droplet deformation prior to evaporation which is not unexpected.
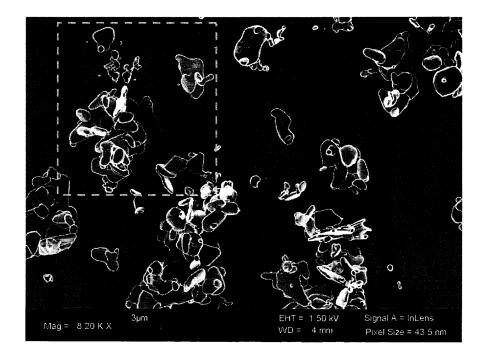
Figure 9.11 SEM image of RDX recrystallized by expansion across a 250 µm ID nozzle from 350 bar and 85 °C to 60 bar downstream pressure.

Figure 9.12 Enlargement of boxed portion of image in Figure 9.11.

It is should be reiterated that due to chocked flow the particle size distribution and morphology at the nozzle exit should be identical for similar pre-expansion conditions and nozzle dimensions, regardless of the downstream conditions. The differences in the size distribution and morphology of the collected RDX crystals are attributed to the growth downstream of the nozzle.

Majority of RESS studies in the literature primarily dealt with expansion conditions such that condensation of carbon dioxide is avoided. Condensation is generally believed to negatively impact the final particle size and morphology as well as introduce additional complexity which is difficult to model. Such conditions were achieved by working at low pre-expansion pressures and drastically overheating the supercritical solution prior to expansion. Another approach is by using long capillary nozzle which can be heated leading to a nearly isenthalpic expansion. Such approaches are poorly suitable for bulk production by RESS due to a greatly increased energy demand and a reduced throughput.

Based on the analysis provided in this chapter, it appears that condensation may be preferred since particle growth by aerosol coagulation may be mitigated. This is especially the case for conditions where solid carbon dioxide heterogeneously condenses on the surface of the solute nanoparticles. The smallest particle size obtained in this work was at conditions where the precipitated RDX was trapped in solid carbon dioxide early in the expansion. Liquid carbon dioxide condensation may also have favorable effects, however, processing conditions should be chosen such that the formation of large droplets of carbon dioxide by coagulation is avoided. As was demonstrated, this can be achieved by using smaller ID nozzles.

9.5 Conclusions

The effect of post-expansion pressure on the particle growth downstream of the nozzle was examined. The growth of RDX particles was shown to be affected by condensation of the solvent. It was demonstrated that condensation of carbon dioxide occurs heterogeneously on the surface of RDX nanoparticles. The effect of solvent condensation on RDX growth varied for liquid and solid phase condensate. Growth of the condensed particles of carbon dioxide is expected by coagulation resulting in larger particles containing RDX nanoparticles.

A nearly spherical morphology was commonly observed at conditions favorable for solid carbon dioxide formation, while irregular shaped particles were formed at expansion conditions where liquid condensate was formed. Condensation was proposed to affect particle growth as follows. At the onset of condensation it was suggested that the particle growth is halted, regardless whether the condensate is in the liquid or solid state. Encapsulation in dry ice is expected to preserve the particle size achieved at the onset of condensation. No additional growth is expected during separation of the particles from the dry ice by sublimation. In the case of liquid phase carbon dioxide condensation growth of RDX nanoparticles is halted at the onset of condensation, however, growth of particle appears to be possible resulting from evaporation of the liquid droplets containing RDX nanoparticles. A growth mechanism was suggested which occurs by evaporation of liquid droplets which leads to compression of contained RDX nanoparticles leading to particle growth by coagulation. The irregular morphology of RDX crystals produced at conditions where liquid condensation occurred appears to support this proposed mechanism.

A favorable effect of condensation was demonstrated, in contrast to the widely perceived negative effects of condensation in the literature. Limiting the extent of coagulation by solvent condensation appears to be a more practical solution than methods described in the literature including dilution of the expansion chamber with air and addition of a second solute as was described in Section 4.2.2.

CHAPTER 10

SENSITIVITY AND PEFORMANCE TESTING

Sensitivity testing was performed on samples of RDX recrystallized by the RESS process. Testing of sensitivity to stimuli including electrostatic discharge, impact, and shock was performed using standard military methods. Two types of recrystallized RDX were tested. Type A nano RDX with a mean crystal size around 150 nm and Type B nano RDX with a mean crystal size around 500 nm. Commercially available RDX with a 4.8 micron mean particle size was used as the reference. This reference material is produced by milling with a fluid energy mill. Type A nano RDX has a specific surface area (SSA) around 15-20 m^2/g, Type B nano RDX has a SSA around 5-6 m^2/g. The reference 4.8 micron RDX has a SSA of around 1 m^2/g. Both types of RDX recrystallized by RESS contained around 1 % HMX from HPLC analysis. The reference material contained about 8-10 % HMX. Both Type A and B recrystallized RDX samples were determined to be crystalline by powder XRD analysis. Sensitivity testing of the novel RDX samples as well as the reference materials was performed in both the pure state as well as in wax based formulations.

10.1 Formulation Preparation and Characterization

Processing of nanocrystalline RDX into useful energetic formulations poses a number of challenges. Nanocrystals of organic compounds exhibit poor stability in liquid media. In the sub-micron and nano regimes, the crystals are highly susceptible to Ostwald ripening. This is a mechanism by which crystals suspended in a saturated solvent will undergo size

enlargement driven by the reduction of the surface free energy. The extent of the size enlargement is a function of the initial crystal size, solution temperature, and the residence time. This effect is severe for nanocrystalline materials. Consequently, if a liquid media is used in processing nanocrystalline materials, the final product may consist of a significantly altered material with respect to the original material, and as a result the benefits of size reduction may be lost.

In order to mitigate the effect of Ostwald ripening, nanocrystals may be stabilized with appropriately chosen surfactants in liquids which are weak solvents of the material. Such approach has been successfully demonstrated in stabilizing nanocrystalline pharmaceutical compounds[102-104].

Surfactants also aid in dispersion of nanocrystals which is necessary prior to deposition of the coating material. Dispersion of nanoparticles in an incompatible liquid medium has several difficulties. There is a high tendency of nanoparticles to agglomerate. This is not surprising as the interfacial tension increases with surface area of the dispersed material. Agglomeration is highly favorable as the surface forces are greatly reduced. The high surface area of nanoparticles, 6-20 m^2/g for RDX samples in this work, complete dispersion would lead to a tremendous surface free energy. Surfactants aid in overcoming the large surface energy by reducing the interfacial surface energy between the aqueous phase and the nanocrystals.

10.1.1 Slurry Coating of RDX

Formulations were prepared by slurry coating. A wax binder was used. The binder consisted of 70 % Chlorez 700 SSNP wax and 30 % Paroil 170 T plasticizer. Both were

acquired from Dover Chemical Corp. The target composition of the formulations was 88 wt. % RDX and 12 wt. % binder.

Coating involved preparation of an aqueous slurry of RDX. Due to the highly hydrophobic nature of RDX addition of surfactant was necessary to aid dispersion. Lecithin was used to aid dispersion of RDX. A baffled stirred vessel was used to prepare the formulations. RDX was added to the aqueous medium consisting of 90 % water and 10 % methyl ethyl ketone (MEK). The surfactant, lecithin, and RDX were added and the solution was mixed at around 500 RPM for 15 minutes. High RPM aided in dispersion of RDX. Next, a MEK based lacquer solution containing the binder was gradually added to the slurry followed by stirring for 30 minutes. The binder precipitated due to the low solubility in the aqueous phase and was deposited on the dispersed RDX. The product was collected by vacuum filtration and oven dried at $ca.$ 80 °C overnight.

The composition of the coated samples was determined by HPLC analysis. The weight fraction of RDX and HMX in the formulations containing Type A, Type B, and the reference 4.8 micron RDX are listed in Table 10.1.

Table 10.1 Composition of Prepared Formulations

Sample	% RDX	% HMX	% Energetic	% Binder
4.8 Micron RDX / wax	79.3	8.4	87.7	12.3
Type A nano RDX / wax	85.8	1.6	87.4	12.6
Type B nano RDX / wax	85.0	1.3	86.3	13.7

The composition closely matched the ratio of ingredients loaded during slurry coating. Small quantities of HMX are present in the recrystallized samples of RDX. The ratio of HMX to RDX is lower than in the precursor RDX. This is expected since the solubility of HMX in supercritical carbon dioxide is substantially lower.

As was described in Section 2.3, the coating quality can have a significant impact on the sensitivity of explosive formulations. It is desired that coating of individual crystals rather than agglomerates is achieved. Coating of agglomerates may lead to the inclusion of empty voids as well as placing individual explosive crystals in direct contact. This may lead to elevated sensitivity and, due to a lower density of the explosive charge, to a decrease in the performance.

10.1.2 Coating Characterization

It was of interest to analyze the wax distribution on the surface of RDX crystals. Conventional SEM and TEM analysis is inadequate as the wax cannot be distinguished from the RDX. Images taken by SEM and TEM of formulated RDX are shown in Figure 10.1.

A high-resolution imaging technique capable to spectroscopically differentiate between the coating material and RDX as well as map their spatial distribution with approximately 7.5 nm spatial resolution was utilized[99]. The technique is based on low-loss electron energy loss spectroscopy (EELS). The microscopy was performed using a Philips CM-20 Scanning Transmission Electron Microscope (STEM) with a field-emission electron source and a high-efficiency Gatan Enfina 776 magnetic-prism EELS spectrometer. The specimen was held at -171 °C using a Gatan cryo-transfer stage.
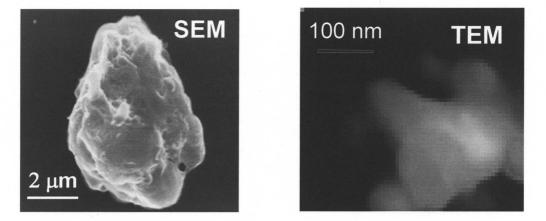
Figure 10.1 SEM (left) and TEM (right) images of wax coated RDX nanoparticles.

The low-loss electron energy loss spectra collected from specimens of pure wax deposited on a thin-film carbon substrate and pure RDX deposited on a thin-film carbon substrate are shown in Figure 10.2.
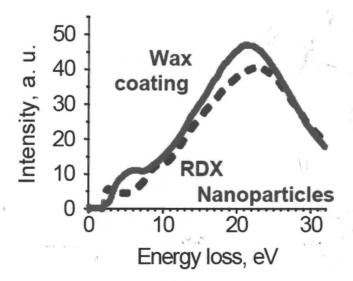
Figure 10.2 Low-loss EELS spectra of pure wax and pure RDX.

The spectra shown in Figure 10.2 are sufficiently distinctive and can be used to map the amounts of each component present in specimens containing both wax and RDX. EELS

imaging of coated samples was performed by scanning the sample with a focused electron beam approximately 3-5 nm full-width at half maximum. A sample analysis is shown in Figure 10.3. The wax and RDX are mapped separately showing the distribution of the two materials. The wax and RDX spectra along the white line in Figure 10.3 are shown in Figure 10.4.
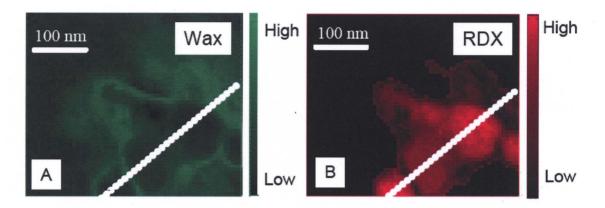
Figure 10.3 Spatially resolved maps of the wax (A) and RDX (B) by EELS analysis.
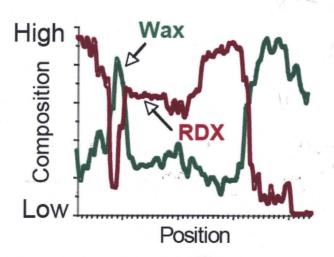
Figure 10.4 Wax and RDX profiles along the white line in Figure 10.3.

The analysis revealed that individual particles as well as agglomerates of particles were coated by wax. In addition, it was observed that clumps of wax were present. This technique was found to be useful for the analysis of coated clusters and individual crystals.

Based on the TEM-EELS analysis as well as the density measurements of the pressed explosive (described below) it appears that the slurry coating method employed in the preparation of the RDX/wax formulations does not provide the coating quality desired. Incomplete dispersion of RDX prior to coating is likely a key issue. Coating of clusters leads to void inclusion and a consequently a reduced density.

10.2 Sensitivity Testing

Standard sensitivity tests were performed to asses the response of the samples to shock, impact, and electrostatic shock discharge. The samples were dried in an oven at around 40 °C to a constant weight before testing.

10.2.1 Electrostatic Discharge Sensitivity Testing

The electrostatic sensitivity test was performed to determine the ignition threshold due to an electrostatic stimulus. The method is described in MIL-STD-1751A, dated 11 December 2001, Method 1032, "Electrostatic Discharge Sensitivity Test (ARDEC(Picatinny Arsenal)Method)". The recrystallized and the reference 4.8 micron RDX samples were analyzed in their pure and coated forms. None of the samples were initiated in 20 trials at 0.25 joules, the maximum energy level of the test apparatus. These results indicate that accidental electrostatic discharge poses a very low risk of initiation.

10.2.2 Impact Sensitivity Testing

The impact sensitivity tests were performed using an ERL, Type 12 impact tester, with a 2.5 kg drop weight. This method is described in MIL STD 1751A, Method 1012 "Impact Sensitivity Test-ERL(Explosives Research Laboratory)/Bruceton Apparatus." The test is performed by dropping the drop weight from incremental heights and recording whether initiation occurs. The drop height is adjusted in order to determine the height at which initiation probability is 50% (H_{50}). The impact sensitivity is given as the H_{50} value.

The sample is typically loaded in loose form. The sample rests on a disk of 180 grit sandpaper which is placed on top of the anvil. The sandpaper greatly lowers the impact height necessary for initiation. The grit material is believed to aid in the formation of hot spots upon impact due to frictional heating. The sample size required for this test is 35 ± 5 mg.

Impact test results for the uncoated samples of RDX are shown in Table 10.2. The results show that both Type A and Type B samples of nanocrystalline RDX have a substantially lower impact sensitivity (higher H_{50}) than the reference 4.8 micron RDX. Also included is the impact sensitivity of Class 5 RDX which is a commercial form of RDX with a mean size around 15-30 microns with a wide size distribution. Class 5 RDX was the most sensitive. The results indicate that a significant sensitivity reduction is achieved by crystal size reduction to nano-scale dimensions. However, the trend of sensitivity reduction with crystal size reduction appears not to continue down to the smallest crystal size investigated. Type A nano RDX exhibited a higher sensitivity than the coarser Type B nano RDX.

Table 10.2 Impact Sensitivity Test Results for Uncoated RDX Samples

Material	Impact Sensitivity H_{50} (cm)
Class 5 RDX	23
4.8 Micron RDX	32.2 ± 0.7
Type A nano RDX	57.3 ± 1.3
Type A nano RDX (pellets)	42.0 ± 0.9
Type B nano RDX	73.5 ± 1.9

As was described in Section 6.8.4, the tap density of nanocrystalline RDX powder is substantially lower than that of the larger grained samples such as the Class 5 RDX. In order to minimize the effect of the sample density when comparing impact sensitivity of the fine grained with larger grained samples, an additional test was performed on pressed pellets of Type A nano RDX. Around 30 mg samples of pure RDX were pressed at low pressure to produce each pellet. The pellets pressed with the nanocrystalline RDX were intact after pressing. An attempt to produce pellets using class 5 RDX and 4.8 micron RDX failed as the pellets readily crumbled.

As can be seen in Table 10.2, Type A nano RDX in the denser pellet form is more sensitive to impact initiation than the lower density loose powder. The test with the pressed pellets is likely a better comparison to class 5 and 4.8 micron RDX samples due to elimination of the large discrepancy in the sample density. The sensitivity of the pressed pellets of Type A nano RDX is substantially lower than the reference samples including the 4.8 micron RDX and Class 5 RDX.

Impact sensitivity testing was also performed on formulations consisting of ca. 88 wt. % RDX and wt. 12 % wax. The impact test results are summarized in Table 10.3.

Table 10.3 Impact Sensitivity Test Results for Wax Coated RDX Samples

Material	Impact Sensitivity H_{50} (cm)
Coated 4.8 micron RDX	26.2 ± 0.7
Coated Type A nano RDX	45.5 ± 1.0
Coated Type B nano RDX	62.0 ± 1.5

The results with the coated samples reveal a similar pattern as seen with the uncoated samples. The nanocrystalline RDX based formulations show a substantially lower sensitivity than the 4.8 micron RDX. Interestingly, in both the uncoated and coated samples the larger grained Type B nano RDX was less sensitive than Type A nano RDX. This may be an indication that a minimum may exist in the dependence of impact sensitivity on the crystal size and that reduction beyond a certain size may lead to increased sensitivity.

Another notable observation is that for all samples the coated material exhibited a higher sensitivity compared to the uncoated material. This outcome may partially be attributed to the consolidation of RDX during the coating process leading to a substantially higher density than the loose uncoated powder. Note the similarity in the sensitivity of the coated Type A nano RDX and the uncoated pellets of Type A nano RDX. The density is likely similar for these two samples.

10.2.3 Shock Sensitivity Testing

Shock sensitivity analysis was performed with the NOL Small-Scale Gap Test according to MIL-STD-1751A, Method 1042. The material to be tested was pressed into brass

cylinders at 16,000 psi. Around 1.5 grams of material were required for each cylinder. At least 12 cylinders were used per test.

Schematic of the small-scale gap test assembly is shown in Figure 10.5. The shock wave is generated by a donor explosive charge. The shock passes through an attenuating inert material (PMMA) with the degree of attenuation determined by the thickness of this material. The thickness of the PMMA spacer is adjusted to determine the pressure at which the probability of initiation is 50 %. The shock sensitivity is presented in terms of the shock pressure necessary for 50% initiation probability. The occurrence of detonation is determined based on the damage to the steel witness block which receives the blast resulting from the initiation of the test sample.
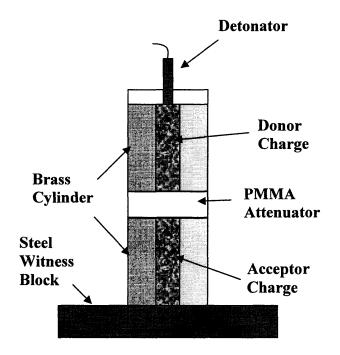
Figure 10.5 Small-scale gap test assembly.

The incident shocks in this test have a relatively low amplitude and long duration and are intended to represent shocks from unintended initiation sources such as adjacent detonations rather than sources such as detonators which have a substantially higher shock pressure and shorter shock duration.

The shock sensitivity results for the uncoated samples of recrystallized and reference RDX are presented in Table 10.4. The shock pressure is presented in both dBg and kbar units. For each sample, the density as well as the percentage of the theoretical maximum density (TMD) and the corresponding void fraction is included as they are important parameters influencing the shock sensitivity.

Table 10.4 Shock Sensitivity Test Results for Uncoated RDX Samples

Material	Shock Sensitivity (dBg)	Shock Sensitivity (kbar)	Sample Density (g/cc)	% TMD	% Void Space
4.8 Micron RDX	5.5	19.6	1.49	81.9	18.1
Type A nano RDX	5.65 ± 0.22	20.6	1.42	78.0	22.0
Type B nano RDX	6.38 ± 0.06	26.1	1.43	78.6	21.4

The small scale gap test results are also shown in Figure 10.6. Included in the Figure is the shock sensitivity of conventional RDX at various densities, obtained from the MIL-STD-1751A, Method 1042[14]. The effect of the sample density on the shock sensitivity is clearly illustrated for conventional RDX. As the density approaches the theoretical maximum value, the shock sensitivity decreases.
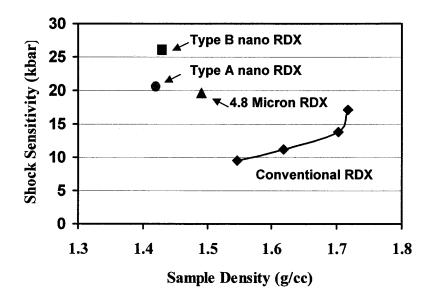
Figure 10.6 Shock sensitivity of uncoated samples of conventional, 4.8 micron, Type A nano, and Type B nano RDX.

As was discussed in Chapter 2, the shock sensitivity depends on the packing density of the pressed samples due to the effect of the void size on the hot spot formation. The sensitivity is expected to increase with the void fraction.

The data clearly show a decrease in shock sensitivity as the crystal size is reduced down to the nano-scale. However, the finer grained Type A nano RDX is substantially more shock sensitive than the Type B nano RDX.

Due to the low pressing density of the finer grained samples of RDX a large void fraction remains in the samples. Achieving a density closer to the TMD value may require pressing at substantially higher pressures as the mechanical strength of RDX increases as the crystal size is reduced. Potentially a multi-modal mixture consisting of both Type A and Type B nano RDX may lead to a higher packing density and a further reduction in the shock sensitivity.

The shock sensitivity was also assessed for formulations prepared with the recrystallized as well as reference RDX samples in a wax binder with 88 wt. % RDX and 12 wt. % wax. The test results are shown in Table 10.5.

Table 10.5 Shock Sensitivity Test Results for RDX/Wax Formulations

Material	Shock Sensitivity (dBg)	Shock Sensitivity (kbar)	Sample Density (g/cc)	% TMD	% Void Space
Class 1 RDX / Wax	5.5	19.6	1.69	94.9	5.1
4.8 Micron RDX / Wax	5.69	20.9	1.57	87.7	12.3
Type A RDX / Wax	6.23 ± 0.21	24.9	1.57	87.7	12.3
Type B RDX / Wax	7.03 ± 0.23	32.1	1.58	88.2	11.8

The shock sensitivity data indicate that the formulations prepared with the nanocrystalline samples are substantially less shock sensitive compared to the reference 4.8 micron RDX and Class 1 RDX with a mean particle size above 200 microns. The results also show that formulated Type B nano RDX is the least sensitive. The shock sensitivity data for the formulated samples are also shown in Figure 10.7.

A similar density was achieved for the 4.8 micron RDX and the recrystallized nano RDX samples by pressing at 16,000 psi. It should be noted that the densities achieved are substantially lower than what would be expected from a perfectly formulated mixture with the given composition. The low density of the pressed samples is an indication of non-uniform wax coating of RDX. As is evident in the TEM-EELS analysis of the formulated samples described above, wax coating of agglomerates as well as wax clumps were present in the formulation. Coating of agglomerates of RDX will

lead to a lower density as intercrystalline void space within the agglomerates is not filled. The clumps of wax present throughout the formulation also will lead to a reduced density as this wax was intended to coat crystals and fill the interstitial space.
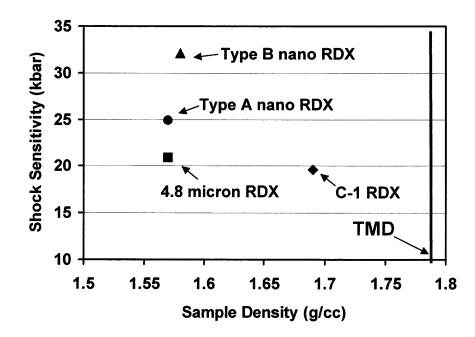
Figure 10.7 Shock sensitivity of wax coated Class-1, 4.8 micron, Type A nano, and Type B nano RDX.

These issues are likely related to the slurry coating process employed in the preparation of the formulations and indicate the difficulty of coating very fine crystals. The same coating method was used with class 1 RDX with a mean crystal size above 200 microns. Apparently a much better distribution of wax was achieved as is evidenced by the substantially higher density with a void fraction of around 5 %. This is much closer to the ideal value based on the composition. Improvements in the coating process of fine crystals are necessary to achieve optimal sensitivity properties of such novel explosive

formulations. Nevertheless, the data suggests that reduction of the mean crystals size leads to a substantial reduction in shock sensitivity for both pure as well as formulated samples.

10.3 Critical Thickness Analysis

The critical thickness is an important performance parameter. Tests were performed to assess the minimum thickness of explosive formulation which can sustain detonation. Formulations containing 95 wt. % RDX and 5 % binder were prepared. Tests were performed by preparing films of varying thickness on an aluminum witness sheet. The films were initiated with a detonator. Type A and B nano RDX samples as well as Class-5 RDX were tested. The detonation events results shown as "fire" and "no fire" are summarized for the varying samples as a function of thickness in Table 10.6.

The formulations containing nanocrystalline RDX samples appear to have a substantially lower critical thickness compared to the Class-5 RDX based formulation. The formulation with Type B nano RDX appears to have the lowest critical thickness. It detonated at 0.64 mm and did not detonate at 0.25 mm. It can be concluded that the critical thickness is in the range from 0.25 to 0.64 mm. Further testing in this thickness range will be required to accurately determine the critical value. Class-5 RDX did not detonate at highest thickness tested, 1.27 mm. These preliminary results are based on a single test performed per thickness per formulation. Further testing will be required to obtain statistically significant results.

Table 10.6 Critical Thickness Test Results

Material	Sample Thickness (mm)			
	1.27	0.75	0.64	0.25
Class-5 RDX	No Fire			
Type A nano RDX	Fire	Fire	No Fire	
Type B nano RDX	Fire	Fire	Fire	No Fire

10.4 Conclusions

The sensitivity of nanocrystalline samples of RDX was assessed to stimuli including electrostatic discharge, impact, and shock. Sensitivity testing of pure samples as well as formulations was performed. The sensitivity to electrostatic discharge was found to be negligible as no initiation occurred at the highest energy setting of the test apparatus. The impact test results revealed that the nanocrystalline samples exhibited substantially lower impact sensitivity than the reference 4.8 micron RDX. Similarly the nanocrystalline samples were substantially less shock sensitive than the reference material.

Both the impact and the shock sensitivity test results appear to indicate that the larger grained type B nano RDX is less sensitive than the finer grained Type A nano RDX. This result is true for both pure and formulated samples. The difference appears to be significant, on the order 25 % in most of the tests. Assessment of the test results points out that likely a minimum in the sensitivity exists as the size is reduced and that this minimum is above the grain size of Type A nano RDX.

The generally lower sensitivity of the larger grained RDX is surprising as both experimental and predicted trends discussed in Chapter 2 indicate that reduction in size

should lead to a lowered sensitivity to the stimuli tested in this work. The hot spot formation mechanisms which are responsible for explosive initiation discussed in Chapter 2 are expected to be more effective the larger grained Type B nano RDX. The observed trend suggests that a fundamentally different initiation mechanism may be responsible for initiation of Type A nano RDX. Further tests will be required to more accurately determine the mean particle size of RDX corresponding to the apparent minimum in sensitivity.

Another observation is the relatively low density of the pressed pure and formulated samples containing the fine grained RDX samples with pressing at 16,000 psi. For the pure samples this is likely a consequence of the enhanced mechanical strength with size reduction. In the formulations another contributing factor is the non-uniform distribution of the binder material. As was shown by TEM-EELS analysis, the binder appeared to coat agglomerates of RDX particles. In addition, the binder was found in clumps. As the sensitivity is known to correlate with the void fraction, improvement in the formulation quality of nanocrystals is required to achieve the optimal sensitivity characteristics.

Testing of the critical detonation thickness revealed that the formulations containing the nanocrystalline samples detonated at less than half the thickness of class-5 RDX. The formulation containing Type B nano RDX exhibited the lowest critical thickness. Conventional high explosives typically exhibit an increased critical diameter, which is proportional to critical thickness, with reduced sensitivity. The apparently novel characteristic of nanocrystalline RDX is the reduced sensitivity with a corresponding reduction in the critical diameter.

CHAPTER 11

CONCLUSIONS

11.1 Summary of Results

In an effort to produce the optimal form of the explosive RDX, size reduction to nano-scale dimensions was investigated. The sought after characteristics of the new form of RDX included low vulnerability to accidental initiation by unintended stimuli including shock and impact as well as similar or improved performance parameters including a reduction of the detonation failure diameter and improved shock wave spreading.

11.1.1 Recrystallization of RDX

Prior to this work nanocrystalline RDX was not available. Therefore, a method had to be developed for production of RDX with the desired particle size and morphology. The key desired characteristics of the novel form of RDX included a mean particle size ranging from around 100 to 1000 nm, narrow particle size distribution, spherical morphology, high purity, and minimal content of large crystal defects and inclusions. Recrystallization of RDX by rapid expansion of supercritical solutions (RESS) was identified as the most suitable method to achieve the desired product characteristics. Key advantages of RESS include the capability to reach the desired small particle size, characteristically high purity of recrystallized materials with no residual solvent, and safe processing due to mild processing temperatures and no mechanical stresses.

Extensive research on the recrystallization of RDX by RESS was performed. Carbon dioxide was used as the solvent. RDX was dissolved in supercritical carbon

191

dioxide and precipitated as fine particles upon expansion of the supercritical solutions across a nozzle. Initial experiments generated only sufficient quantities for particle size analysis by microscopy. These experiments generated the first samples of nanocrystalline RDX and demonstrated that RESS was indeed a viable route towards production of RDX nanoparticles.

To generate bulk quantities of RDX by RESS, an efficient collection method had to be developed. The difficulty of collecting aerosol RDX nanoparticles from the gas phase carbon dioxide at atmospheric pressure was overcome by the discovering that solid carbon dioxide (dry ice) heterogeneously condensed on the precipitated RDX particles during expansion. By sufficiently lowering the post-expansion temperature large agglomerates of dry ice formed and precipitated to the bottom of the expansion vessel. The recrystallized RDX was then recovered from the collected dry ice by sublimation. It was determined that such collection method was highly efficient resulting in near complete recovery of produced RDX nanoparticles.

The effect of process parameters on the particle size was investigated including pre-expansion temperature (50-90°C), pre-expansion pressure (100-350 bar) and post-expansion pressure (0-65 bar) as well as nozzle internal diameter (100-250 μm) with 250 μm nozzle length. The particle size was found to be sensitive to all the process parameters studied. The general trends included a reduction of the particle size with increase in the pre-expansion temperature, and an increase in particle size with post-expansion pressure as well as with the nozzle diameter. The mean particle size ranged from around 100 to 800 nm with a corresponding specific surface area ranging from around 30 to 3 m^2/g. The smallest particle size was achieved by expansion across a 100

μm ID nozzle from 90 °C and around 150 bar to atmospheric pressure. The particle size distribution was relatively narrow and followed a log-normal distribution. The collected particles appeared to have a spherical or near spherical shape with no apparent crystal facets. The produced particles were determined to be crystalline by powder X-ray diffraction analysis. The product exhibited high purity.

In order to produce an adequate quantity of nanocrystalline RDX for sensitivity and performance testing, continuous processing was developed. Due to the high consumption of carbon dioxide, recycling of the solvent was incorporated into the process. At near atmospheric discharge pressures recycling required the use of a compressor to recompress the expanded gas to around 60 bar, followed by cooling to liquefy the carbon dioxide in order to be fed back to the pump. An alternative processing mode was investigated by setting the discharge pressure to around 60 bar. This eliminated the need for compression and recycling was achieved solely by cooling to around 0-5°C. Operating at an elevated discharge pressure was found to greatly simplify the processing complexity as well as substantially reduced the energy demand of the process. The effect of elevated discharge pressure on the particle size and morphology was examined. A larger particle size with a specific surface area of around 5-7 m^2/g was produced at elevated discharge pressures.

Continuous recrystallization of RDX with throughput reaching around 6 g / hour was accomplished. The process was operated continuously up to around 5-6 hours. Bulk quantities were produced for testing.

To better understand the influence of process conditions on the particle size and morphology modeling of the supercritical fluid expansion was performed. A one-

dimensional compressible flow steady-state model was utilized to calculate the flow dynamics and thermodynamics of carbon dioxide expansion across a nozzle. The calculations focused on subsonic expansion at the nozzle inlet and inside the nozzle terminating at the nozzle exit. The pressure, temperature, and velocity profiles along these expansion stages were calculated. A significant pressure drop was found to occur at the nozzle inlet and inside the nozzle. Based on the pressure and temperature profiles the potential RDX supersaturation levels along the subsonic expansion stages were calculated. It was found that precipitation of RDX likely starts at the nozzle entry region. The calculations revealed that for the range of pre-expansion conditions considered the expanding carbon dioxide remained in the supercritical state up to the nozzle exit. This indicated that no condensation of solvent was expected inside the nozzle.

The influence of carbon dioxide condensation on particle formation during RESS was examined. Scenarios where liquid and solid phase condensation of carbon dioxide occurs were considered. Little attention has been given in the existing literature to the role of solvent condensation. Much of the published work on the RESS process focuses on conditions where no solvent condensation occurs. This is likely due to the additional complexity introduced by condensation which is difficult to model mathematically, and the prevalent notion that condensation negatively influences particle formation. It was found that for a wide range of useful processing conditions condensation will occur. To avoid carbon dioxide condensation during expansion would likely require impractical process conditions, which is the case for RDX recrystallization.

A positive influence of solvent condensation was outlined. A key benefit of condensation, which was demonstrated to occur heterogeneously on the surface of solute

precipitate, is the likely mitigation of solute growth by coagulation, which is believed to be responsible for the large particle size often obtained in experiments.

11.1.2 Sensitivity and Performance Analysis

The sensitivity and performance of the recrystallized and reference RDX samples were analyzed. Sensitivity was tested for incident stimuli including electrostatic discharge, impact, and shock. The detonation failure thickness was also experimentally measured.

Tests were performed on both pure samples as well as wax based formulations prepared by slurry coating. Two types of recrystallized RDX were tested, Type A nano RDX with a mean particle size around 150 nm and a specific surface area around 15-20 m^2/g, and Type B nano RDX with a mean particle size around 500 nm and a specific surface area around 5-6 m^2/g. Type A nano RDX was produced by RESS with expansion to near atmospheric pressures while the coarser Type B nano RDX was produced by expansion to around 55-65 bar. A commercially available fine grade RDX with a mean size around 4.8 microns was used as the reference.

Sensitivity testing reveled that the nanocrystalline grades of RDX were not vulnerable to accidental initiation by an electrostatic discharge. No initiation was obtained at the highest energy level tested, 0.25 J.

Both types of nano RDX exhibited a significantly reduced impact sensitivity compared to the reference material. A reduction for both coated and uncoated samples was observed. The coarser Type B nano RDX was found to have the lowest sensitivity.

A substantial reduction in sensitivity to shock was also found for the recrystallized samples based on the small-scale gap testing of both pure and formulated

samples. Once again Type B nano RDX exhibited the lowest sensitivity to shock in both pure and formulated forms.

The impact and shock sensitivity tests revealed that a minimum in sensitivity may exist with a corresponding crystal size larger than that of Type A nano RDX. This is surprising as most trends from experimental data as well as existing mathematical models predict a decrease in sensitivity as the particle size is reduced. Such reversal in the sensitivity trend may point to a transition to a fundamentally different initiation mechanism below a certain grain size.

Measurement of the detonation failure thickness was performed. The tests were performed with RDX formulations containing around 5 % polymeric binder. The tests revealed a substantial reduction of detonation failure thickness for the recrystallized samples. The formulation containing Type B nano RDX exhibited the lowest detonation failure thickness.

11.2 Recommendations

Further improvements to the RESS process will require a better understanding of complex expansion phenomena, especially downstream of the nozzle in the free jet and during the transonic flow where shock waves accompany the deceleration of fluid to subsonic velocities. The complex influence of spikes in temperature and pressure at the shock waves on particle formation need to be better understood. This is especially relevant in light of the profound effects of solvent condensation on the growth of particles during RESS.

Although a substantial reduction in shock sensitivity was demonstrated as a result of crystal size reduction to nano scale dimensions, the results are likely not optimal. The tested samples had a substantial void fraction. It is well known that voids may contribute to the initiation of energetic compounds. The high void fraction is in part due to the non-ideal coating of RDX by wax. Based on the STEM-EELS analysis, coating of RDX agglomerates by wax was found. This has the implications that the intercrystalline voids remain within the agglomerates. Elimination of such void would require a coating technology capable of producing individually coated crystals.

The above observations are an example of a general increase in the difficulty of processing of nanomaterials. Due to the high surface area and therefore increased tendency to agglomerate, processing of particles becomes more complex as the particle size is reduced. Improvements in nanoparticle coating technology will be required. This will include improvements in particle dispersion, e.g. with the use of surfactants, or implementation of novel methods of coating material deposition. The achievement of an energetic formulation with optimal sensitivity and performance characteristics will ultimately depend on the ability to process the nanomaterials.

The apparent presence of a minimum in sensitivity to shock and impact with size reduction warrants further research to determine the mean crystal size corresponding to this minimum. In addition, it would be of value to investigate the initiation mechanism responsible for the increased sensitivity below a certain crystal size.

APPENDIX A

CO$_2$ PARAMETER VALUES FOR 27-PARAMETER EQUATION OF STATE

Parameter values used for calculation of CO$_2$ properties with the 27-parameter equation of state, after F. Huang et al[93].

$$b_2 = c_1 + \frac{c_2}{T'} + \frac{c_3}{T'^2} + \frac{c_4}{T'^3} + \frac{c_5}{T'^4} + \frac{c_6}{T'^5}$$

$$b_3 = c_7 + \frac{c_8}{T'} + \frac{c_9}{T'^2} \; ; \quad b_4 = c_{10} + \frac{c_{11}}{T'} \; ; \quad b_5 = c_{12} + \frac{c_{13}}{T'}$$

$$b_6 = \frac{c_{14}}{T'} \; ; \quad b_7 = \frac{c_{15}}{T'^3} + \frac{c_{16}}{T'^4} + \frac{c_{17}}{T'^5} \; ; \quad b_8 = \frac{c_{18}}{T'^3} + \frac{c_{19}}{T'^4} + \frac{c_{20}}{T'^5}$$

Table A.1 Equation of State Parameter Values for CO$_2$

i	c_i	i	c_i
1	0.376194	15	-2.79498
2	0.118836	16	5.62393
3	-3.04379	17	-2.93831
4	2.27453	18	0.988759
5	-1.23863	19	-3.04711
6	0.250442	20	2.32316
7	-0.11535	21	1.07379
8	0.675104	22	-5.997240E-05
9	0.198861	23	8.853390E-05
10	0.216124	24	3.164180E-03
11	-0.583148	25	10
12	1.197470E-02	26	50
13	5.372780E-02	27	80000
14	2.652160E-02		

APPENDIX B

MAPLE INPUT FOR CO₂ FLOW CALCULATIONS

Sample input file for calculation of flow properties using Maple version 9. The case presented is for calculation of the dynamic and thermodynamic properties of expanding carbon dioxide within the nozzle (stage III).

```
> restart;
> with (DEtools):
> with (plots):
```

Input parameters:

```
> Tc:=304.2; Pc:=73.8;  R:=83.14/44; omega:= .224;
f:=0.033687; rhoc:=0.4676;
```

Constant volume and constant pressure heat capacity expressions as function of location along expansion axis:

```
> Cv:=(.9329294763+14012494.0026998986*z^5)*10;
> Cp:=(2.792790442+19006293223.8500862*z^6)*10;
     gamma1:=Cp/Cv;
```

Parameter values for 27 parameter EOS:

```
>a[2]:=c[1]+c[2]/(T(z)/Tc)+c[3]/(T(z)/Tc)^2+
c[4]/(T(z)/Tc)^3+c[5]/(T(z)/Tc)^4+c[6]/(T(z)/Tc)^5;

> a[3]:=c[7]+c[8]/(T(z)/Tc)+c[9]/(T(z)/Tc)^2;

> a[4]:=c[10]+c[11]/(T(z)/Tc); a[5]:=c[12]+c[13]/(T(z)/Tc);

> a[6]:=c[14]/(T(z)/Tc);

> a[7]:=c[15]/(T(z)/Tc)^3+c[16]/(T(z)/Tc)^4+
     c[17]/(T(z)/Tc)^5;
> a[8]:=c[18]/(T(z)/Tc)^3+c[19]/(T(z)/Tc)^4+
     c[20]/(T(z)/Tc)^5;
> c[1]:=0.376194; c[2]:=0.118836; c[3]:=-3.04379;
     c[4]:=2.27453; c[5]:=-1.23863; c[6]:=0.250442;
> c[7]:=-.115350; c[8]:=0.675104; c[9]:=0.198861;
```

```
      c[10]:=0.216124; c[11]:=-0.583148; c[12]:=0.0119747;
>  c[13]:=0.0537278; c[14]:=0.0265216; c[15]:=-2.79498;
      c[16]:=5.62393; c[17]:=-2.93831;
>  c[18]:=0.988759; c[19]:=-3.04711; c[20]:=2.32316;
      c[21]:=1.07379; c[22]:=-0.599724E-4;
>  c[23]:=0.885339E-4; c[24]:=0.316418E-2; c[25]:=10;
      c[26]:=50; c[27]:=80000;
```

27-Parameter EOS for CO2:

```
>P:=(R*T(z)*rho(z))*(1+a[2]*rho(z)/rhoc+a[3]*(rho(z)/rhoc)^
2+a[4]*(rho(z)/rhoc)^3+a[5]*(rho(z)/rhoc)^4+a[6]*(rho(z)/rh
oc)^5+a[7]*(rho(z)/rhoc)^2*2.71828^(-
c[21]*(rho(z)/rhoc)^2)+a[8]*(rho(z)/rhoc)^4*2.71828^(-
c[21]*(rho(z)/rhoc)^2)+c[22]*(rho(z)/rhoc)*2.71828^(-
c[27]*(1-T(z)/Tc)^2)+c[23]*(1-
rho(z)/rhoc)/(rho(z)/rhoc)*2.71828^(-c[25]*(1-
rho(z)/rhoc)^2-c[27]*(1-T(z)/Tc)^2)+c[24]*(1-
rho(z)/rhoc)/(rho(z)/rhoc)*2.71828^(-c[26]*(1-
rho(z)/rhoc)^2-c[27]*(1-T(z)/Tc)^2));
```

```
>  Z:=P*1/rho(z)/R/T(z);
```

Derivative of pressure with respect to density based on the EOS:
```
>  DPDRHO:=-0.1600000000e-11*(-
0.1180965910e13*T(z)^5+0.5352541865e23*T(z)*rho(z)-
0.2018202870e16*rho(z)^4*T(z)^4+0.1273965108e22*rho(z)^2*ex
p(-4.911001401*rho(z)^2)*T(z)^2-
0.3291410480e25*rho(z)+0.1238765934e27*rho(z)^2*exp(-
4.911001401*rho(z)^2)-0.1152142036e28*rho(z)^4*exp(-
4.911001401*rho(z)^2)+0.1466562432e28*rho(z)^6*exp(-
4.911001401*rho(z)^2)-0.3231868945e21*rho(z)*T(z)^2-
0.6324892688e25*rho(z)^6*exp(-
4.911001401*rho(z)^2)*T(z)+0.5772187702e25*rho(z)^4*exp(-
4.911001401*rho(z)^2)*T(z)-0.1709028264e13*exp(-
80049.94615+213.8578544*rho(z)-
228.6760634*rho(z)^2+526.0939223*T(z)-
.8649218788*T(z)^2)*T(z)^5*rho(z)^2-
0.7606297395e22*rho(z)^4*exp(-4.911001401*rho(z)^2)*T(z)^2-
0.7796059430e24*rho(z)^2*exp(-
4.911001401*rho(z)^2)*T(z)+0.6748372895e22*rho(z)^6*exp(-
4.911001401*rho(z)^2)*T(z)^2-
0.1900223650e13*T(z)^5*rho(z)+0.1869077070e13*rho(z)^2*T(z)
^5-0.3326876642e16*rho(z)^2*T(z)^4-
```

```
0.2980382755e18*rho(z)^2*T(z)^3-
0.9985661545e13*rho(z)^3*T(z)^5+0.8194246825e16*rho(z)^3*T(
z)^4-0.1479019832e13*rho(z)^4*T(z)^5-
0.2556655580e16*rho(z)^5*T(z)^4+8944007475.*exp(-
80009.94618+42.77157089*rho(z)-
45.73521267*rho(z)^2+526.0939223*T(z)-
.8649218788*T(z)^2)*T(z)^5*rho(z)+0.1598283232e13*exp(-
80049.94615+213.8578544*rho(z)-
228.6760634*rho(z)^2+526.0939223*T(z)-
.8649218788*T(z)^2)*T(z)^5*rho(z)-9563737680.*exp(-
80009.94618+42.77157089*rho(z)-
45.73521267*rho(z)^2+526.0939223*T(z)-
.8649218788*T(z)^2)*T(z)^5*rho(z)^2+302931394.*rho(z)*exp(-
0.3199997847e-18*(-
0.5000000000e12+1644044613.*T(z))^2)*T(z)^5-
0.3699418310e12*exp(-80049.94615+213.8578544*rho(z)-
228.6760634*rho(z)^2+526.0939223*T(z)-
.8649218788*T(z)^2)*T(z)^5-1986553430.*exp(-
80009.94618+42.77157089*rho(z)-
45.73521267*rho(z)^2+526.0939223*T(z)-
.8649218788*T(z)^2)*T(z)^5+0.1422067961e19*rho(z)*T(z)^3-
0.1825564935e15*rho(z)*T(z)^4)/T(z)^4;
```

Definition of sound velocity based on EOS and Cp/Cv ratio:
```
> c:=sqrt(gamma1*DPDRHO*10^6);
```

Mach number definition :
```
> M:=v(z)/c;
```

Derivative of flow cross section diameter along expansion axis, here equal to 0 since flow is inside constant diameter nozzle:
```
> DE4:=diff(DI(z),z)=0;
```

SYSTEM OF DIFFERENTIAL EQUATIONS(conservation of momentum, energy, and mass):

Derivative of density along expansion axis:
```
> DE1:=diff(rho(z),z)=-rho(z)/DI(z)/(M^(-2)-
1)*((1+1/Cv/rho(z)*DPDT)*2*f-2*diff(DI(z),z));
```

Derivative of pressure with respect to temperature:
```
>DPDT:=1.889545455*rho(z)*(1+2.138579983*(.376194+36.141355
01/T(z)-281531.8264/T(z)^2+63982453.14/T(z)^3-
0.1059661653e11/T(z)^4+0.6516121794e12/T(z)^5)*rho(z)+4.573
524343*(-
.115350+205.3180293/T(z)+18393.41759/T(z)^2)*rho(z)^2+9.780
```

```
847612*(.216124-
177.3516349/T(z))*rho(z)^3+20.91712492*(0.119747e-
1+16.34012836/T(z))*rho(z)^4+360.8141943*rho(z)^5/T(z)+4.57
3524343*(-78622694.30/T(z)^3+0.4811334264e11/T(z)^4-
0.7645037904e13/T(z)^5)*rho(z)^2*2.71828^(-
4.911004705*rho(z)^2)+20.91712492*(27813757.73/T(z)^3-
0.2606836278e11/T(z)^4+0.6044510707e13/T(z)^5)*rho(z)^4*2.7
1828^(-4.911004705*rho(z)^2)-0.1282557742e-
3*rho(z)*2.71828^(-80000*(1-0.3288089226e-
2*T(z))^2)+0.4139845164e-4*(1-
2.138579983*rho(z))*2.71828^(-10*(1-2.138579983*rho(z))^2-
80000*(1-0.3288089226e-2*T(z))^2)/rho(z)+0.1479570568e-
2*(1-2.138579983*rho(z))*2.71828^(-50*(1-
2.138579983*rho(z))^2-80000*(1-0.3288089226e-
2*T(z))^2)/rho(z))+1.889545455*T(z)*rho(z)*(2.138579983*(-
36.14135501/T(z)^2+563063.6528/T(z)^3-
191947359.4/T(z)^4+0.4238646612e11/T(z)^5-
0.3258060897e13/T(z)^6)*rho(z)+4.573524343*(-
205.3180293/T(z)^2-
36786.83518/T(z)^3)*rho(z)^2+1734.649315*rho(z)^3/T(z)^2-
341.7885061*rho(z)^4/T(z)^2-
360.8141943*rho(z)^5/T(z)^2+4.573524343*(235868082.9/T(z)^4
.1924533706e12/T(z)^5+0.3822518952e14/T(z)^6)*rho(z)^2*2.71
828^(-4.911004705*rho(z)^2)+20.91712492*(-
83441273.19/T(z)^4+0.1042734511e12/T(z)^5-
0.3022255354e14/T(z)^6)*rho(z)^4*2.71828^(-
4.911004705*rho(z)^2)-0.1282557742e-3*rho(z)*2.71828^(-
80000*(1-0.3288089226e-2*T(z))^2)*(526.0939223-
1.729843758*T(z))+0.4139845164e-4*(1-
2.138579983*rho(z))*2.71828^(-10*(1-2.138579983*rho(z))^2-
80000*(1-0.3288089226e-2*T(z))^2)*(526.0939223-
1.729843758*T(z))/rho(z)+0.1479570568e-2*(1-
2.138579983*rho(z))*2.71828^(-50*(1-2.138579983*rho(z))^2-
80000*(1-0.3288089226e-2*T(z))^2)*(526.0939223-
1.729843758*T(z))/rho(z));
```

Derivative of Temperature along the expansion axis:

```
> DE2:=diff(T(z),z)=T(z)/Cv/rho(z)^2*DPDT*diff(rho(z),z);
```

Derivative of velocity along expansion axis:

```
> DE3:=diff(v(z),z)=v(z)*(-1/rho(z)*diff(rho(z),z)-
2*diff(DI(z),z)/DI(z));
```

Numeric solution of system of differential equations:

```
> S:= dsolve({DE1,DE2,DE3,DE4, rho(0)=0.696, v(0)=20500,
T(0)=336, DI(0)=.015}, numeric):
```
Graphical output of calculated results:

```
> odeplot (S, [z, v(z)/100], 0..0.025, color=black,
thickness=2,view=[0..0.025,200..250]);
> odeplot (S, [z, T(z)], 0..0.025, color=black,
thickness=2);
> odeplot (S, [z, rho(z)], 0..0.025);
> odeplot (S, [z, DI(z)], 0..0.018);
> odeplot (S, [z, M], 0.0..0.025, color=black,
thickness=2,view=[0..0.025,0.4..1.05]);
> odeplot (S, [z, P], 0.0..0.025, color=black,
thickness=2,view=[0..0.025,90..200]);
> S(0.025);
> eval(P, S(0.025));
> odeplot (S, [z, Cp], 0.0..0.025);
```

REFERENCES

1. Meyer, R., J. Kohler, and A. Homburg, *Explosives*. 5th ed. 2005: Wiley-VCH.

2. Morris, J.B., *Solubility of RDX in Dense Carbon Dioxide at Temperatures Between 303 K and 353 K.* J. Chem. Eng. Data, 1998. **43**: p. 269-273.

3. Stepanov, V., *Production of Nanocrystalline Nitramine Energetic Materials by Rapid Expansion of Supercritical Solutions*. 2003, M.S. Thesis, NJIT.

4. Bowden, F.P. and A.D. Yoffe, *Initiation and Growth of Explosion in Liquids and Solids*. 1952: Cambridge University Press.

5. Gvishi, M. and A. Solomonovici, *The Initiation Threshold Sensitivity of LX-15 Explosive as a Function of its Grain Size*. Propellants, Explosives, Pyrotechnics, 1989. **14**: p. 190-192.

6. Armstrong, R.W., et al., *Crystal Size Dependence for Impact Initiation for Cyclotrimethylenetrinitramine Explosive*. J. Appl. Phys, 1990. **68**(3): p. 979-984.

7. Caulder, S.M., et al. *Effect of Particle Size and Crystal Quality on the Critical Shock Initiation Pressures of RDX/HTPB Formulations*. in *International Symposium on Detonation*. 2006.

8. Borne, L., J. Patedoye, and C. Spyckerelle, *Quantitative Characterization of Internal Defects in RDX Crystals*. Propellants, Explosives, Pyrotechnics, 1999. **24**: p. 255-259.

9. Mullin, J.W., *Crystallization*. 4th ed. 2001: Butterworth Heinemann.

10. Balzer, J.E., et al., *High-Speed Photographic Study of the Drop-Weight Impact Response of Ultrafine and Conventional PETN and RDX*. Combustion and Flame, 2002. **130**: p. 298-306.

11. Tarver, C.M., S.K. Chidester, and A.L.N. III, *Critical Conditions for Impact- and Shock-Induced Hot Spots in Solid Explosives*. J. Phys. Chem, 1996. **100**: p. 5794-5799.

12. Mishra, I.B. and L.J.V. Kieft. *Novel Approach to Insensitive Explosives*. in *19th International Annual Conference of ICT*. 1988. Karlsruhe, Germany.

13. Borne, L. *Influence of Intragranular Cavities of RDX Particle Batches on the Sensitivity of Cast Wax Bonded Explosives*. in *10th International Symposium on Detonation*. 1993.

14. MIL-STD-1751A, *Safety and Performance Tests for the Qualification of Explosives*, DoD, 2001.

15. Gifford, M.J., et al. *Unconventional Properties of Ultrafine Energetic Materials*. in *32nd Int. Annual Conference of ICT*. 2001. Karlsruhe, Germany.

16. Borne, L., J. Mory, and F. Schlesser, *Reduced Sensitivity RDX (RS-RDX) in Pressed Formulations: Respective Effects of Intra-Granular Pores, Extra-Granular Pores and Pore Sizes*. Propellants, Explosives, Pyrotechnics, 2008. **33**(1): p. 37-43.

17. van der Steen, A.C., H.J. Verbeek, and J.J. Meulenbrugge. *Influence of RDX Crystal Shape on the Shock Sensitivity of PBXs*. in *Ninth (International) Symposium on Detonation. 1989. p. 23-27.*

18. Borne, L. and A. Beaucamp. *Effects of Explosive Crystal Internal Defects on Projectile Impact Initiation*. in *12th International Symposium on Detonation*. 2002.

19. Hoffman, D.M., *Density Distributions of Cyclotrimethylenetrinitramines (RDX)*. Lawrence Livermore National Laboratory, Preprint UCRL-JC-147684, 2002.

20. Coffey, C.S., *Initiation Due to Plastic Deformation From Shock or Impact*, in *Energetic Materials Part 2. Detonation, Combustion*. 2003, Elsevier. p. 101-123.

21. Coffey, C.S. and J. Sharma, *Plastic Deformation, Energy Dissipation, and Initiation of Crystalline Explosive*. Physical Review B, 1999. **60**(13): p. 9365-9371.

22. Sharma, J., et al. *Nanostructure of Defects and Hot Spots of Explosives as Revealed by an Atomic Force Microscope*. in *Eleventh (International) Symposium on Detonation. 1998. p. 443-450.*

23. Gilman, J.J. *Direct Evidence of Chemical Reactions Induced by Shear-Strains*. in *Mat. Res. Soc.* 2004: 287-297.

24. Elban, W.L., R.W. Armstrong, and T.P. Russell, *Plasticity/Interfacial Energy Influences on Combustion-driven Cracking of RDX Energetic Crystals*. Philos. Mag., 1998. **A78**: p. 907.

25. Armstrong, R.W. *Dislocation-Assisted Initiation of Energetic Materials*. in *New Trends in Research of Energetic Materials, Eighth International Seminar*. 2005. University of Pardubice, The Czech Republic.

26.   Menikoff, R., *Micro-Gap Experiments and Insensitive Explosives*. Los Alamos National Laboratory, Report LA-UR-07-3363, 2007.

27.   Gutkin, M.Y. and I.A. Ovid'ko, *Plastic Deformation in Nanocrystalline Materials*. 2004: Springer.

28.   Moulard, H. *Particular aspect of the explosive particle size effect on shock sensitivity of cast pbx formulations*. in *Ninth Symposium on Detonation*. 1989. Portland, Oregon.

29.   Honodel, C.A., et al. *Shock initiation of TATB formulations*. in *Seventh International Detonation Symposium*. 1981.

30.   Lee, K., et al. *Synthesis, Detonation Spreading and Reaction Rate Modeling of Fine TATB*. in *11th Symposium on Detonation*. 1998.

31.   Kuklja, M.M. *Chemical Decomposition of Solid Cyclotrimethylene Trinitramine*. in *2001 Int. Conference on Computational Nanoscience and Nanotechnology*. 2001. South Carolina, USA.

32.   Jung, J. and M. Perrut, *Particle design using supercritical fluids: literature and patent survey*. Journal of Supercritical Fluids, 2001. **20**: p. 179-219.

33.   Vemavarapu, C., et al., *Design and process aspects of laboratory scale SCF particle formation systems*. Int. J. of Pharmaceutics, 2005. **292**: p. 1-16.

34.   Byrappa, K., S. Ohara, and T. Adschiri, *Nanoparticles synthesis using supercritical fluid technology - towards biomedical applications*. Advanced Drug Delivery Reviews, 2008. **60**: p. 299-327.

35.   de la Fuente Badilla, J.C., C.J. Peters, and J.de Swaan Arons, *Volume Expansion in Relation to the Gas-Antisolvent Process*. Journal of Supercritical Fluids, 2000. **17**: p. 13-23.

36.   Gallagher, P.M., M.P. Coffey, and V.J. Krukonis, *Gas Anti-Solvent Recrystallization of RDX: Formation of Ultra-fine Particles of Difficult-to-Comminute Explosive*. Journal of Supercritical Fluids, 1992. **5**: p. 130-142.

37.   Teipel, U., U. Forter-Barth, and H. Krause, *Crystallization of HMX-Particles by Using the Gas Anti-Solvent Process*. Propellants, Explosives, Pyrotechnics, 1999. **24**: p. 195-198.

38.   Tom, J.W. and P.G. Debenedetti, *Particle formation with supercritical fluids*. Journal of Aerosol Science, 1991. **22**(5): p. 555-584.

39.   Mohamed, R.S., P.G. Debenedetti, and R.K. Prud'homme, *Effects of Process Conditions on Crystals Obtained from Supercritical Mixtures.* AIChE Journal, 1989. **35**(2): p. 325-328.

40.   Yaws, C.L., *Chemical Properties Handbook.* 1998: McGraw-Hill.

41.   Sun, L., S.B. Kiselev, and J.F. Ely, *Multiparameter Crossover Equation of State: Generalized Algorithm and Application to Carbon Dioxide.* Fluid Phase Equilibria, 2005. **233**: p. 204-219.

42.   Bartle, K.D., et al., *Solubilities of Solids and Liquids of Low Volatility in Supercritical Carbon Dioxide.* J. Phys. Chem. Ref. Data, 1991. **20**: p. 713-756.

43.   Gupta, R.B. and J. Shim, *Solubility in Supercritical Carbon Dioxide.* 2006: CRC Press.

44.   Foster, N.R., et al., *Significance of the crossover pressure in solid-supercritical fluid phase equilibria.* Ind. Eng. Chem. Res., 1991. **30**: p. 1955-1964.

45.   Mohamed, R.S. and G.D. Holder, *High Pressure Phase Behavior in Systems Containing CO_2 and Heavier Compounds with Similar Vapor Pressures.* Fluid Phase Equilibria, 1987. **32**: p. 295-317.

46.   Trabelsi, F., K. Abaroudi, and F. Recasens, *Predicting the Approximate Solubilities of Solids in Dense Carbon Dioxide.* Journal of Supercritical Fluids, 1999. **14**: p. 151-161.

47.   Prausnitz, J.M., R.N. Lichtenthaler, and E.G. Azevedo, *Molecular Thermodynamics of Fluid-Phase Equilibria.* 1999: Prentice Hall PTR.

48.   Escobedo-Alvarado, G.N., S.I. Sandler, and A.M. Scurto, *Modeling of Solid-Supercritical fluid phase equilibria with a cubic equation of state-G^{ex} model.* Journal of Supercritical Fluids, 2001. **21**: p. 123-134.

49.   Coutsikos, P., K. Magoulas, and G.M. Kontogeorgis, *Prediction of solid-gas equilibria with the Peng-Robinson equation of state.* Journal of Supercritical Fluids, 2003. **25**: p. 197-212.

50.   Jessop, P.G. and W. Leitner, *Chemical Synthesis Using Supercritical Fluids.* 1999: Wiley-VCH.

51.   Johnston, K.P. and C.A. Eckert, *An Analytical Carnahan-Starling-van der Waals Model for Solubility of Hydrocarbon Solids in Supercritical Fluids.* AIChE Journal, 1981. **27**: p. 773-779.

52.   Kwauk, X. and P.G. Debenedetti, *Mathematical modeling of aerosol formation by rapid expansion of supercritical solutions in a converging nozzle.* Journal of Aerosol Science, 1993. **24**(4): p. 445-469.

53.   Ekart, M.P., et al., *Cosolvent Interactions in Supercritical Fluid Solutions.* AIChE Journal, 1993. **39**: p. 235-248.

54.   Ting, S.T., et al., *Chemical-Physical Interpretation of Cosolvent Effects in Supercritical Fluids.* Ind. Eng. Chem. Res., 1993. **32**: p. 1482-1487.

55.   Glebov, E.M., et al., *Kinetics of a Diels-Alder Reaction of Maleic Anhydride and Isoprene in Supercritical CO_2.* Phys. Chem. A, 2001. **105**: p. 9427-9435.

56.   Niehaus, M., et al., *Supercritical Fluid Extraction of Polar Nitrogen Containing-Substances*, in *High Pressure Chemical Engineering*, P.R.v. Rohr and C. Trepp, Editors. 1996, Elsevier Science B. V. p. 345-350.

57.   Mishima, K., et al., *Microencapsulation of Proteins by Rapid Expansion of Supercritical Solution with a Nonsolvent.* AIChE Journal, 2000. **46**: p. 857-865.

58.   Day, C., C.J. Chang, and C. Chen, *Phase Equilibrium of Ethanol + CO_2 and Acetone + CO_2 at Elevated Pressures.* J. Chem. Eng. Data, 1996. **41**: p. 839-843.

59.   Taylor, L.T., *Supercritical Fluid Extraction.* 1996: John Wiley & Sons.

60.   Morris, J.B. *Supercritical Fluid Extraction of Triple-Base and LOVA Gun Propellants.* in *JANNAF.* 1999. San Diego, CA.

61.   McHugh, M.A. and V.J. Krukonis, *Supercritical Fluid Extraction: Principles and Practice.* 1994: Butterworth-Heinemann.

62.   Lee, J.M., B. Lee, and S. Hwang, *Phase Behavior of Poly(l-lactide) in Supercritical Mixtures of Carbon Dioxide and Chlorodifluoromethane.* J. Chem. Eng. Data, 2000. **45**: p. 1162-1166.

63.   Carrot, M.J. and C.M. Wai, *UV-Visible Spectroscopic Measurement of Solubilities in Supercritical CO_2 Using High Pressure Fiber-Optic Cells.* Anal. Chem., 1998. **70**: p. 2421-2425.

64.   Atkins, P., *Physical Chemistry.* 1994, New York: W. H. Freeman and Company.

65.   Petersen, R.C., D.W. Matson, and R.D. Smith, *Rapid precipitation of low vapor pressure solids from supercritical fluid solutions: the formation of thin films and powders.* J. Am. Chem. Soc., 1986. **108**: p. 2100-2102.

66. Debenedetti, P.G., *Homogeneous Nucleation in Supercritical Fluids.* AIChE Journal, 1990. **36**(9): p. 1289-1298.

67. Turk, M., *Influence of thermodynamic behavior and solute properties on homogeneous nucleation in supercritical fluids.* Journal of Supercritical Fluids, 2000. **18**: p. 169-184.

68. Helfgen, B., et al., *Simulation of particle formation during the rapid expansion of supercritical solutions.* Aerosol Science, 2001. **32**: p. 295-319.

69. Chesnokov, E.N. and L.N. Krasnoperov, *Complete thermodynamically consistent kinetic model of particle nucleation and growth: Numerical study of the applicability of the classical theory of homogeneous nucleation.* J. Chem. Phys., 2007. **126**.

70. Weber, M. and M. Thies, *Understanding of the RESS process*, in *Supercritical fluid technology in materials science and engineering*, Y. Sun, Editor. 2002, Marcel Dekker Inc.

71. Lele, A.K. and A.D. Shine, *Morphology of Polymers Precipitated from a Supercritical Solvent.* AIChE Journal, 1992. **38**(5): p. 742-752.

72. Turk, M., *Formation of small organic particles by RESS: experimental and theoretical investigations.* Journal of Supercritical Fluids, 1999. **15**: p. 79-89.

73. Weber, M., L.M. Russell, and P.G. Debenedetti, *Mathematical modeling of nucleation and growth of particles formed by rapid expansion of supercritical solution under subsonic conditions.* Journal of Supercritical Fluids, 2002. **23**: p. 65-80.

74. Huang, J. and T. Moriyoshi, *Fabrication of fine powders by RESS with a clearence nozzle.* J. of Supercritical Fluids, 2006. **37**: p. 292-297.

75. Domingo, C., E. Berends, and G.M. van Rosmalen, *Precipitation of ultrafine organic crystals from the rapid expansion of supercritical solutions over a capillary and a frit nozzle.* Journal of Supercritical Fluids, 1997. **10**: p. 39-55.

76. Matson, D.W., et al., *Rapid Expansion of Supercritical Fluid Solutions: Solute Formation of Powders, Thin Films, and Fibers.* Ind. Eng. Chem. Res., 1987. **26**: p. 2298-2306.

77. Thakur, R. and R.B. Gupta, *Rapid expansion of supercritical solutions with solid cosolvent (RESS-SC) process: formation of griseofulvin nanoparticles.* Ind. Eng. Chem. Res., 2005. **44**: p. 7380-7387.

78.   Shaub, G.R., J.F. Brennecke, and M.J. McCready, *Radial model for particle formation from the rapid expansion of supercritical solutions.* Journal of Supercritical Fluids, 1995. **8**: p. 318-328.

79.   Franklin, R.K., et al., *Formation of perfluoropolyether coatings by the rapid expansion of supercritical solutions (RESS) process. Part 2: Numerical modeling.* Ind. Eng. Chem. Res., 2001. **40**: p. 6127-6139.

80.   Weber, M. and M.C. Thies, *A simplified and generalized model for the rapid expansion of supercritical solutions.* J. of Supercritical Fluids, 2007. **40**: p. 402-419.

81.   Helfgen, B., M. Turk, and K. Schaber, *Hydrodynamic and aerosol modeling of the rapid expansion of supercritical solutions (RESS-process).* J. of Supercritical Fluids, 2003. **26**: p. 225-242.

82.   Khalil, I. and D.R. Miller, *The Structure of Supercritical Fluid Free-Jet Expansions.* AIChE Journal, 2004. **50**(11): p. 2697-2704.

83.   Debenedetti, P.G., *Metastable Liquids.* 1996: Princeton University Press.

84.   Andres, R.P., *Homogeneous Nucleation in a Vapor*, in *Nucleation*, A.C. Zettlemoyer, Editor. 1969, Marcel Dekker Inc.

85.   Hawa, T. and M.R. Zachariah, *Internal pressure and surface tension of bare and hydrogen coated silicon nanoparticles.* Journal of chemical physics, 2004. **121**(18): p. 9043-9049.

86.   Turk, M., et al., *Micronization of Pharmaceutical Substances by Rapid Expansion of Supercritical Solutions (RESS): Experiments and Modeling.* Part. Part. Syst. Charact., 2002. **19**: p. 327-335.

87.   Turk, M., Chem. Eng. Tech., 2004. **76**: p. 835.

88.   Thakur, R. and R.B. Gupta, *Rapid expansion of supercritical solutions with solid cosolvent (RESS-SC) process: Formation of 2-aminobenzoic acid nanoparticle.* Journal of Supercritical Fluids, 2006. **37**: p. 307-315.

89.   Urbanski, T., *Chemistry and Technology of Explosives.* Vol. 3. 1967: Macmillan Publishing Company.

90.   Thorne, P.G., *Evaluation of the use of supercritical fluids for the extraction of explosives and their degradation products from soil.* 1994, U.S. Army Corps of Engineers. CRREL Special Report p. 94-9.

91. Greist, W.H., C. Guzman, and M. Dekker, *Packed-column supercritical fluid chromatographic separation of highly explosive compounds.* J. Chromatography A, 1989. **467**: p. 423.

92. Bird, R.B., W.E. Stewart, and E.N. Lightfoot, *Transport Phenomena.* 2nd ed. 2002: John Wiley & Sons, Inc.

93. Huang, F., et al., *An accurate equation of state for carbon dioxide.* Journal of chemical engineering of Japan, 1985. **18**: p. 490-496.

94. http://webbook.nist.gov. Accessed in 2007.

95. Jr., T.A. and R.L. Ditsworth, *Fluid Mechanics.* 1972: McGraw-Hill.

96. Yoon, S.H., et al., *Heat Transfer and Pressure Drop Characteristics during the in-tube cooling process of carbon dioxide in the supercritical region.* International Journal of Refrigeration, 2003. **26**(8): p. 857-864.

97. Khalil, I.G., *Free-jet expansion of supercritical CO_2,* in *Mechanical Engineering.* 2003, University of California, San Diego.

98. www.chemicalogic.com. Accessed in 2006.

99. Stepanov, V., et al., *High-Resolution Spectroscopic Imaging of Wax-Coated RDX Nanoparticles.* ARDEC Report ARAET-TR-07020, 2007.

100. Matsunaga, T., et al., *In situ optical monitoring of RDX nanoparticles formation during rapid expansion of supercritical CO_2 solutions.* Phys. Chem. Chem. Phys, 2007. **9**: p. 5249-5259.

101. Bonnamy, A., et al., *Characterization of the rapid expansion of supercritical solutions by Fourier transform infrared spectroscopy in situ.* Review of Scientific Instruments, 2005. **76**: p. 053904, 1-8.

102. Rasenack, N., H. Steckel, and B.W. Muller, *Preparation of microcrystals by in situ micronization.* Powder Technology, 2004. **143**: p. 291-296.

103. Merisko-Liversidge, E., et al., *Formulation and Antitumor Activity Evaluation of Nanocrystalline Suspensions of Poorly Soluble Anticancer Drugs.* Pharmaceutical Research, 1996. **13**(2): p. 272-278.

104. Rasenack, N. and B.W. Muller, *Dissolution Rate Enhancement by in Situ Micronization of Poorly Water-Soluble Drugs.* Pharmaceutical Research, 2002. **19**(12): p. 1894-1900.